IPPT Reports on Fundamental Technological Research
1/2025

Jędrzej Dobrzański

Finite-Element Modelling of Moving Weak Discontinuities Using Laminated Microstructures

Institute of Fundamental Technological Research
Polish Academy of Sciences

Finite-Element Modelling of Moving Weak Discontinuities Using Laminated Microstructures

IPPT Reports on Fundamental Technological Research

Editorial Board:
Daria Jóźwiak-Niedźwiedzka – Editor-in-Chief
Łukasz Jankowski, Dariusz Jarząbek,
Dorota Kołbuk-Konieczny, Mateusz Kopeć,
Piotr Korczyk, Magdalena Osial,
Iwona Pokorska-Służalec, Agnieszka Pręgowska,
Norbert Żołek
Bogna Matuszewska-Munk – Managing Editor

Institute of Fundamental Technological Research
Polish Academy of Sciences
Warsaw

IPPT Reports on Fundamental Technological Research
1/2025

Finite-Element Modelling of Moving Weak Discontinuities Using Laminated Microstructures

Jędrzej Dobrzański

Institute of Fundamental Technological Research
Polish Academy of Sciences

Warsaw 2025

Copyright © 2025 The Author(s).
Published by IPPT PAN. This work is licensed under the Creative Commons Attribution License
CC BY 4.0 (https://creativecommons.org/licenses/by/4.0/).

The monograph is based on a doctoral dissertation entitled 'Finite-element modelling of moving weak discontinuities using laminated microstructures', written under the supervision of Prof. Stanisław Stupkiewicz, PhD, Eng., and defended in December 2024 at the Department of Materials Mechanics at the Institute of Fundamental Technological Research of the Polish Academy of Sciences.

The work reported in this thesis has been supported by the National Science Centre (NCN) in Poland through Grant No. 2018/29/B/ST8/00729.

Reviewers:
prof. dr hab. inż. Witold Cecot
prof. dr hab. inż. Łukasz Madej
dr hab. inż. Andrzej Myśliński, prof. IBS PAN

Proofreading:
Publishing Office

Graphic design cover:
Eliza Jezierska

ISSN 2299-3657
ISBN 978-83-65550-62-0 (print)
ISBN 978-83-65550-61-3 (online)
DOI: https://doi.org/10.24423/9788365550613

Received on 10 April 2025

Institute of Fundamental Technological Research Polish Academy of Sciences
(Instytut Podstawowych Problemów Techniki Polskiej Akademii Nauk (IPPT PAN))
Pawińskiego 5B, 02-106 Warsaw
Phone 48 22 826 60 22, e-mail: reports@ippt.pan.pl
https://reports.ippt.pan.pl

Typesetting in LaTeX: Katarzyna Jezierska
Printed in Poland by: EXDRUK, Rysia 6, 87-800 Włocławek, Poland

Abstract

A new computational approach for modelling material and moving weak discontinuities (referred to as *interfaces*) is presented in this thesis. The modelling of moving interfaces, both from a theoretical and numerical point of view, has been a subject of research for many years, leading to various models and computational methods to be found in the literature. One such technique is the well-established *phase-field method* (PFM). Since this approach is not without weaknesses, one of the main aims of this dissertation is to address its limitations and compare it with a new proposed method.

In the new computational approach, based on the finite element method, the *non-conforming* mesh is used. It means that the spatial discretization of the computational domain is incompatible with the internal geometry of the modelled body, indicating that the nodes of finite elements do not lie on weak discontinuities. As a result, an appropriate treatment must be applied to elements cut by the interface to account for the presence of two material phases with typically different parameters. In the proposed method, these elements are replaced by so-called *laminated* elements which are entirely composed of laminated microstructures with the volume fraction of both phases and the lamination orientation determined by the interface position within the finite element. Hence the name of the method – *laminated element technique* (LET).

The performance of LET is demonstrated through numerical simulations of problems typical for solid mechanics. The examples include both two- and three-dimensional problems, involving linear elasticity as well as elasto-plastic cases within finite deformations. Where possible, results obtained using LET have been compared with those from other methods, including analytical solutions, as well as results found in the literature. The obtained results confirm that LET is not able to achieve an optimal convergence rate (with mesh refinement) characteristic of finite-element modelling using conforming meshes. However, the results also demonstrate that LET can continuously respond to the continuous change in the interface position within a single finite element, providing a direct basis for generalizing this method to cases involving moving interfaces.

The generalization of LET to problems involving moving interfaces became feasible through its coupling with the phase-field method. The resulting computational technique, named LET-PF, exploits the advantages of PFM while simultaneously reducing some of its limitations. In LET-PF, unlike PFM, the phases of both materials are mixed within a thin layer of only one-element thickness. This allows obtaining results of higher accuracy compared to the conventional PFM or results of comparable accuracy but using coarser meshes, thus reducing the computational cost.

The performance of LET-PF is demonstrated through problems typical for micromechanics of heterogeneous materials. These examples are limited to two-dimensional cases within linear elasticity. Results obtained using LET-PF have been subjected to an extensive comparative analysis, where they have been confronted with results from PFM and, if possible, with analytical solutions. This comparison leads to the conclusion that,

in certain cases, LET-PF eliminates limitations of the conventional phase-field method, thus providing a significant advantage. Consequently, one of the main objectives of the dissertation has been achieved.

KEYWORDS: finite element method, weak discontinuity, interface, phase-field method, non-conforming mesh, laminate, microstructure evolution.

Streszczenie

W niniejszej rozprawie zaprezentowano nową metodę obliczeniową, która służy do modelowania materialnych i ruchomych powierzchni nieciągłości (tzw. *interfejsów*). Zagadnienie modelowania ruchomych interfejsów, zarówno od strony teoretycznej, jak i numerycznej, jest przedmiotem badań od wielu lat i w związku z tym w literaturze naukowej można odnaleźć modele oraz metody obliczeniowe, które zmagają się z tym problemem. Jednym z takich podejść o dobrze ugruntowanej pozycji jest *metoda pola fazowego* (ang. *phase-field method*). Ponieważ metoda ta nie jest pozbawiona mankamentów, jedną z głównych aspiracji niniejszej rozprawy jest zaadresowanie jej ograniczeń i skonfrontowanie jej z nowym, proponowanym podejściem obliczeniowym.

Nowa metoda obliczeniowa, oparta na metodzie elementów skończonych, wykorzystuje tzw. *siatkę niezgodną*. Oznacza to, że przestrzenna dyskretyzacja domeny obliczeniowej nie jest dopasowana do wewnętrznej geometrii modelowanego ciała, czyli że węzły elementów skończonych nie leżą na powierzchniach nieciągłości. Skutkuje to tym, że w elementach skończonych przeciętych interfejsem należy zastosować odpowiednią procedurę, która pozwoli uwzględnić obecność dwóch faz materiału o przeważnie różnych parametrach. W prezentowanej metodzie elementy te zastępuje się tzw. elementami *laminatowymi*, czyli takimi, które w całości są utworzone z mikrostruktury warstwowej o ustalonym udziale objętościowym obu faz oraz kierunku laminacji wynikających z pozycji interfejsu w ramach elementu skończonego. Stąd też nazwa metody – *laminated element technique* (LET).

Cechy metody LET zaprezentowano na podstawie symulacji numerycznych zagadnień typowych dla mechaniki ciała stałego. Rozwiązywane zagadnienia obejmowały zadania dwu- i trójwymiarowe, zarówno w ramach liniowej sprężystości, jak i sprężystoplastyczności z uwzględnieniem skończonych deformacji. Tam, gdzie to było możliwe, wyniki uzyskane za pomocą metody LET porównano z wynikami pochodzącymi z innych metod, w tym metod analitycznych, a także z wynikami znalezionymi w literaturze. Uzyskane rezultaty potwierdziły, że metoda LET nie jest w stanie osiągnąć optymalnego stopnia zbieżności (wraz z zagęszczaniem siatki elementów skończonych) charakterystycznego dla modelowania w metodzie elementów skończonych z wykorzystaniem siatek zgodnych. Wyniki dowiodły też jednak, że metoda LET jest w stanie w sposób ciągły reagować na ciągłą zmianę położenia interfejsu w ramach jednego elementu skończonego, co stanowiło bezpośrednią przesłankę do uogólnienia tej metody na przypadki interfejsów ruchomych.

Uogólnienie podejścia obliczeniowego LET na przypadki ruchomych interfejsów było możliwe dzięki sprzężeniu go z metodą pola fazowego. Otrzymana technika obliczeniowa – LET-PF – wykorzystuje zalety metody pola fazowego przy jednoczesnym zmniejszeniu jej ograniczeń. W przeciwieństwie do metody pola fazowego, w metodzie LET-PF fazy obu materiałów są mieszane w ramach cienkiej warstwy o grubości jednego elementu skończonego. Pozwala to na uzyskiwanie wyników o większej dokładności lub

wyników o zbliżonej dokładności, ale przy stosowaniu siatek dyskretyzacji o mniejszej rozdzielczości i, tym samym, przy mniejszym koszcie obliczeniowym.

Osiągi metody LET-PF zaprezentowano na przykładzie zadań typowych dla mikromechaniki materiałów niejednorodnych. Ograniczono się w nich do przypadków dwuwymiarowych w zakresie liniowej sprężystości. Rezultaty otrzymane metodą LET-PF poddano obszernej analizie porównawczej, w której zestawiono je z wynikami pochodzącymi z metody pola fazowego oraz, o ile to było osiągalne, z rozwiązaniami analitycznymi. Konfrontacja ta pozwoliła dojść do wniosku, że metoda LET-PF w pewnych przypadkach eliminuje ograniczenia konwencjonalnej metody pola fazowego i tym samym ma nad nią istotną przewagę. Tym samym osiągnięto jeden z głównych celów rozprawy.

Słowa kluczowe: metoda elementów skończonych, powierzchnia nieciągłości, interfejs, metoda pola fazowego, siatka niezgodna, mikrostruktura warstwowa, ewolucja mikrostruktury.

Contents

1. Introduction

1.1. Motivation

Solving partial differential equations on complex geometries plays a dominant role in many problems of interest in computational solid mechanics. The complexity of geometry may be associated with the external shape of the investigated domain; however, it is the intricacy of the internal geometry within the domain, linked to its non-homogeneity, that constitutes a source of challenges. Analytical solutions that consider possible geometrical heterogeneities are not available in most cases. Computational approaches are thus indispensable, the finite element method (FEM) being the most general, most powerful and most popular computational tool for numerical simulations in various areas of engineering.

Historically, FEM relies on geometry-dependent computational grids (body-fitted or conforming meshing). However, due to the complexity of investigated geometries, especially internal heterogeneities, a fine conforming discretization can be quite hard to use. One reason is the limited computational cost that can be afforded. Although algorithms for finite element meshing in 2D are quite efficient and well-established, the mesh generation for 3D problems still remains a rather cumbersome and time-consuming task. This problem is particularly pronounced when discretising geometries that contain discontinuities or objects (details) with diverse characteristic lengths. Secondly, some additional manual input is often needed or the use of specialized mesh generation software. Thirdly, for 3D models, especially large-scale ones, unstructured meshes, which are necessarily needed to represent complex geometries, may lead to additional difficulties associated with the assembly and solution of the respective finite-element equations. And finally, even if the previous obstacles can be somehow overcome, additional effort may be needed during post-processing. Overall, mesh generation may become the most time-consuming process in the preprocessing step of numerical modelling, and dealing with conforming meshes for complex geometries may significantly increase the computational expense.

A possible approach to evade the mesh generation problem is to use a non-conforming mesh. In general, the respective methods use a structured mesh or a simple unstructured mesh generated in the domain defined by the external boundary of the modelled geometry. Generating such a mesh is then a straightforward process. However, the internal details of the geometry must somehow

be treated, and several approaches have been developed for that purpose, as discussed in the next chapter.

The issues mentioned so far relate to the modelling of the so-called *material* discontinuities, that is, such regions where two subdomains of different materials come together and are separated by a distinct internal boundary – an interface. This interface, whose position is strictly related to the material points (particles) of the body at that specific location, typically represents a discontinuity zone where a jump in parameters such as stiffness or density can be observed. These, in turn, are the source of discontinuities in mechanical quantities such as strain and stress. Material interfaces defined in this way can deform due to mutual deformations in both subdomains, however, they cannot propagate, i.e., "wander" through successive material points (particles) of the body.

Material interfaces are everywhere, and numerous examples of their occurrence can be identified. In engineering, for instance, it would be primarily any composite material, such as concrete, where the interfaces are the boundaries between the aggregate (inclusions) and the cement (matrix), or carbon fibre-reinforced polymers (CFRP), where the interfaces between reinforcing fibres and the matrix material (e.g., epoxy resin) constitute the overall performance of the composite structure. Nature also exhibits the presence of interfaces; for instance, soil, as a material, typically consists of multiple fractions separated by interfaces. Taking into account the heterogeneity of soil is crucial in the construction of large structures like skyscrapers and bridges.

However, heterogeneities, and consequently the associated interfaces, should not only be observed at the macroscale. In general, most materials exhibit heterogeneity on the mesoscale. Their microstructure is composed of grains and domains, whose shape, size, and mutual distribution significantly affect macroscopic properties. Moreover, it is crucial to emphasize that real microstructures are often, by their nature, thermodynamically unstable structures that may undergo evolution. This implies not only the existence of interfaces on the mesoscale but also their propagation over time. These are referred to as *moving* interfaces. Instances of such interfaces are evident in phenomena such as phase transformations, wherein a material exhibits two distinguishable phases separated by a propagating front. Dealing with the modelling of moving interfaces poses considerable challenges, both analytical and numerical. This is due to the interplay between the physical process (for instance, the mechanical deformation) and the geometry of the evolving interface, but also to the need to develop suitable algorithms that allow consistent discretization with respect to the position of the interface.

In the last few decades, attempts to create numerical models efficiently simulating moving interfaces have been the cornerstone of research for many scientists. In the literature, as discussed in the following chapter, numerous formulations have been found that have subsequently been used to simulate processes such

as melting/solidification, solid-state phase transformations (martensitic transformations and twinning), precipitate growth and coarsening, grain growth, and many more. Among all the techniques developed, two classes of approaches can be distinguished. The first is known as *sharp-interface tracking* models. In this approach, the interface is a geometric entity explicitly defined – it is a curve or surface (depending on whether the problem is two- or three-dimensional), with its shape and position precisely determined. At each subsequent time step, this information is updated based on relevant equations. The undeniable drawback of this class of methods is the necessity of tracking the interfaces, which often poses a barrier to effectively modelling phenomena where interfaces have complex shapes, especially in three dimensions. Addressing this limitation is the second class of methods, which has been leading in recent years in modelling moving interfaces. This is the so-called *diffuse-interface* or *phase-field* approach. In these techniques, interfaces are implicitly defined – their position and shape are governed by a scalar field of phase-field variable, spanned across the entire domain of the considered problem. Despite its versatility, this method has one significant drawback, which is the computational cost associated with the need for relatively high discretization resolutions to resolve interfaces accurately. The aim of this thesis is thus to develop a new computational method that will serve as a compromise between these two classes of approaches, combining the advantages of both.

1.2. Research aims and objectives

The primary aims set in this thesis are:

- **to develop and implement a new computational method for finite-element modelling of material and moving weak discontinuities using laminated microstructures**, and
- **to test this method in solid mechanics problems and compare its performance with other existing methods**.

In the context of modelling material interfaces, the aim of this dissertation is to formulate a simple method within the finite element framework where the finite element mesh remains independent of the internal geometry of the domain. Numerous approaches in the literature meet this criterion, with the well-established extended finite element method (X-FEM) standing out for its optimal convergence rate. Therefore, the intention is not for the new method to compete with existing ones, such as X-FEM. Instead, the primary criteria set for this approach are simplicity, ease of implementation, and the preservation of elemental character, which means that, unlike the aforementioned X-FEM, no additional global degrees of freedom are needed and the user intervention into the code is not necessary. Furthermore, an essential requirement for the new

technique is its capacity for a continuous response with respect to continuous change in the position of the interface. Such a property is crucial for generalizing the method to model moving interfaces, which forms the central focus of this dissertation.

The primary goal of this thesis is to develop an approach for modelling moving interfaces, that is based on the phase-field method and improves upon it in a certain aspect. It is known, as detailed further in Chapter 3, that the phase-field model has a drawback, namely, the necessity of employing a relatively fine discretization to accurately resolve the interface. In this regard, the new method aims to be superior, allowing for the use of coarser discretization while still providing results of satisfactory accuracy, i.e., better compared to the conventional phase-field method.

In the case of material interfaces, the developed method has been compared with other approaches also utilizing non-conforming meshes, including, where possible, X-FEM and other methods, whose results have been found in the literature. For moving interfaces, an extensive comparative analysis of the selected problems has been conducted with the conventional phase-field approach.

1.3. Scope of the thesis

The thesis is conceptually divided into two parts. The first is devoted to the modelling of material weak discontinuities. The second part, which is the core of this work, exposes the concerns related to the modelling of moving weak discontinuities. The implementation of the proposed method is performed within the finite-element framework, specifically in the *AceGen* environment, while all computational examples have been conducted in the software *AceFEM* [76, 78]. The examples presented in the thesis are limited to the static or quasi-static solid mechanics problems.

Chapter 2 provides 4 a literature overview. In the first section, existing numerical methods for modelling material weak discontinuities, which, like the method presented in this work, utilize non-conforming meshes, are briefly discussed. In the second section, a more comprehensive literature review is presented, focusing on methods used for modelling moving interfaces.

In Chapter 3, three sections present the necessary theoretical foundations used in the dissertation. In Section 3.1, the problem of a two-phase body with material weak discontinuity is formulated in both finite- and small-strain frameworks, along with the finite-element treatment. Subsection 3.2.1 addresses the two-phase body problem with a moving weak discontinuity. It introduces the reference sharp-interface problem and its alternative version within the diffuse-interface framework. At the end of Subsection 3.2.1, the finite-element treatment of the phase-field model is provided. Chapter 3 concludes with Section 3.3, where

the basic equations of the theory of simple laminates are presented. They are a key part of the method presented in the dissertation.

In Chapter 4, the idea and formulation of the developed method for material interfaces, called *laminated element technique* (LET), are introduced. In the following Chapter 5, LET combined with the phase-field model (LET-PF), being the generalization of the method to moving interfaces, is presented. In both Chapters 4 and 5, the discretized weak forms of the governing equations, ready to be used in the finite element method, are provided.

Chapters 6 and 7 demonstrate the performance of the presented method using static or quasi-static solid mechanics problems, addressing material and moving interfaces, respectively. In Chapter 6, a total of five problems are considered. The first three are within the linear elasticity framework, while the remaining two adopt the finite-deformation framework. The first finite-deformation example assumes hyperelastic constituents, while the second involves an elasto-plastic material. The examples shown in Chapter 6 are both two- and three-dimensional. Chapter 7 comprises two numerical examples. The first includes an extensive parametric analysis based on a problem with an analytical solution, provided in Appendix E. The second computational example illustrates the evolution of a two-dimensional cell, ensuring a non-trivial steady-state solution. Both computational examples in Chapter 7 are limited to 2D problems within the framework of small-strain elasticity and in both of them, the performance of LET-PF is compared to the conventional phase-field method.

The thesis concludes with Chapter 8, where possible extensions and improvements of the developed method are presented, along with the final conclusions.

The results presented in this dissertation have already been published in the form of two peer-reviewed articles [34, 35]. In the first one [35], a formulation of a new method for modelling material interfaces is introduced, accompanied by numerous numerical examples from the field of solid mechanics. The second of the mentioned works [34] is entirely dedicated to the generalization of this method for modelling moving interfaces. It presents both the development of the new method coupled with the phase-field framework and its performance through extensive numerical simulations in the domain of solid mechanics. Since the content of these articles coincides with the material presented in this dissertation, some parts in this thesis (chapters, sections or appendices) reproduce the content of those publications, in particular Chapters 6 and 7. The parts that are entirely excerpted from the papers are indicated by a footnote at the beginning of the relevant chapter, section or appendix. In the remaining part of the thesis, the duplicated sections from the articles have been expanded to a greater or lesser extent.

2. Literature overview

As mentioned in the introduction, the results of this work have been divided into two parts. Therefore, in this literature review, Section 2.1 addresses methods for modelling material interfaces, while Section 2.2 presents techniques used for simulating moving interfaces. However, the latter part, as it is more related to the essential part of this thesis, is presented here in a much more extensive manner.

2.1. Computational modelling of material weak discontinuities

The focus of this work is on weak discontinuities, i.e., on the situation in which the primal variable (e.g., the displacement field) is continuous at the interface and discontinuous are its derivatives and related quantities (e.g., strains and stresses) when the material properties (e.g., elastic moduli) suffer discontinuity at the interface. This is in contrast to strong discontinuities, such as cracks, when the primal variable may be discontinuous at the interface (of possibly unknown and evolving shape). Actually, several methods have been primarily developed for strong discontinuities and have then been adapted to weak discontinuities.

This is, for instance, the case of the extended finite element method (X-FEM) initially developed for modelling crack propagation independent of the underlying finite-element mesh [9,108], see also two methods that are closely related to X-FEM, namely CutFEM [18] and phantom node method (PNM) [139], and are sometimes considered just versions of X-FEM. It has been subsequently shown that X-FEM can be successfully used also for modelling complex internal geometries (weak discontinuities) of the geometry independent of the finite-element mesh [10, 109, 146]. With the increasing popularity of the isogeometric analysis (IGA) [61], the X-FEM approach has been also combined with IGA [48, 98], including XIGA for weak discontinuities and multimaterial problems [113, 150].

In X-FEM, the inner surfaces (e.g., material interfaces, cracks) are defined implicitly using level set functions [115]. Enrichment functions are then employed to modify the finite-element approximation of the displacement field such that the discontinuity is represented on a non-matching mesh. As a result, the optimal convergence rate can be achieved. The beneficial features of X-FEM come at the cost that additional global degrees of freedom are introduced (those as-

sociated with the enrichment shape functions). Moreover, integration must be performed accurately on the elements cut by an interface and, for this purpose, the elements are triangulated such that the subdomains match the interfaces. This becomes even more complex when more than one interface passes through an element, which is not so improbable, for instance, in the case of small inclusions or multi-material problems. Overall, implementation of X-FEM is not straightforward, particularly in 3D, and cannot be performed solely at the element level.

Additional deformation modes, in a sense similar to the enrichment functions of X-FEM, are also introduced in the immersed interface FEM (IIFEM) [91, 94] and in the augmented finite element method (AFEM) [42, 97]. The difference is that, unlike in X-FEM, the enrichment functions are not continuous at the inter-element boundaries, which implies that the optimal convergence rate cannot be achieved. To improve convergence, the inter-element compatibility is enforced in a version of IIFEM [92], which then bears some similarity to X-FEM. In the incompatible case, the additional degrees of freedom associated with the additional deformation modes can be condensed at the element level, hence no additional global degrees of freedom are introduced.

Common to the approaches discussed above is the "small cut-cell" problem that may appear when a small part of the element is cut by an interface. This may lead to a large condition number of the algebraic system to be solved and may deteriorate numerical stability of the resulting algorithms, thus additional stabilization techniques are needed.

A different approach is adopted in the shifted interface method (SIM) [88, 89] in which the interface is shifted to a nearby inter-element boundary. At the same time, to compensate for the error introduced by shifting the interface, the interface jump (compatibility) conditions are applied at the surrogate interface in a modified form resulting from the Taylor expansion of the original jump conditions. As a result, the optimal convergence rate can be achieved [89].

It is also worth mentioning two simple non-conforming methods. While not as sophisticated as those mentioned above, and none of these methods has been specifically named, examples of their application can be found in the literature. The first method involves assigning the entire finite element to one of the two phases based on the value of some function (implicitly describing the interface geometry) at the central point of the element. In the literature, this approach is sometimes referred to as *digital-image-based* FEM [70, 151] or *voxel-based* FEM [93]. The second of these simple non-conforming methods differs from the first in that the phase assignment occurs not at the level of the entire element (at its central point) but at the level of individual integration (Gauss) points. In this way, the accuracy of this latter approach can be improved by increasing the number of integration points, see [42, 109]. Concerning voids and free boundaries, this latter approach is closely related to the finite cell method [116]. These

two simple approaches are used in Chapter 6, where, as part of the numerical simulations, their results are compared with those of the method proposed in this thesis.

In this thesis, a simple method for improved treatment of weak discontinuities in non-conforming FEM discretization is developed. It is presented in detail in Chapter 4, after Dobrzański *et al.* [35]. The inspiration came from recent developments in the FFT-based methods in computational homogenization. In this class of approaches [107], a periodic unit cell is discretized into a regular array of voxels, hence complex-shaped interfaces cannot be represented exactly. In order to increase the accuracy of FFT-based homogenization, the idea of *composite voxels* has been introduced in [17], see also [155] for a related approach in the context of FEM, and was the first attempt to use a homogenization technique to prescribe effective mechanical properties to the voxel that contains an interface between two phases. This idea was further developed by considering the composite voxel to be represented by a *laminated microstructure* and characterized by the corresponding effective properties [47,64]. It has been shown that these laminate voxels significantly improve the accuracy of the method as compared to the composite voxels employing simple Voigt and Reuss bounds [64]. Further related developments in the context of FFT-based homogenization include the extension to inelastic problems [66, 101] and to the finite-strain framework [65, 69].

2.2. Computational modelling of moving weak discontinuities

Numerical tracking of moving interfaces constitutes a prominent area of interest in computational physics. With the advancement of computer techniques such as the finite element method or finite difference method over the years, researchers have made various attempts to develop numerical algorithms for simulating interface motion. A review of the literature reveals the emergence of two distinct classes of methods that differ in how they treat weak discontinuities. The first type of models, known as sharp-interface tracking models, assumes that the interface is a precisely localized curve or surface, depending on whether the problem is two- or three-dimensional, and that certain jump conditions must be fulfilled over this interface. The second class of models, known as diffuse-interface models, assumes that the surfaces of discontinuity are smeared out and described by a continuous scalar field spanning the entire domain. The following sections present a discussion of both of these approaches.

2.2.1. Sharp-interface tracking models

Sharp-interface tracking models are a broad family of techniques in which information about the position and shape of an interface is stored explicitly at each time step, while the evolution of the interface is subject to the associated

interfacial equation of motion. It is important to acknowledge that researchers in computational fluid dynamics have made significant contributions to the development of tracking interface methods. Many approaches used in other fields, such as solid mechanics, have their origins in this area. This is due to the fact that the modelling of a free boundary, specifically the gas–liquid interface or the free surface, which refers to the interface between two well-separated immiscible fluids, is a common challenge addressed in simulations across various problems in computational fluid dynamics [53, 103, 120, 121, 131, 149, 180].

Among these methods, two classes of approaches can be distinguished [152]. The first one is the interface-tracking methods, also sometimes referred to as the Lagrangian techniques. In this approach, spatial discretization is adjusted at each time step to accommodate the changing topology of the interface so that it is conforming, i.e., that grid points or finite-element nodes lie directly on the interface. This approach is sometimes also called, in the context of the finite element method, an adaptive remeshing technique [31, 130, 133, 141]. The topology of the interface in subsequent time steps is subject to the solution to the evolution equation, coupled with the other equations of the problem. This implies that the spatial discretization of the problem must be destroyed and built again at each time step. Although such an approach ensures high accuracy of the solution, as the interface is explicitly modelled as the edges of finite elements, an undeniable drawback of this approach is the computational cost associated with the need for multiple discretization processes. This is especially evident in the case of interfaces with complex geometry, which can pose challenges, particularly in solving three-dimensional problems.

The second class of approaches is known as interface-capturing methods, also referred to as the Eulerian techniques. It is characterized by the spatial discretization of the domain remaining independent of the evolving interface geometry. Consequently, the use of more sophisticated finite-element codes capable of capturing the non-matching interface is required, which may pose a certain challenge and thus be a drawback of this class of methods. However, simultaneously, the advantage of this approach over the previous one is that the computationally expensive process of mesh/grid generation at each time step is avoided. Therefore, this is a much broader class of methods, as it allows, in its generality, the use of any method employing non-conforming meshes mentioned in Section 2.1 as a part of the approach. For instance, the approach using the X-FEM technique has been used to simulate the microstructure evolution [37, 62, 111].

However, regardless of which approach is chosen for modelling moving interfaces, in the class of sharp-interface tracking models, attention must also be paid to how the interface, as a geometric object, is represented and how its position is updated. One approach involves discretizing the interface using a separate data structure containing information about a set of marker-points. These points, densely packed on the interface (with a spacing comparable to the size of

spatial discretization), describe its position and shape. Alternatively, points can be packed at larger intervals, and then an appropriate curve or a higher-order surface would describe the topology of the interface. Subsequently, a tailored evolution equation, coupled with other equations, describes the movement of these points and, consequently, the interface. This approach, often referred to as the *front-tracking* method in the literature [51,158], has been used, among other applications, in modelling blood flow in the heart [118], multi-fluid flows [163], dendritic solidification [63,185], grain growth [5,140] and many more. However, this approach has certain drawbacks. Each interface has a separate discretization. If, during evolution, two separate interfaces merge, then their separate discretizations must be unified, requiring special treatment. Another problem is that certain parts of the interface may experience thinning of marker-points, while others may experience grouping. In both cases, this should be addressed by appropriately adding new points or removing them to avoid clustering, respectively. While these issues are relatively easy to resolve in two-dimensional problems, in three dimensions, the problem becomes much more challenging to implement, although not impossible, as demonstrated in [51].

In the above-mentioned approach, tracking the distribution of marker-points and their connectivity is computationally troublesome and expensive, requiring reinitialization at each time step. To address this drawback, the well-established and popular level-set method [115,134] comes to the rescue. Thanks to its generality and robustness, this method has been applied in various fields such as fluid mechanics [135], solid mechanics [10, 109, 146], crack growth [108, 144], phase transformations [62], shape optimization [2,11,176], and many more. Currently, the term "level-set method" is very general and refers to describing the interface as a curve or surface implicitly, using the zero level set of the level-set function. This approach has been widely adopted in interface-tracking and interface-capturing methods [147,148,163], replacing the marker-points approach. In this method, changes in the interface topology are recorded by the changes in the level-set function governed by the appropriate evolution equation. Because positive values represent the phase on one side of the interface, and negative values represent the other, the level-set method easily handles merging or breaking. One characteristic of the level-set method is that the level-set function is a signed distance function that measures the distance to the closest point on the interface. However, during evolution, this property is lost. In some cases, it is crucial to preserve this property. Therefore, reinitialization must be performed at each time step, restoring the signed distance function property, which increases computational cost.

Among the interface-capturing methods, it is worth mentioning the historical marker-and-cell method [57], developed at the Los Alamos National Laboratory. In this method, a set of discrete Lagrangian particles is used to identify the regions occupied by a specific fluid. A kind of continuation of this method is

the volume of fluid method [59, 112], where interface tracking is done indirectly by calculating the volume fractions of both phases in a given grid cell. Volume fractions are incorporated into the problem to be solved by the advection equation. Therefore, there is no explicit representation of the interface; rather, it is reconstructed based on the values of volume fractions. For more information on these methods, the reader is referred to [128].

The limitations of the above-mentioned methods were addressed in the doctoral thesis by [154]. The author developed a method known as the segment projection method, which serves as a compromise between front-tracking and level-set methods [39, 40, 153]. The main idea of this method involves splitting the considered interface into several segments that can be described as functions of one spatial variable. In this way, each interface is defined by the union of curve parts. Due to the overlapping nature of these parts, explicit information about their connectivity must be provided. The segments in this method are discretized using points on the curves, as in the front-tracking method. However, the discretization is Eulerian in nature, akin to the level-set method. Although the segment projection method emerged by combining the strengths of front-tracking and level-set methods, it is not without weaknesses. Since each interface in this method requires a separate and independent description, phenomena such as merging and breaking of interfaces require an additional algorithm. While this is relatively easier than in the case of front-tracking methods, given that the segments are functions of one variable, it is still considered as one of the inconveniences of this method.

In the context of the interface-tracking methods a very recent method used in the finite-element environment should be noted – the so-called eXtreme Mesh deformation approach (X-MESH) [110]. This technique allows the sharp interfaces to be tracked, and although it belongs to the group of interface-tracking methods, it avoids remeshing the entire domain and changing the mesh topology at each time step. Instead, the mesh is deformed only in the close neighbourhood of the evolving interface, producing almost degenerated elements (with zero measure). The idea of X-MESH is similar to the Arbitrary Lagrangian–Eulerian (ALE) approach [60], but differs in that the nodes lying on the interface are not the same throughout the process – the key idea of the X-MESH is to allow elements to be distorted up to zero measure while maintaining their connectivity so that the interface can be relayed between the nodes. So far, the approach has been used to simulate the Stefan phase-change model [110] and the immiscible two-phase flow [6, 123].

2.2.2. Diffuse-interface models

A completely different way to model moving interfaces is by using a variety of models that apply the so-called *phase-field method*. Although the basic idea

behind this approach goes back to the late 19th century, it has become extremely popular in the last 20–30 years. This is evidenced by the vast number of publications that have appeared during this time. This increased interest is mainly due to the significant improvement in the technology of computers and their ability to perform complex calculations during this time. The abundance of scientific papers reflects the fact that this method has become the top choice for numerical simulations of microstructure evolution. Because this dissertation is closely related to the phase-field method, this chapter has been dedicated to exploring it in more detail.

The phase-field method is a continuum theory that traces its origins back to the 19th century, specifically the 1890s. That was the time when van der Waals published a work related to the theory of capillarity in a thermodynamic framework [166–168], see also the translation [127]. In his considerations, the author observed that a more natural assumption is that the density change between liquid and gas occurs continuously, as opposed to the earlier belief in a sharp, step-like manner described by a step function. Van der Waals also postulated that the free energy at a given point, particularly in the vicinity of the interface, should be determined not only by the density at that point but also by its values at neighbouring points. These assumptions laid the foundation for the phase-field method, characterized by the rejection of a sharp discontinuity between different phases and the adoption of a continuous transition from one phase to another. The interface defined in this way is no longer a discontinuity and is termed a *diffuse interface*.

Van der Waals' work and his concept of diffuse interfaces, although initially met with great enthusiasm, were forgotten for many years. At this point, Landau's work from 1937 [80, 81] should be mentioned, where the author presented a theory serving as a phenomenological framework for describing second-order continuous phase transformations. A typical approach for determining thermodynamic parameters such as free energy involves a tedious process of solving the Schrödinger equation. Landau recognized that, instead, the free energy near the interface could be successfully approximated using the first terms of the Taylor expansion. The argument of this polynomial is the so-called order parameter, whose specific value indicates the presence of a particular phase at a point and is assumed to be a continuous function of the position. Since the Taylor expansion is also a continuous function, the free energy within the interface is described in a continuous manner. As a result, the interface between the two phases is characterized in a diffuse way. Although the work of Landau [80] did not explicitly refer to the publication by van der Waals [166], it is evident that his theory bears some similarities with van der Waals' theory and in some simpler cases both models coincide. Landau's concept was also used later in a paper by Ginzburg and Landau [49, 50], where a complex-valued order parameter and its gradients were used to model superconductivity.

The breakthrough came with a paper by Cahn and Hilliard [23]. Essentially, the results of their work were similar to those in the publication by van der Waals [166], albeit expressed in a more modern tone. This made their work the foundation for many important applications in the area of statistical thermodynamics of nonuniform systems [15, 84, 157, 182] over the following years. These applications include areas such as wetting [22, 105], nucleation or spinodal decomposition [21, 52, 82], and liquid–liquid interfaces [179].

The aforementioned period of the development of the phase-field method (the 1960s and 1970s) also corresponds to dynamic development of the finite element method [3, 28, 100, 186], as well as other numerical methods such as the finite difference method. At the turn of the 1970s and 1980s, mass-produced computers designed for home use became widely available. Therefore, it was only a matter of time before the numerical implementation of the phase-field method became a heavily researched topic. The first formulation of the phrase *phase-field model* is attributed to the authors of two works from the 1980s. In the work by Langer [83], inspired by the so-called *model C* [56], phase-field equations were presented for the first time, which, according to the author, provide a natural basis for creating an algorithm for numerical simulations. In his work, the phase-field method was used purely to avoid tracking the interface. In the same spirit, the *phase-field model* was also introduced in the work by Fix [44], where it was used to model the free boundary problems. It is also worth mentioning the works of Caginalp [19], Caginalp and Fife [20], Collins and Levine [29], where solid mathematical justifications and other considerations on the phase-field method were presented. Additionally, the works of Penrose and Fife [117], Wang *et al.* [169], Wheller *et al.* [177] generalized existing models in the literature, providing a general framework for modelling the phenomenon of solidification.

When discussing diffuse interfaces in the modelling of microstructure evolution, recognition should be also given to the works of Chen and Khachaturyan [25] and Wang *et al.* [172]. They independently derived the phase-field model from the microscopic theory of Khachaturyan [71, 72]. In their approach, the phase-field variables refer to microscopic parameters (e.g., the local composition or the long-range order parameter). The applications of the model are broad and include solid-state phase transformations, such as the precipitation of an ordered intermetallic phase from a disordered matrix [87, 164, 173] and martensitic transformations [7, 170], but also the ferroelectric [26, 90] and magnetic domain evolution [184].

However, the groundbreaking work by Kobayashi [75], which presented, probably for the first time, results of a numerical model using the phase-field method for simulating dendritic crystal growth in 2D, stands out. Kobayashi's work significantly propelled the development of the phase-field method, opening the doors to the numerical modelling of microstructure evolution. In the subsequent years, other important works emerged, such as those by Wheeler *et al.* [178] and Warren

and Boettinger [175], dedicated to modelling dendritic growth of a pure material; Steinbach *et al.* [143], proposing the multiphase-field concept for modelling multiphase systems; and Karma and Rappel [67, 68], introducing improvements for more efficient modelling of solidification in three dimensions. The ongoing successes of the phase-field method further motivated researchers to test and implement the method for various applications. Currently, it is impossible to count all the publications related to it, and the pace of new works being published shows no sign of slowing down.

From today's point of view, the phase-field method is a well-established, versatile and powerful approach to computational modelling of microstructure evolution problems [24,104,122,142,156,171]. Microstructure evolution is inherently associated with the propagation of interfaces that separate individual phases, and this constitutes the main challenge in developing computational approaches for the corresponding problems. The essence of the phase-field method is in treating the interfaces as diffuse, rather than sharp, which is achieved by introducing a phase-field variable (so-called order parameter) that differentiates the phases and varies in a continuous manner within the diffuse interfaces. Accordingly, the propagation of interfaces can be simulated on a fixed finite-element mesh. Tracking of interfaces is thus avoided, which would otherwise require, for instance, adaptive remeshing or enhancement techniques such as X-FEM. This, in turn, makes it possible to study the evolution of arbitrarily complex morphologies without having to make any presumptions about their shape.

The phase-field method is highly versatile because the diffuse-interface framework can be combined with virtually any physics and, in fact, has been used in numerous contexts, for instance, solidification [114], solid-state transformations [24, 54, 162], including martensitic transformation [85, 161, 170, 181] and twinning [27, 95, 126], fracture [4, 16], corrosion [30], ferroelectric [26, 90] and magnetic domain evolution [184], electromigration [12], solid-state sintering [174], biological applications [14, 36], and many more.

Another important feature of the phase-field method is that the order parameter carries information about the energy of the interfaces. The interfacial energy is naturally included in the energy balance and thus contributes to the driving force for interface propagation, which is particularly important at smaller scales at which the interfacial energy effects are more pronounced. It is also the interfacial energy term in the free energy function that sets the thickness of the diffuse interfaces through the term involving the gradient of the order parameter. Moreover, considering that the contribution of interfaces to the total energy of a system is size-dependent, the phase-field method is able to model the size effects [124, 159, 183].

Current research on the phase-field method also places significant emphasis on the quantitative aspect of numerical simulations. The phase-field method, by its nature, is a phenomenological approach – the evolution equations describing the

phase-field variables are derived on the basis of general thermodynamic and kinetic principles. However, the phase-field method does not describe behaviour at the atomistic level, so specific thermodynamic inputs, such as interfacial energy or mobility, must be determined based on experimental and theoretical research. In some cases, they are not even directly accessible by experiment. A remedy for this limitation can be then the combined phase-field method with the so-called *ab initio* or *first-principles* calculations [13, 73, 74, 99, 165], which use quantum mechanical methods to determine parameters numerically without empirical fitting or adjustment. In this way, this mixed approach acts as a bridge between atomistics and microstructure, providing a method that allows both qualitative and quantitative predictions.

However, the beneficial features of the phase-field method, as discussed above, come at a price of a high computational cost. This is because a sufficiently fine computational grid (mesh) is needed to correctly represent the profile of the order parameter across the diffuse interface (whose thickness is very often of much smaller scale than the characteristic dimension of the problem) and to correctly represent the corresponding interfacial energy. This sets a severe constraint on the maximum allowable element size, and the associated high computational cost limits the maximum physical dimension of the domain that can be considered in the computations.

With the aim to overcome the limitations discussed above, the so-called "sharp phase-field method" has been developed by [43], see also [33, 45, 46]. The method allows the computational grid to be larger than the theoretical interface thickness, hence significantly coarser meshes can be used compared to the conventional phase-field method, and thus larger physical domains can be effectively simulated. However, the method relies on the notion of the discrete gradient, which is limited to the finite difference method and does not generalize to other discretization techniques, in particular, to the finite-element method.

In this thesis, the mentioned limitations of the phase-field method are addressed from a different perspective. Focusing on microstructure evolution problems involving elastic interactions and on the finite element method for spatial discretization, a hybrid diffuse–semisharp approach is proposed. It is presented in detail in Chapter 5, after [34]. The microstructure, including diffuse interfaces and their evolution, is described in a phase-field-like fashion using a continuous order parameter, and the order parameter plays the role of a level-set function that implicitly defines the position of the sharp interfaces. Considering that the position of the interfaces is arbitrary (and changes in a continuous manner), a fixed finite-element mesh does not conform to those sharp interfaces. To solve the corresponding mechanical equilibrium subproblem, a semisharp approach, namely the laminated element technique (LET), presented in detail in Chapter 4, is employed. In this approach, the elements that are cut by an interface are treated as laminates of the two involved phases, so that the interface-affected

elements create a thin (one element thick) layer of elements between the two phases, and the method can thus be classified as semisharp. In the present context, it is an important feature of LET that the response is a continuous function of the position and orientation of the interface, hence the method is suitable for problems involving moving interfaces.

3. Preliminaries

3.1. Two-phase body with a material weak discontinuity

This section presents the basic equations of continuum mechanics for a body composed of two phases separated by a surface of weak discontinuity, also referred to as an *interface*, where there is a sudden change in material properties. The term "phases" denotes distinct and homogeneous regions of the system separated by the interfaces and having their mechanical properties defined.

The first two subsections present the equations for both finite- and small-strain frameworks, while the final subsection provides a general approach to modelling such systems using the finite element method.

3.1.1. Finite-strain framework

Consider a body occupying, in the reference configuration, the domain Ω, see Fig. 3.1. The body consists of the two phases, occupying the subdomains Ω_1 and Ω_2, respectively, that are separated by the interface $\Gamma = \Omega_1 \cap \Omega_2$. Thermal influences and interfacial energy are neglected. Within both phases, the material properties are assumed to be homogeneous. The interface Γ dividing the body is assumed to be smooth and its direction at each point is denoted by the unit normal vector $\boldsymbol{N}$ pointing from Ω_1 to Ω_2.

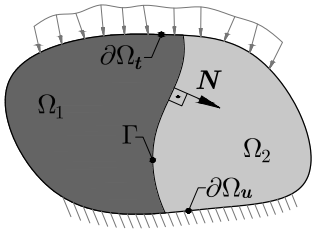

Fig. 3.1. The scheme of the two-phase body with the material interface occupying the domain Ω in the reference configuration.

Deformation of the body is described by the deformation mapping $\boldsymbol{\varphi}$ such that $\boldsymbol{x} = \boldsymbol{\varphi}(\boldsymbol{X}) = \boldsymbol{X} + \boldsymbol{u}(\boldsymbol{X})$ where $\boldsymbol{X}$ and $\boldsymbol{x}$ denote the position of a material point in the reference and current configuration, respectively, and $\boldsymbol{u}$ is the displacement field. The deformation mapping is assumed to be continuously differentiable in

Ω_1 and in Ω_2 and continuous on Γ. The deformation gradient $\boldsymbol{F} = \nabla\boldsymbol{\varphi}$ can thus be defined in Ω_1 and in Ω_2, while continuity of $\boldsymbol{\varphi}$ implies the following *kinematic compatibility condition*, e.g. [136],

$$[\![\boldsymbol{F}]\!] = \boldsymbol{c} \otimes \boldsymbol{N} \quad \text{on } \Gamma, \tag{3.1}$$

where $[\![\square]\!] = (\square)_2 - (\square)_1$ denotes the jump of the quantity $\square$ at the interface Γ, $\boldsymbol{c}$ is a vector and $\otimes$ denotes the diadic product.

The isothermal Helmholtz free energy density function (per unit volume) can be written, separately for the i-th phase, in the following form

$$\psi_i(\boldsymbol{F}) = \psi_i^0 + \psi_i^{\mathrm{el}}(\boldsymbol{F}), \tag{3.2}$$

where ψ_i^0 is the chemical energy component (the energy in the stress-free state) and $\psi_i^{\mathrm{el}}(\boldsymbol{F})$ is the elastic strain energy part. In the case of finite deformations, the potential ψ_i is a function of the deformation gradient, which depends on the constitutive model that is used. Assuming the hyperelastic material, the local constitutive equation takes the form

$$\boldsymbol{P} = \frac{\partial \psi_i}{\partial \boldsymbol{F}} \quad \text{in } \Omega \setminus \Gamma, \tag{3.3}$$

where $\boldsymbol{P} = J\boldsymbol{\sigma}\boldsymbol{F}^{-T}$ is the first Piola–Kirchhoff stress tensor, defined in terms of the Jacobian determinant $J = \det \boldsymbol{F}$ and the Cauchy stress tensor $\boldsymbol{\sigma}$. It is worth noting that relation (3.3) is not determined on the interface Γ, as a jump in the stress field can be expected there due to a sudden change in material properties. However, preserving the equilibrium at the interface Γ necessitates fulfilling the second compatibility condition – *the continuity of the stress vector*

$$[\![\boldsymbol{P}]\!] \cdot \boldsymbol{N} = \boldsymbol{0} \quad \text{on } \Gamma. \tag{3.4}$$

Having the stress field defined, the equilibrium equation in the strong form can be formulated

$$\operatorname{Div} \boldsymbol{P} = \boldsymbol{0} \quad \text{in } \Omega \setminus \Gamma, \qquad \begin{cases} \boldsymbol{u} = \boldsymbol{u}^* & \text{on } \partial\Omega_{\boldsymbol{u}}, \\ \boldsymbol{P} \cdot \boldsymbol{\nu} = \boldsymbol{T}^* & \text{on } \partial\Omega_{\boldsymbol{t}}, \end{cases} \tag{3.5}$$

where $\boldsymbol{u}^*$ and $\boldsymbol{T}^*$ denote the prescribed displacement and traction on the boundaries $\partial\Omega_{\boldsymbol{u}}$ and $\partial\Omega_{\boldsymbol{t}}$, respectively, and $\boldsymbol{\nu}$ stands for the unit outer normal to Ω. Here, to indicate that the differentiating proceeds with respect to the reference configuration, the divergence operator is written with a capital letter.

3.1.2. Small-strain framework

The set of equations within the small-strain framework will not fundamentally differ from those mentioned in the previous chapter. In this case, no distinction is made between the reference and current configurations and hence the position of a material point in both configurations is the same, namely $\boldsymbol{x} \approx \boldsymbol{X}$. The deformation of the body is described by the displacement field $\boldsymbol{u}$ and the measure of deformations is the infinitesimal strain tensor $\boldsymbol{\varepsilon}$, which is the symmetric part of the displacement gradient

$$\boldsymbol{\varepsilon} = \nabla_{\mathrm{s}} \boldsymbol{u} = \frac{1}{2}\left(\nabla \boldsymbol{u} + (\nabla \boldsymbol{u})^{\mathrm{T}}\right) \quad \text{in } \Omega \setminus \Gamma. \tag{3.6}$$

Also, the kinematic compatibility condition takes the form of the symmetric part of the dyadic product

$$[\![\boldsymbol{\varepsilon}]\!] = \frac{1}{2}\left(\boldsymbol{c} \otimes \boldsymbol{n} + \boldsymbol{n} \otimes \boldsymbol{c}\right) \quad \text{on } \Gamma, \tag{3.7}$$

where $\boldsymbol{n}$ stands for the unit normal of the interface Γ pointing from Ω_1 to Ω_2. Note that the jump of the displacement gradient is expressed as $[\![\nabla \boldsymbol{u}]\!] = \boldsymbol{c} \otimes \boldsymbol{n}$.

Analogically, the isothermal Helmholtz free energy density function for i-th phase takes the form

$$\psi_i(\boldsymbol{\varepsilon}) = \psi_i^0 + \psi_i^{\mathrm{el}}(\boldsymbol{\varepsilon}). \tag{3.8}$$

In the case of the small-strain framework, the elastic strain energy component is expressed as

$$\psi_i^{\mathrm{el}}(\boldsymbol{\varepsilon}) = \frac{1}{2}(\boldsymbol{\varepsilon} - \boldsymbol{\varepsilon}_i^{\mathrm{t}}) : \mathbb{L}_i : (\boldsymbol{\varepsilon} - \boldsymbol{\varepsilon}_i^{\mathrm{t}}), \tag{3.9}$$

where $\mathbb{L}_i$ is the fourth-order elastic moduli tensor and $\boldsymbol{\varepsilon}_i^{\mathrm{t}}$ is the transformation strain (known and constant within each phase) of the i-th phase. Then, the local constitutive equation takes the following form

$$\boldsymbol{\sigma} = \frac{\partial \psi_i}{\partial \boldsymbol{\varepsilon}} = \mathbb{L}_i : (\boldsymbol{\varepsilon} - \boldsymbol{\varepsilon}_i^{\mathrm{t}}) \quad \text{in } \Omega \setminus \Gamma, \tag{3.10}$$

where $\boldsymbol{\sigma}$ is the Cauchy stress tensor. The second compatibility condition (the continuity of the traction on the interface) is preserved by fulfilling the equation

$$[\![\boldsymbol{\sigma}]\!] \cdot \boldsymbol{n} = \boldsymbol{0} \quad \text{on } \Gamma. \tag{3.11}$$

The strong form of the equilibrium equation is defined as follows

$$\operatorname{div} \boldsymbol{\sigma} = \boldsymbol{0} \quad \text{in } \Omega \setminus \Gamma, \qquad \begin{cases} \boldsymbol{u} = \boldsymbol{u}^* & \text{on } \partial\Omega_{\boldsymbol{u}}, \\ \boldsymbol{\sigma} \cdot \boldsymbol{\nu} = \boldsymbol{t}^* & \text{on } \partial\Omega_{\boldsymbol{t}}, \end{cases} \tag{3.12}$$

where $\boldsymbol{t}^*$ is the prescribed surface traction.

3.1.3. Finite-element treatment

To establish the finite-element formulation, the weak form of the equilibrium equation is required. To achieve this, first introduce the kinematically admissible displacement field

$$\boldsymbol{u}_\zeta = \boldsymbol{u} + \zeta\boldsymbol{\eta}, \tag{3.13}$$

where $\boldsymbol{u}$ is the displacement field fulfilling the equilibrium equation (the *real* one), ζ is a scalar and $\boldsymbol{\eta}$ stands for any vector field vanishing on the boundary $\partial\Omega_{\boldsymbol{u}}$, where the displacement is prescribed. The term $\zeta\boldsymbol{\eta}$ in the above equation is commonly referred to as the *perturbation* of the displacement field $\boldsymbol{u}$, with ζ indicating the scale and $\boldsymbol{\eta}$ representing the direction of this perturbation. The *virtual displacement* (or so-called *test function*) is then defined as follows

$$\delta\boldsymbol{u} = \frac{\partial\boldsymbol{u}_\zeta}{\partial\zeta}\,\mathrm{d}\zeta = \boldsymbol{\eta}\,\mathrm{d}\zeta. \tag{3.14}$$

For the sake of convenience and practicality, the more usual way of calculating the variations of any field or functional in mechanics is to use the formalism of Gateaux derivative. Assuming $\boldsymbol{u}_\epsilon$ expresses the family of kinematically admissible displacement fields of one parameter ϵ, where $\boldsymbol{u}_\epsilon|_{\epsilon=0} = \boldsymbol{u}$ fulfils the equilibrium equation, the virtual displacement is then calculated in the following way

$$\delta\boldsymbol{u} = \left.\frac{\mathrm{d}}{\mathrm{d}\epsilon}\boldsymbol{u}_\epsilon\right|_{\epsilon=0}. \tag{3.15}$$

Essentially, $\delta\boldsymbol{u}$ represents an infinitesimal perturbation of the displacement field $\boldsymbol{u}$. Assuming that the field $\boldsymbol{u}_\epsilon$ is kinematically admissible, the variation $\delta\boldsymbol{u}$ must also conform to the conditions of kinematic admissibility. As a result, it must possess differentiability throughout the entire domain Ω, except for the interface Γ, where it can suffer a weak discontinuity.

Finite-strain framework

The weak form of the equilibrium equation is obtained in a rather standard manner – by multiplying the strong form of the equilibrium equation $(3.5)_1$ by the test function $\delta\boldsymbol{u}$ and integrating over the whole domain, consequently. Owing to the discontinuity of the deformation at the interface Γ, it is expressed as follows

$$\int_{\Omega_1} \mathrm{Div}\,\boldsymbol{P}\cdot\delta\boldsymbol{u}\,\mathrm{d}V + \int_{\Omega_2} \mathrm{Div}\,\boldsymbol{P}\cdot\delta\boldsymbol{u}\,\mathrm{d}V = 0 \qquad \forall\,\delta\boldsymbol{u}. \tag{3.16}$$

Using rather standard mathematical operations, such as employing the divergence theorem and applying integration by parts, the integral for the i-th phase can be rewritten as

$$\int_{\Omega_i} \mathrm{Div}\, \boldsymbol{P}\cdot\delta\boldsymbol{u}\,\mathrm{d}V = \int_{\Omega_i} \boldsymbol{P} : \mathrm{Grad}\,\delta\boldsymbol{u}\,\mathrm{d}V - \int_{\Gamma} \delta\boldsymbol{u}\cdot\boldsymbol{P}\cdot\boldsymbol{N}_i\,\mathrm{d}S - \int_{\partial\Omega_{i,\boldsymbol{t}}} \boldsymbol{T}^*\cdot\delta\boldsymbol{u}\,\mathrm{d}S, \quad (3.17)$$

where $\boldsymbol{N}_i$ is the outward-pointing unit normal on the boundary Γ of the phase i. Here, similar to before, to emphasize that the differentiation is carried out in the reference configuration, the gradient operator is written in uppercase. Since $\partial\Omega_{\boldsymbol{t}} = \partial\Omega_{1,\boldsymbol{t}} \cup \partial\Omega_{2,\boldsymbol{t}}$ and $\boldsymbol{N}_1 = -\boldsymbol{N}_2 = \boldsymbol{N}$, the weak form takes the following form

$$\sum_{i=1}^{2} \int_{\Omega_i} \boldsymbol{P} : \mathrm{Grad}\,\delta\boldsymbol{u}\,\mathrm{d}V + \underbrace{\int_{\Gamma} \delta\boldsymbol{u}\cdot[\![\boldsymbol{P}]\!]\cdot\boldsymbol{N}\,\mathrm{d}S}_{\substack{=0,\text{ because of the traction}\\ \text{continuity condition (3.4)}}} - \int_{\partial\Omega_{\boldsymbol{t}}} \boldsymbol{T}^*\cdot\delta\boldsymbol{u}\,\mathrm{d}S = 0, \qquad \forall\,\delta\boldsymbol{u}. \quad (3.18)$$

Ensuring the fulfilment of the second compatibility condition at the interface (3.4) results in the elimination of the second term in the equation above. On the other hand, the first compatibility condition (3.1), related to the continuity of the displacement field, is satisfied by the assumption of the continuity of the virtual displacement field. Finally, the weak form of the equilibrium equation is stated as

$$\sum_{i=1}^{2} \int_{\Omega_i} \boldsymbol{P} : \mathrm{Grad}\,\delta\boldsymbol{u}\,\mathrm{d}V - \int_{\partial\Omega_{\boldsymbol{t}}} \boldsymbol{T}^*\cdot\delta\boldsymbol{u}\,\mathrm{d}S = 0, \qquad \forall\,\delta\boldsymbol{u}. \quad (3.19)$$

In the next step, the domain Ω is discretized into the triangulation $\mathcal{T}$. The standard approach when modelling weak discontinuities using the finite element method is to use a *conforming finite-element mesh* in which the mesh matches the interfaces. In such a scenario the triangulation $\mathcal{T}$ of the domain Ω can be partitioned into two disjoint subsets

$$\mathcal{T} = \mathcal{T}_1 \cup \mathcal{T}_2, \quad (3.20)$$

where $\mathcal{T}_1$ and $\mathcal{T}_2$ are the sets of finite elements that correspond to subdomains Ω_1 and Ω_2, respectively. The displacement field $\boldsymbol{u}$ is then approximated using the basis functions N_i

$$\boldsymbol{u}^h = \sum_k N_k^{(\boldsymbol{u})} \boldsymbol{u}_k, \quad (3.21)$$

where $\boldsymbol{u}_k$ stands for the displacement of k-th node of the triangulation $\mathcal{T}$ with $\mathbf{p}_{\boldsymbol{u}} = \{\boldsymbol{u}_k\}$ denoting the global vector consisting of all nodal values. As a consequence, the approximation of the virtual displacement used in the weak form (3.19) takes the form

$$\delta\boldsymbol{u}^h = \sum_k N_k^{(\boldsymbol{u})} \delta\boldsymbol{u}_k \quad (3.22)$$

(thus obtaining the Galerkin method) and the other approximated quantities, such as deformation gradient $\boldsymbol{F}^h$ and the first Piola–Kirchhoff stress tensor $\boldsymbol{P}^h$, are then obtained

$$\boldsymbol{F}^h = \boldsymbol{I} + \frac{\partial \boldsymbol{u}^h}{\partial \boldsymbol{X}}, \quad \boldsymbol{P}^h = \boldsymbol{P}(\boldsymbol{F}^h), \tag{3.23}$$

where $\boldsymbol{I}$ is the second-order identity tensor. Following the standard approach, $\boldsymbol{u}^h$ is introduced into the weak form (3.19) and the integration is performed over individual finite elements ω of the triangulation (3.20). Thereby, the discretized weak form of the equilibrium equation takes the form

$$\sum_{i=1}^{2} \left(\sum_{\omega \in \mathcal{T}_i} \int_{\omega} \boldsymbol{P}^h : \operatorname{Grad} \delta \boldsymbol{u}^h \, \mathrm{d}V \right) - \sum_{\partial\omega \in \mathcal{S}_{\boldsymbol{t}}} \int_{\partial\omega} \boldsymbol{T}^* \cdot \delta \boldsymbol{u}^h \, \mathrm{d}S = 0, \qquad \forall\, \delta \mathbf{p}_{\boldsymbol{u}}, \tag{3.24}$$

where $\mathcal{S}_{\boldsymbol{t}}$ denotes the triangulation of the boundary $\partial\Omega_{\boldsymbol{t}}$ into surface segments $\partial\omega$, consistent with the triangulation $\mathcal{T}$ of the bulk. According to the fundamental lemma of the calculus of variations, the obtained variational equation (3.24) defines the set of nonlinear equations that can be written in the following residual form

$$\mathbf{R}_{\boldsymbol{u}}(\mathbf{p}_{\boldsymbol{u}}) = \mathbf{0}. \tag{3.25}$$

The solution of these equations is obtained using the Newton–Raphson method.

Small-strain framework

In the small-strain framework, the weak form of the equilibrium equation retains the same structure, albeit expressed in terms of appropriate measures of strain and stress specific to infinitesimal deformations

$$\sum_{i=1}^{2} \int_{\Omega_i} \boldsymbol{\sigma} : \delta \boldsymbol{\varepsilon} \, \mathrm{d}V - \int_{\partial\Omega_{\boldsymbol{t}}} \boldsymbol{t}^* \cdot \delta \boldsymbol{u} \, \mathrm{d}S = 0, \qquad \forall\, \delta \boldsymbol{u}, \tag{3.26}$$

where $\delta\boldsymbol{\varepsilon} = \nabla_{\mathrm{s}} \delta \boldsymbol{u} = \frac{1}{2}\left(\nabla \delta \boldsymbol{u} + (\nabla \delta \boldsymbol{u})^{\mathrm{T}}\right)$. Following a similar procedure as in the finite-strain framework, and utilizing the same approximation (3.21), one arrives at the discretized weak form of the equilibrium equation:

$$\sum_{i=1}^{2} \left(\sum_{\omega \in \mathcal{T}_i} \int_{\omega} \boldsymbol{\sigma}^h : \delta \boldsymbol{\varepsilon}^h \, \mathrm{d}V \right) - \sum_{\partial\omega \in \mathcal{S}_{\boldsymbol{t}}} \int_{\partial\omega} \boldsymbol{t}^* \cdot \delta \boldsymbol{u}^h \, \mathrm{d}S = 0, \qquad \forall\, \delta \mathbf{p}_{\boldsymbol{u}}, \tag{3.27}$$

where

$$\begin{gathered} \boldsymbol{\varepsilon}^h = \frac{1}{2}\left(\nabla \boldsymbol{u}^h + (\nabla \boldsymbol{u}^h)^{\mathrm{T}}\right), \qquad \boldsymbol{\sigma}^h = \boldsymbol{\sigma}(\boldsymbol{\varepsilon}^h), \\ \delta \boldsymbol{\varepsilon}^h = \frac{1}{2}\left(\nabla \delta \boldsymbol{u}^h + (\nabla \delta \boldsymbol{u}^h)^{\mathrm{T}}\right). \end{gathered} \tag{3.28}$$

Lastly, the set of nonlinear equations defined by the variational equation (3.27) can be written in the residual form (3.25) and is solved using the Newton–Raphson method.

3.2. Two-phase body with a moving weak discontinuity

In this section, moving interfaces are considered. The scenario of an interface in motion is not merely an abstract concept; it can manifest during phase transformations in microstructures. For instance, in the case of martensitic transformations in shape-memory alloys, the moving interface represents a propagating front that separates the two material phases.

Since the numerical examples of moving interfaces presented in the subsequent chapters of this thesis are restricted to cases involving small deformations only, all equations and formulae are demonstrated here within the small-strain framework.

The section is organized as follows: in the first subsection, the classical formulation of the microstructure evolution problem in the sharp-interface framework is presented. Then, a diffuse-interface approach is discussed. The last subsection presents the implementation of the phase-field model in the context of the finite element method.

3.2.1. Reference sharp-interface problem

Consider now that the interface Γ is allowed to move, see Fig. 3.2. For this to be possible, it is necessary to introduce a new physical quantity into the considerations, which will induce this motion. This quantity is the thermodynamic driving force, intricately linked to the change in the position (relative to the material) of the interface in the direction perpendicular to it. It is not a force in the Newtonian sense, meaning it does not cause deformation or motion of the entire body; rather, it is a new type of force referred to in the book by Gurtin [55] as a *configurational force*, which performs work when the microstructure of a material evolves [119]. In this work, as will be formalized later, it is assumed that the position (relative to the material) of a given point on the interface remains

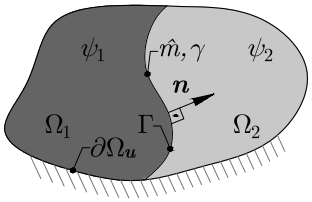

Fig. 3.2. The scheme of the two-phase body with the moving interface Γ occupying the domain Ω in the reference configuration.

unchanged only when the associated local driving force is zero. Therefore, if at every point on the interface Γ, the thermodynamic force equals zero, and moreover, mechanical equilibrium is satisfied at every point of the body, then the body is said to be in thermodynamic equilibrium.

In this thesis, the focus is limited to quasi-static problems, thus omitting inertial effects. Consequently, to derive the formula for the thermodynamic driving force, it is convenient to employ the variational principles of mechanics, as illustrated for finite deformations in the book by Gurtin [55]. The derivation below follows that of Gurtin [55], except that the small-deformation framework is used.

The total free energy of the system is given by the functional

$$\hat{\Psi}\left(\boldsymbol{u}, \Gamma\right) = \int_{\Omega_1} \psi_1 \, \mathrm{d}V + \int_{\Omega_2} \psi_2 \, \mathrm{d}V + \int_{\Gamma} \gamma \, \mathrm{d}S, \tag{3.29}$$

where ψ_i is defined as in Eq. (3.8) and γ is the interfacial energy density (per unit area of the interface Γ) – assumed to be constant in this work. The system is in thermodynamic equilibrium when the displacement field $\boldsymbol{u}$ and the position of the interface Γ minimize the energy functional (3.29). This implies the restriction of the vanishing of the first variation of the total free energy with respect to the perturbation of both the displacement $\delta\boldsymbol{u}$ and the position of the interface $\delta\Gamma$, namely

$$\delta\hat{\Psi}\left(\boldsymbol{u}, \Gamma\right) = \frac{\mathrm{d}}{\mathrm{d}\epsilon}\delta\hat{\Psi}\left(\boldsymbol{u}_\epsilon, \Gamma_\epsilon\right)\bigg|_{\epsilon=0} = 0, \qquad \forall\delta\boldsymbol{u}\,\forall\delta\Gamma. \tag{3.30}$$

The virtual displacement $\delta\boldsymbol{u}$ is defined as in the formula (3.15), while the perturbation of the position of the interface $\delta\Gamma$ is stated as follows: assume that Γ_ϵ expresses the family of interfaces that depend on ϵ in a continuous manner and is such that $\Gamma_\epsilon = \Gamma$ at $\epsilon = 0$. Furthermore, Γ_ϵ is parameterized by $\boldsymbol{X} = \boldsymbol{X}_\epsilon(\xi_1, \xi_2)$. The variation $\delta\Gamma$ is then defined as a normal part (a scalar field) of the variation of Γ

$$\delta\Gamma = \boldsymbol{n} \cdot \frac{\mathrm{d}}{\mathrm{d}\epsilon}\boldsymbol{X}_\epsilon(\xi_1, \xi_2)\bigg|_{\epsilon=0}. \tag{3.31}$$

Due to the linearity of the variation operator, the variation of the total free energy can be rewritten in the form

$$\delta\hat{\Psi}\left(\boldsymbol{u}, \Gamma\right) = \delta\left(\int_{\Omega_1} \psi_1 \, \mathrm{d}V\right) + \delta\left(\int_{\Omega_2} \psi_2 \, \mathrm{d}V\right) + \delta\left(\int_{\Gamma} \gamma \, \mathrm{d}S\right). \tag{3.32}$$

Because the internal geometry of the body is changing due to the variation $\delta\Gamma$, this fact should be taken into account when calculating the variations of the above

functionals. The following formulae for the related perturbations in the integration domains will serve as a support for further derivations, see also Fig. 3.3,

$$\sum_{i=1}^{2} \delta \left(\int_{\Omega_i} \mathrm{d}V \right) = \sum_{i=1}^{2} \left((-1)^{i+1} \int_{\Gamma} \delta\Gamma \, \mathrm{d}S \right), \quad \delta \left(\int_{\Gamma} \mathrm{d}S \right) = - \int_{\Gamma} \kappa \delta\Gamma \, \mathrm{d}S, \tag{3.33}$$

where κ is the total curvature (i.e., twice the mean curvature) at a given point of the interface Γ. By incorporating the above, the bulk components yield

$$\begin{aligned} \sum_{i=1}^{2} \delta \left(\int_{\Omega_i} \psi_i \, \mathrm{d}V \right) &= \sum_{i=1}^{2} \left(\int_{\Omega_i} \frac{\partial \psi_i}{\partial \boldsymbol{\varepsilon}} : \delta\boldsymbol{\varepsilon} \, \mathrm{d}V + (-1)^{i+1} \int_{\Gamma} \psi_i \delta\Gamma \, \mathrm{d}S \right) \\ &= \sum_{i=1}^{2} \int_{\Omega_i} \boldsymbol{\sigma} : \nabla \delta\boldsymbol{u} - \int_{\Gamma} [\![\psi]\!] \delta\Gamma \, \mathrm{d}S, \end{aligned} \tag{3.34}$$

whereas the variation of the interfacial part results in

$$\delta \left(\int_{\Gamma} \gamma \, \mathrm{d}S \right) = - \int_{\Gamma} \gamma\kappa \delta\Gamma \, \mathrm{d}S. \tag{3.35}$$

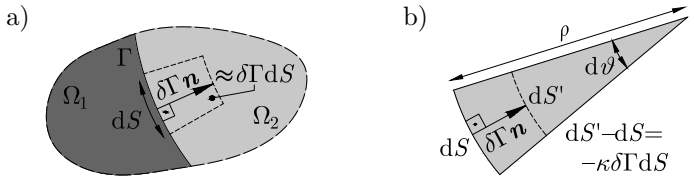

Fig. 3.3. The supplementary 2D sketch illustrating the perturbations in the integration domains related to the perturbation of the interface Γ. The subfigures show the geometrical relation for the perturbation of: a) the volume and b) the interface surface, where κ is the curvature at a given point of Γ (for 3D case, κ is twice the mean curvature).

By successively applying integration by parts, the divergence theorem and the identity $[\![fg]\!] = \langle f \rangle [\![g]\!] + [\![f]\!] \langle g \rangle$, where $\langle \square \rangle = \frac{1}{2}(\square_1 + \square_2)$ represents the average of the interfacial limits of $\square$, the variation of the total free energy (3.32) then gives consequently

$$\begin{aligned} \delta\hat{\Psi}(\boldsymbol{u}, \Gamma) &= - \sum_{i=1}^{2} \int_{\Omega_i} \delta\boldsymbol{u} \cdot \operatorname{div} \boldsymbol{\sigma} \, \mathrm{d}V - \int_{\Gamma} \left(\langle \delta\boldsymbol{u} \rangle \cdot [\![\boldsymbol{\sigma}]\!] \cdot \boldsymbol{n} + [\![\delta\boldsymbol{u}]\!] \cdot \langle \boldsymbol{\sigma} \rangle \cdot \boldsymbol{n} \right) \mathrm{d}S \\ &\quad - \int_{\Gamma} \left([\![\psi]\!] + \gamma\kappa \right) \delta\Gamma \, \mathrm{d}S. \end{aligned} \tag{3.36}$$

Due to the compatibility condition, the displacement field and therefore the virtual displacement must be continuous,

$$\delta \boldsymbol{u}_1 + \nabla \boldsymbol{u}_1 \cdot (\delta\Gamma \boldsymbol{n}) = \delta \boldsymbol{u}_2 + \nabla \boldsymbol{u}_2 \cdot (\delta\Gamma \boldsymbol{n}), \tag{3.37}$$

which can be rewritten in the form:

$$[\![\delta \boldsymbol{u}]\!] = -\delta\Gamma [\![\nabla \boldsymbol{u}]\!] \cdot \boldsymbol{n}. \tag{3.38}$$

Applying (3.38) to the (3.36) finally gives

$$\begin{aligned} \delta\hat{\Psi}(\boldsymbol{u}, \Gamma) \;=\; & -\int_{\Omega_1} (\operatorname{div} \boldsymbol{\sigma}) \cdot \delta \boldsymbol{u} \, \mathrm{d}V - \int_{\Omega_2} (\operatorname{div} \boldsymbol{\sigma}) \cdot \delta \boldsymbol{u} \, \mathrm{d}V - \int_{\Gamma} ([\![\boldsymbol{\sigma}]\!] \cdot \boldsymbol{n}) \cdot \langle \delta \boldsymbol{u} \rangle \, \mathrm{d}S \\ & - \int_{\Gamma} \big([\![\psi]\!] - (\langle \boldsymbol{\sigma} \rangle \cdot \boldsymbol{n}) \cdot ([\![\nabla \boldsymbol{u}]\!] \cdot \boldsymbol{n}) + \gamma\kappa \big) \delta\Gamma \, \mathrm{d}S. \end{aligned} \tag{3.39}$$

The vanishing of the variation of the total free energy for any perturbations $\delta \boldsymbol{u}$ and $\delta\Gamma$, as stated in (3.30), leads to significant implications. The first three integrals in (3.39) represent the equilibrium equations governing a two-phase body with a material (non-moving) interface. These equilibrium equations were previously presented in (3.11) and (3.12). On the other hand, the last integral provides an additional condition, which is associated with the motion of the interface, namely

$$[\![\psi]\!] - (\langle \boldsymbol{\sigma} \rangle \cdot \boldsymbol{n}) \cdot ([\![\nabla \boldsymbol{u}]\!] \cdot \boldsymbol{n}) + \gamma\kappa = 0, \tag{3.40}$$

which is often referred to as the *Maxwell relation*. This condition, together with the equilibrium equations, guarantees that the body is in thermodynamic equilibrium. Thus, the left-hand side of Eq. (3.40) defines the thermodynamic driving force. Taking into account the continuity of the displacement field (3.7) and the symmetry of the stress tensor $\boldsymbol{\sigma}$, the expression for this force can be elegantly expressed as follows

$$\hat{f} = [\![\psi]\!] - \langle \boldsymbol{\sigma} \rangle : [\![\boldsymbol{\varepsilon}]\!] + \gamma\kappa. \tag{3.41}$$

Furthermore, it is worth noting that in this expression, the term $\langle \boldsymbol{\sigma} \rangle$ can be replaced with $\boldsymbol{\sigma}_1$ or $\boldsymbol{\sigma}_2$ due to the traction continuity condition (3.11) at the interface Γ. Finally, the above formula can be grouped and expressed in a more concise way

$$\hat{f} = \hat{f}_{\text{bulk}} + \hat{f}_{\text{int}}, \tag{3.42}$$

where

$$\hat{f}_{\text{bulk}} = [\![\psi]\!] - \langle \boldsymbol{\sigma} \rangle : [\![\boldsymbol{\varepsilon}]\!], \qquad \hat{f}_{\text{int}} = \gamma\kappa \tag{3.43}$$

are the driving forces related exclusively to the bulk and the interfacial energy, respectively. The obtained expression for the bulk-related thermodynamic driving force $(3.43)_1$ is consistent with the formulas found in the literature, cf. [1]. It is also worth mentioning that it can be derived from the Eshelby stress tensor [41], see also [79]. Indeed, if the small-strain Eshelby stress tensor is given by

$$\boldsymbol{\Sigma} = \psi \boldsymbol{I} - (\nabla \boldsymbol{u})^{\mathrm{T}} \cdot \boldsymbol{\sigma}, \tag{3.44}$$

then the normal component of the jump of the Eshelby stress tensor provides

$$\begin{aligned} \boldsymbol{n} \cdot [\![\boldsymbol{\Sigma}]\!] \cdot \boldsymbol{n} &= [\![\psi]\!] - \boldsymbol{n} \cdot [\![(\nabla \boldsymbol{u})^{\mathrm{T}} \cdot \boldsymbol{\sigma}]\!] \cdot \boldsymbol{n} \\ &= [\![\psi]\!] - \boldsymbol{n} \cdot \big([\![\nabla \boldsymbol{u}]\!]^{\mathrm{T}} \cdot \langle \boldsymbol{\sigma} \rangle\big) \cdot \boldsymbol{n} - \boldsymbol{n} \cdot \big(\langle \nabla \boldsymbol{u} \rangle^{\mathrm{T}} \cdot [\![\boldsymbol{\sigma}]\!]\big) \cdot \boldsymbol{n}. \end{aligned} \tag{3.45}$$

In view of the condition (3.11), the last component vanishes in the above equation and the remaining part can be rewritten as

$$\boldsymbol{n} \cdot [\![\boldsymbol{\Sigma}]\!] \cdot \boldsymbol{n} = [\![\psi]\!] - (\langle \boldsymbol{\sigma} \rangle \cdot \boldsymbol{n}) \cdot ([\![\nabla \boldsymbol{u}]\!] \cdot \boldsymbol{n}), \tag{3.46}$$

which leads to the conclusion that

$$\hat{f}_{\mathrm{bulk}} = \boldsymbol{n} \cdot [\![\boldsymbol{\Sigma}]\!] \cdot \boldsymbol{n} = [\![\psi]\!] - \langle \boldsymbol{\sigma} \rangle : [\![\boldsymbol{\varepsilon}]\!]. \tag{3.47}$$

Now that the thermodynamic driving force has been defined, the kinetic law for the interface can be proposed. Viscous dissipation is commonly employed in phase-field models. Of course, examples can be found where other types of dissipation are used, see [54, 125, 160]. However, such applications are relatively scarce in the context of the phase-field method. In this thesis, as mentioned in the introduction of this section, the considerations are limited to the case of viscous dissipation. Consequently, the kinetic law for the interface Γ is then defined,

$$\hat{v}_n = \hat{m} \hat{f}, \tag{3.48}$$

where $\hat{v}_n$ is the interface speed in the normal direction $\boldsymbol{n}$, $\hat{m}$ is the interface mobility and $\hat{f}$ is the local thermodynamic driving force (3.41), associated with the propagating interface. While the interface mobility is an arbitrary parameter exclusively tied to the interface property, the thermodynamic driving force is additionally influenced by the deformation in proximity to the interface.

Direct computational (e.g., finite-element) treatment of the microstructure evolution problem within the sharp-interface framework is not straightforward because it would require remeshing to ensure that the mesh matches the evolving microstructure. A feasible approach to model moving interfaces is thus to adopt a diffuse-interface approximation independent of the spatial discretization, which is discussed next.

3.2.2. Diffuse-interface framework*

The sharp-interface problem discussed in the preceding section can be approximated by adopting a diffuse-interface description using the phase-field method. To this end, a continuous order parameter ϕ, $0 \leq \phi \leq 1$, is introduced such that $\phi = 0$ corresponds to phase 1 and $\phi = 1$ to phase 2, while the intermediate values correspond to the diffuse interface, see Fig. 3.4.

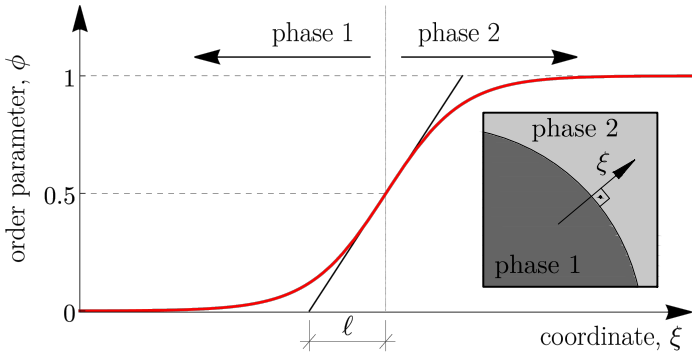

Fig. 3.4. The order parameter profile, denoted with a red solid line, representing the diffuse interface between two phases.

Accordingly, the Helmholtz free energy ψ, characterizing both the individual phases and the diffuse interface, is assumed to be a function of the strain $\boldsymbol{\varepsilon}$ and of the order parameter ϕ and its spatial gradient $\nabla\phi$, and comprises the bulk and interfacial energy contributions, ψ_{bulk} and ψ_{int}, respectively,

$$\psi(\boldsymbol{\varepsilon}, \phi, \nabla\phi) = \psi_{\text{bulk}}(\boldsymbol{\varepsilon}, \phi) + \psi_{\text{int}}(\phi, \nabla\phi). \tag{3.49}$$

The bulk energy contribution ψ_{bulk} is specified as

$$\psi_{\text{bulk}}(\boldsymbol{\varepsilon}, \phi) = \psi^0(\phi) + \frac{1}{2}(\boldsymbol{\varepsilon} - \boldsymbol{\varepsilon}^{\text{t}}(\phi)) : \mathbb{L}(\phi) : (\boldsymbol{\varepsilon} - \boldsymbol{\varepsilon}^{\text{t}}(\phi)), \tag{3.50}$$

where

$$\begin{gathered} \psi^0(\phi) = (1 - h(\phi))\psi_1^0 + h(\phi)\psi_2^0, \qquad \boldsymbol{\varepsilon}^{\text{t}}(\phi) = (1 - h(\phi))\boldsymbol{\varepsilon}_1^{\text{t}} + h(\phi)\boldsymbol{\varepsilon}_2^{\text{t}}, \\ \mathbb{L}(\phi) = (1 - h(\phi))\mathbb{L}_1 + h(\phi)\mathbb{L}_2. \end{gathered} \tag{3.51}$$

Here, in contrast to (3.8) and (3.9), the chemical energy ψ^0, the transformation strain $\boldsymbol{\varepsilon}^{\text{t}}$ and the elastic stiffness tensor $\mathbb{L}$ depend on the order parameter ϕ

*The content of this section has been entirely excerpted from the article of Dobrzański and Stupkiewicz [34]. Minor modifications may have been applied to the text and figures.

through the weighting function $h(\phi)$ such that $h(0) = 0$, $h(1) = 1$, and $h'(0) = h'(1) = 0$. The popular *2-3-4 polynomial*, $h(\phi) = 3\phi^2 - 2\phi^3$ (with $\alpha = 3$), is adopted here, see [85, 142].

The interfacial energy contribution ψ_{int} is taken in the form of the so-called double-well potential [142],

$$\psi_{\text{int}}(\phi, \nabla\phi) = \frac{6\gamma}{\ell}\left(\phi^2(1-\phi)^2 + \frac{\ell^2}{4}\nabla\phi\cdot\nabla\phi\right), \tag{3.52}$$

where γ is the interfacial energy, see (3.29), and ℓ is the interface thickness parameter, see Fig. 3.4. Note that, when $\phi = 0$, the bulk energy (3.50) reduces to ψ_1, i.e., to the free energy specified by (3.8) for the pure phase 1, and likewise for the free energy ψ_2 of the pure phase 2 when $\phi = 1$.

In the phase-field method, the interfaces are treated as diffuse hence the discontinuities at the interfaces are smeared out and the compatibility conditions (3.7) and (3.11) need not be considered. Since the strains and stresses are continuous, the mechanical equilibrium equation holds in the entire domain Ω, i.e., also within the diffuse interface,

$$\operatorname{div}\boldsymbol{\sigma} = \mathbf{0} \quad \text{in } \Omega, \tag{3.53}$$

with $\boldsymbol{\sigma} = \partial\psi/\partial\boldsymbol{\varepsilon} = \mathbb{L}(\phi) : (\boldsymbol{\varepsilon} - \boldsymbol{\varepsilon}^{\text{t}}(\phi))$, subject to the boundary conditions $(3.12)_2$.

Evolution of the microstructure is governed by the time-dependent Ginzburg–Landau equation [24, 117],

$$\dot{\phi} = -m\frac{\delta\Psi}{\delta\phi}, \qquad \frac{\delta\Psi}{\delta\phi} = \frac{\partial\psi}{\partial\phi} - \nabla\cdot\frac{\partial\psi}{\partial\nabla\phi}, \tag{3.54}$$

where $\delta\Psi/\delta\phi$ is the variational derivative of the total free energy functional $\Psi = \int_\Omega \psi \mathrm{d}V$, and m is the mobility parameter. Homogeneous Neumann boundary conditions are assumed on the entire boundary,

$$\nabla\phi\cdot\boldsymbol{\nu} = 0 \quad \text{on } \partial\Omega. \tag{3.55}$$

It can be shown that the equilibrium profile of the diffuse interface has the following form [58],

$$\phi(\xi) = \frac{1}{2}\tanh\left(\frac{\xi - \xi_0}{\ell}\right) + \frac{1}{2}, \tag{3.56}$$

which can be obtained by minimizing the total interfacial energy $\Psi_{\text{int}} = \int_\Omega \psi_{\text{int}} \mathrm{d}V$ of a planar interface located at $\xi = \xi_0$ (i.e., $\phi(\xi_0) = \frac{1}{2}$), where ξ denotes the coordinate in the direction normal to the interface. This profile is only an approximation of the actual profile when the interface is non-planar or when the

interface propagates due to a mechanical driving force that is not constant within the interface. In fact, special conditions must be met so that a travelling wave solution is obtained with the interface profile independent of the velocity [142].

Adopting the equilibrium profile (3.56) as an approximation of the actual profile, the mobility parameter m in the evolution equation (3.54) can be related to the mobility parameter $\hat{m}$ in the sharp-interface description, cf. Eq. (3.48). By equating the energy dissipated at the propagating sharp interface to that dissipated within the diffuse interface propagating with the same velocity, thus $\hat{f}\hat{v}_n = \hat{v}_n^2/\hat{m} = \int_{-\infty}^{+\infty} (\dot{\phi}^2/m)\mathrm{d}\xi$, where $\xi_0 = \hat{v}_n t$, the following relationship is found,

$$\hat{m} = 3m\ell. \tag{3.57}$$

It follows that when the interface parameter ℓ is varied then the mobility parameter m must be scaled according to (3.57) so that the effective mobility $\hat{m}$ of the interface is not affected (to the first order, in view of the approximate profile of the diffuse interface).

It is worth noting that in the case of using the double-well potential (3.52), the effective interface thickness, i.e., the region where the contribution of each of the two phases is non-negligible, cannot be precisely defined. It is related to the fact that the profile of the diffuse interface (3.56) is a function that asymptotically approaches extreme values 0 and 1. Nevertheless, based on the hyperbolic tangent function (3.56), one can estimate the theoretical effective thickness to be 4ℓ.

3.2.3. Finite-element treatment of the phase-field model

In order to arrive at the finite-element formulation, the mechanical equilibrium equation (3.53) is expressed in a weak form by following the standard procedure,

$$\int_\Omega \boldsymbol{\sigma} : \delta\boldsymbol{\varepsilon}\,\mathrm{d}V - \int_{\partial\Omega_{\boldsymbol{t}}} \boldsymbol{t}^* \cdot \delta\boldsymbol{u}\,\mathrm{d}S = 0, \qquad \forall\,\delta\boldsymbol{u}, \tag{3.58}$$

where $\delta\boldsymbol{\varepsilon} = \nabla_{\mathrm{s}}\delta\boldsymbol{u}$, and $\delta\boldsymbol{u}$ is the virtual displacement (test function) that vanishes, $\delta\boldsymbol{u} = \boldsymbol{0}$, on $\partial\Omega_{\boldsymbol{u}}$. Likewise, the evolution equation (3.54) is expressed in a weak form,

$$\int_\Omega \left[\left(\frac{\dot{\phi}}{m} + \frac{\partial\psi_{\mathrm{bulk}}}{\partial\phi} + \frac{\partial\psi_{\mathrm{int}}}{\partial\phi}\right)\delta\phi + \frac{\partial\psi_{\mathrm{int}}}{\partial\nabla\phi}\cdot\nabla\delta\phi\right]\mathrm{d}V = 0, \qquad \forall\,\delta\phi, \tag{3.59}$$

where $\delta\phi$ is the respective test function and

$$\frac{\partial\psi_{\mathrm{bulk}}}{\partial\phi} = \left(\llbracket\phi^0\rrbracket - \boldsymbol{\sigma} : \llbracket\boldsymbol{\varepsilon}^{\mathrm{t}}\rrbracket + \frac{1}{2}(\boldsymbol{\varepsilon} - \boldsymbol{\varepsilon}^{\mathrm{t}}(\phi)) : \llbracket\mathbb{L}\rrbracket : (\boldsymbol{\varepsilon} - \boldsymbol{\varepsilon}^{\mathrm{t}}(\phi))\right) h'(\phi), \tag{3.60}$$

$$\frac{\partial \psi_{\mathrm{int}}}{\partial \phi} = \frac{12\gamma}{\ell}\phi(1-\phi)(1-2\phi), \qquad \frac{\partial \psi_{\mathrm{int}}}{\partial \nabla\phi} = 3\gamma\ell\,\nabla\phi, \tag{3.61}$$

where $[\![\square]\!] = (\square)_2 - (\square)_1$.

The incremental (time-discrete) form of the evolution equation (3.59) is obtained by applying the implicit backward-Euler time integration scheme. Considering a typical time increment $t_n \to t_{n+1} = t_n + \tau$, the rate of ϕ is thus approximated by its finite-difference approximation,

$$\dot{\phi} \approx \frac{1}{\tau}(\phi - \phi_n), \tag{3.62}$$

where ϕ_n is the known value at the previous time step t_n, and $\phi = \phi_{n+1}$ is the unknown value at the current time step. Here and below, to make the notation more compact, the subscript $n+1$ is omitted for the quantities evaluated at the current time step t_{n+1}. Adopting this notation, the time-discrete problem at t_{n+1} is given directly by the weak forms (3.58) and (3.59) with $\dot{\phi}$ replaced in (3.59) by its finite-difference approximation (3.62).

Spatial discretization is performed using the finite element method. The fields of displacement $\boldsymbol{u}$ and order parameter ϕ are approximated using the respective basis functions $N_k^{(\boldsymbol{u})}$ and $N_k^{(\phi)}$,

$$\boldsymbol{u}^h = \sum_k N_k^{(\boldsymbol{u})}\boldsymbol{u}_k, \qquad \phi^h = \sum_k N_k^{(\phi)}\phi_k, \tag{3.63}$$

where $\boldsymbol{u}_k$ and ϕ_k denote the respective nodal values with $\mathbf{p}_{\boldsymbol{u}} = \{\boldsymbol{u}_k\}$ and $\mathbf{p}_\phi = \{\phi_k\}$ denoting the global vectors. Following the standard approach, $\boldsymbol{u}^h$ and ϕ^h are introduced into the weak forms (3.58) and (3.59) and integration is performed over individual finite elements ω of the triangulation $\mathcal{T}$ of the domain Ω,

$$\sum_{\omega\in\mathcal{T}} \int_\omega \boldsymbol{\sigma} : \delta\boldsymbol{\varepsilon}^h \,\mathrm{d}V - \sum_{\partial\omega\in\mathcal{S}_{\boldsymbol{t}}} \int_{\partial\omega} \boldsymbol{t}^* \cdot \delta\boldsymbol{u}^h \,\mathrm{d}S = 0, \quad \forall\,\delta\mathbf{p}_{\boldsymbol{u}}, \tag{3.64}$$

$$\sum_{\omega\in\mathcal{T}} \int_\omega \Big[\Big(\frac{\phi^h - \phi_n^h}{m\tau} + \frac{\partial\psi_{\mathrm{bulk}}}{\partial\phi} + \frac{\partial\psi_{\mathrm{int}}}{\partial\phi}\Big)\delta\phi^h + \frac{\partial\psi_{\mathrm{int}}}{\partial\nabla\phi}\cdot\nabla\delta\phi^h\Big]\mathrm{d}V = 0, \quad \forall\,\delta\mathbf{p}_\phi, \tag{3.65}$$

where $\delta\boldsymbol{\varepsilon}^h = \nabla_{\mathrm{s}}\delta\boldsymbol{u}^h$, and $\mathcal{S}_{\boldsymbol{t}}$ denotes the triangulation of the boundary $\partial\Omega_{\boldsymbol{t}}$ into surface segments $\partial\omega$, consistent with the triangulation $\mathcal{T}$ of the bulk.

The discretized weak forms (3.64) and (3.65) define the set of coupled nonlinear equations that can be written in the following residual form,

$$\mathbf{R}_{\boldsymbol{u}}(\mathbf{p}_{\boldsymbol{u}};\mathbf{p}_\phi) = \mathbf{0}, \qquad \mathbf{R}_\phi(\mathbf{p}_\phi;\mathbf{p}_{\boldsymbol{u}}) = \mathbf{0}. \tag{3.66}$$

At each time step of the incremental procedure, these equations are solved in a monolithic manner, thus $\mathbf{R}(\mathbf{p}) = \mathbf{0}$ with $\mathbf{R} = \{\mathbf{R}_{\boldsymbol{u}}, \mathbf{R}_\phi\}$ and $\mathbf{p} = \{\mathbf{p}_{\boldsymbol{u}}, \mathbf{p}_\phi\}$, using the Newton method.

3.3. Simple laminate*

In view of the fact that laminated microstructures are fundamental to the method which will be introduced in the next chapter, this section presents the theory of simple laminates. The theory is demonstrated under conditions of finite deformations; nevertheless, the transition to the small-strain theory is direct and straightforward, and the equations retain an identical structure, differing only in the adopted measures of strains and stresses.

A simple laminate is a microstructure composed of layers of two phases (materials) separated by parallel planar interfaces, see Fig. 3.5. Under the usual assumption of separation of scales, strains and stresses are homogeneous within each individual layer and are identical in all layers of the same phase. The microstructure is then fully characterized by the volume fractions of the phases, $\eta_1 = 1 - \eta$ and $\eta_2 = \eta$, where $0 \leqslant \eta \leqslant 1$, and by the interface normal $\boldsymbol{N}$, all referred to the reference configuration.

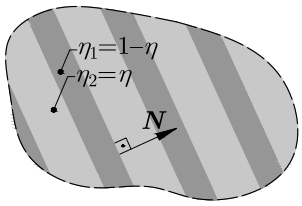

Fig. 3.5. Sketch of a simple laminate. The microstructure is fully characterized by the volume fractions of the phases η_1, η_2 and the lamination orientation, defined by the unit normal vector $\boldsymbol{N}$.

Since the strains and stresses are piecewise homogeneous, the macroscopic deformation gradient $\bar{\boldsymbol{F}} = \{\boldsymbol{F}\}$ and the macroscopic Piola stress $\bar{\boldsymbol{P}} = \{\boldsymbol{P}\}$ are obtained as simple weighted averages of the respective local quantities,

$$\bar{\boldsymbol{F}} = (1-\eta)\boldsymbol{F}_1 + \eta\boldsymbol{F}_2, \qquad \bar{\boldsymbol{P}} = (1-\eta)\boldsymbol{P}_1 + \eta\boldsymbol{P}_2, \tag{3.67}$$

where $\{\square\}$ denotes the average over the representative volume element in the reference configuration. Here, $\boldsymbol{F}_i$ and $\boldsymbol{P}_i$ denote the local quantities within the individual phases.

The compatibility conditions (3.1) and (3.4), and the averaging rules (3.67), complemented by the local constitutive laws of the phases, are sufficient to determine the macroscopic constitutive law relating the macroscopic quantities, $\bar{\boldsymbol{F}}$ and $\bar{\boldsymbol{P}}$. This is illustrated below for the case of hyperelastic constituents. The general case of elastic-plastic phases is discussed in Appendix C, where the corresponding computational scheme is presented including the structure of the nested iterative-subiterative scheme and its linearization.

*The content of this section has been entirely excerpted from the article of Dobrzański *et al.* [35]. Minor modifications may have been applied to the text and figures.

A hyperelastic material model is fully defined by specifying the elastic strain energy function. Denoting by $\psi_i = \psi_i(\boldsymbol{F}_i)$ the Helmholtz free energy density function of phase i, the corresponding Piola stress $\boldsymbol{P}_i$ is obtained as

$$\boldsymbol{P}_i = \frac{\partial \psi_i(\boldsymbol{F}_i)}{\partial \boldsymbol{F}_i}. \tag{3.68}$$

While the requirement of objectivity implies that ψ_i is in fact a function of the right Cauchy–Green tensor $\boldsymbol{C}_i = \boldsymbol{F}_i^{\mathrm{T}}\boldsymbol{F}_i$, it is convenient here to keep the deformation gradient $\boldsymbol{F}_i$ as the argument of ψ_i. Since the constituent phases are hyperelastic, the laminate is also a hyperelastic material. Its behaviour is thus governed by the corresponding (macroscopic) elastic strain energy function that depends on the macroscopic deformation gradient $\bar{\boldsymbol{F}}$, as discussed below.

Using the kinematic compatibility condition (3.1) and the averaging rule $(3.67)_1$, the local deformation gradients $\boldsymbol{F}_i$ can be expressed in terms of the macroscopic deformation gradient $\bar{\boldsymbol{F}}$ and (yet unknown) vector $\boldsymbol{c}$,

$$\boldsymbol{F}_1 = \bar{\boldsymbol{F}} - \eta \boldsymbol{c} \otimes \boldsymbol{N}, \qquad \boldsymbol{F}_2 = \bar{\boldsymbol{F}} + (1-\eta)\boldsymbol{c} \otimes \boldsymbol{N}. \tag{3.69}$$

The macroscopic elastic strain energy $\bar{\psi} = \{\psi\}$ is thus also a function of $\bar{\boldsymbol{F}}$ and $\boldsymbol{c}$,

$$\bar{\psi}(\bar{\boldsymbol{F}}, \boldsymbol{c}) = (1-\eta)\psi_1(\boldsymbol{F}_1) + \eta\psi_2(\boldsymbol{F}_2). \tag{3.70}$$

The unknown vector $\boldsymbol{c}$ can now be determined from the compatibility condition (3.4). The local deformation gradients $\boldsymbol{F}_i$ specified by (3.69) are kinematically admissible since this representation satisfies the kinematic compatibility condition (3.1) and the averaging rule $(3.67)_1$ by construction. Accordingly, the local equilibrium of the laminate, expressed by the compatibility condition (3.4), corresponds to the minimum of the macroscopic elastic strain energy with respect to $\boldsymbol{c}$ (at prescribed $\bar{\boldsymbol{F}}$). Indeed, the condition of stationarity of $\bar{\psi}$ gives

$$\boldsymbol{0} = \frac{\partial \bar{\psi}}{\partial \boldsymbol{c}} = (1-\eta)\frac{\partial \psi_1}{\partial \boldsymbol{F}_1} : \frac{\partial \boldsymbol{F}_1}{\partial \boldsymbol{c}} + \eta \frac{\partial \psi_2}{\partial \boldsymbol{F}_2} : \frac{\partial \boldsymbol{F}_2}{\partial \boldsymbol{c}} = \eta(1-\eta)(\boldsymbol{P}_2 - \boldsymbol{P}_1)\cdot \boldsymbol{N}, \tag{3.71}$$

which is equivalent to (3.4) in the non-trivial case of $0 < \eta < 1$.

Equation (3.4) is a nonlinear equation to be solved for the unknown vector $\boldsymbol{c}$, for instance, using the Newton method. The solution of (3.4) depends (implicitly) on $\bar{\boldsymbol{F}}$, resulting in $\boldsymbol{c} = \boldsymbol{c}(\bar{\boldsymbol{F}})$. The macroscopic elastic strain energy can thus be written as a function of $\bar{\boldsymbol{F}}$ only,

$$\bar{\psi}^*(\bar{\boldsymbol{F}}) = \bar{\psi}(\bar{\boldsymbol{F}}, \boldsymbol{c}(\bar{\boldsymbol{F}})), \tag{3.72}$$

such that $\bar{\psi}^*$ indeed governs the macroscopic response of the laminate,

$$\bar{\boldsymbol{P}} = \frac{\partial \bar{\psi}^*}{\partial \bar{\boldsymbol{F}}}. \tag{3.73}$$

To prove it, one can observe that

$$\begin{aligned}\frac{\partial \bar{\psi}^*}{\partial \bar{\boldsymbol{F}}} &= \frac{\partial \bar{\psi}}{\partial \bar{\boldsymbol{F}}} + \frac{\partial \bar{\psi}}{\partial \boldsymbol{c}} \cdot \frac{\partial \boldsymbol{c}}{\partial \bar{\boldsymbol{F}}} = (1-\eta)\frac{\partial \psi_1}{\partial \boldsymbol{F}_1} : \frac{\partial \boldsymbol{F}_1}{\partial \bar{\boldsymbol{F}}} + \eta \frac{\partial \psi_2}{\partial \boldsymbol{F}_2} : \frac{\partial \boldsymbol{F}_2}{\partial \bar{\boldsymbol{F}}} \\ &= (1-\eta)\boldsymbol{P}_1 + \eta \boldsymbol{P}_2 = \bar{\boldsymbol{P}}, \end{aligned} \tag{3.74}$$

where $\partial \bar{\psi}/\partial \boldsymbol{c} = \boldsymbol{0}$ in view of (3.71). Computation of the tangent moduli tensor is not discussed here since it is discussed in Appendix C in a more general setting.

In the case of linear elastic phases, the laminate is also a linear elastic material fully characterized by a fourth-order tensor of overall elastic moduli. Closed-form formulae for the overall moduli can be found in [145].

4. Formulation of the laminated element technique (LET)

4.1. Idea of the method

The laminated element technique (LET) is a finite-element-based method, in which the spatial discretization does not conform to the internal geometry of the considered body, i.e., the finite-element mesh is not matching the interface. The main idea of LET is rather simple: the finite element that is cut by an interface is treated as a simple laminate composed of the two phases involved, see Fig. 4.1a. No treatment is applied to the elements that fully belong to one phase. Therefore, the partition of the finite-element triangulation $\mathcal{T}$ can be introduced as the union of three disjoint subsets, see Fig. 4.1b,

$$\begin{gathered} \mathcal{T} = \mathcal{T}_1 \cup \mathcal{T}_2 \cup \mathcal{T}_{\text{int}}, \\ \mathcal{T}_1 = \{\omega :\ \eta^{(\omega)} = 0\}, \quad \mathcal{T}_2 = \{\omega :\ \eta^{(\omega)} = 1\}, \quad \mathcal{T}_{\text{int}} = \{\omega :\ 0 < \eta^{(\omega)} < 1\}, \end{gathered} \tag{4.1}$$

where $\eta^{(\omega)}$ is the volume fraction of the phase 2 in the element ω.

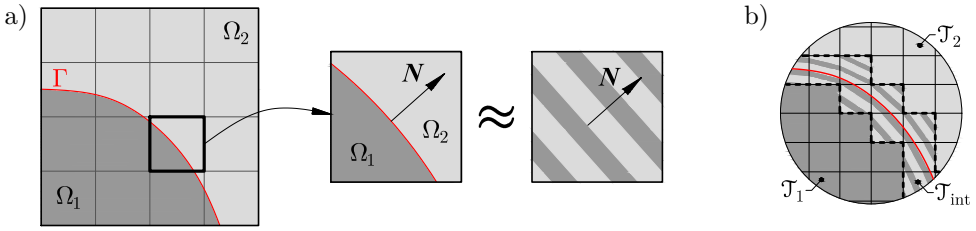

Fig. 4.1. a) Laminated element technique (LET): the element that is cut by an interface (denoted by the red solid line) is treated as a simple laminate with the volume fraction and lamination orientation specified by the actual geometry of the interface within the element. $\boldsymbol{N}$ is the unit normal to the interface; b) partition of the triangulation in LET. The set of all elements that are fully in phase i is denoted by $\mathcal{T}_i$, while $\mathcal{T}_{\text{int}}$ stands for the set of all elements that are cut by the interface.

In each laminated element, the volume fraction of the phases and the lamination orientation are determined according to the actual geometry of the interface within the element, as described in detail in the next section.

4.2. Formulation of the method

As mentioned in Section 3.3, a simple laminate is uniquely defined by two quantities, namely the volume fraction and the unit vector normal to the interfaces separating the phases (in the reference configuration). In LET, these two quantities are determined locally within each laminated element in terms of the level-set function and are assumed constant within each element.

The internal geometry of the considered body is defined by the level-set function ϕ defined over the whole domain Ω,

$$\phi : \ \Omega \subset \mathbb{R}^n \to \mathbb{R}, \tag{4.2}$$

such that $\phi < 0.5$ corresponds to phase 1, $\phi > 0.5$ corresponds to phase 2, and the interface Γ separating the two phases is represented by the $\phi = 0.5$ level set,

$$\Gamma = \{ \boldsymbol{X} \in \Omega \subset \mathbb{R}^n \ | \ \phi(\boldsymbol{X}) = 0.5 \}, \tag{4.3}$$

where $n = 2, 3$ is the space dimension. It is desirable that the level-set function ϕ be smooth and (approximately) proportional to the signed distance from the interface in the nearest neighbourhood of the interface (within the range of one finite element) so that the interface is correctly approximated by the $\phi = 0.5$ level set of the finite-element approximation ϕ^h of the level-set function ϕ,

$$\phi^h = \sum_k N_k^{(\phi)} \phi_k, \tag{4.4}$$

where $N_k^{(\phi)}$ are the usual finite-element basis functions and ϕ_k are the nodal values.

There is some ambiguity concerning the determination of the volume fraction. Exact integration of the volume (or area in 2D) is not possible in the general case and is not needed considering the approximation introduced by LET anyway. In this work, only four-node quadrilateral elements in 2D and eight-node hexahedral elements in 3D are considered, and the following formula for the volume fraction $\eta^{(\omega)} = \eta_2^{(\omega)}$ in the element ω is used,

$$\eta^{(\omega)} = \frac{\displaystyle\sum_{k=1}^{N_\mathrm{n}} \left\langle \phi_k^{(\omega)} - \frac{1}{2} \right\rangle}{\displaystyle\sum_{k=1}^{N_\mathrm{n}} \left| \phi_k^{(\omega)} - \frac{1}{2} \right|}, \tag{4.5}$$

where $\phi_k^{(\omega)}$ are the nodal values of the level-set function ϕ in the element, N_n is the number of nodes in the element, and $\langle \square \rangle = \frac{1}{2}(\square + |\square|)$ denotes the Macaulay brackets.

In 2D, if the considered element is a rectangle and the interface is a straight line cutting two opposite edges of the rectangle, then formula (4.5) gives an exact value of the volume fraction. Likewise, in 3D, formula (4.5) is exact for a planar interface cutting four parallel edges of an element of the shape of a rectangular cuboid. Otherwise, in particular, when the edges are cut differently, formula (4.5) is approximate. For a non-planar interface, the error decreases with mesh refinement since then the interface effectively tends to be more planar. Some efforts have been made to generalize formula (4.5) to improve its accuracy for elements of arbitrary, non-rectangular shape, for instance, by including the usual quadrature weights at the element nodes, but the simple formula (4.5) has been found more accurate. Note that, for a planar interface in 2D, the volume fraction can be computed in closed form using the general formula for the area of a polygon in terms of the coordinates of the vertices. However, this formula does not generalize to the 3D case. The general and simple formula (4.5) is thus adopted in this work, while clearly this part of the model can be replaced by another suitable formulation, see Appendix A.

The unit normal vector $\boldsymbol{N}^{(\omega)}$ is calculated as the normalized gradient of the level-set function ϕ^h at the element centre $\boldsymbol{X}_0^{(\omega)}$,

$$\boldsymbol{N}^{(\omega)} = \frac{\nabla\phi^h(\boldsymbol{X}_0^{(\omega)})}{\|\nabla\phi^h(\boldsymbol{X}_0^{(\omega)})\|}. \tag{4.6}$$

Knowing the volume fraction and the interface normal, the overall constitutive response of the laminate can be readily obtained by applying the micro-to-macro transition, as described in Section 3.3.

Remark 4.1. *The above construction, Eqs.* (4.5) *and* (4.6)*, is applicable when the element is cut by one interface only. The approach can be generalized to the case of more interfaces (and more phases) by introducing additional level-set functions, each corresponding to one interface. A higher-rank laminate can then be considered with the micro-macro transition applied in a hierarchical manner or, if there are only two phases, a simple laminate can be considered with the volume fraction equal to the total volume fraction of the phases within the element and with the lamination orientation obtained by averaging those corresponding to each interface, see Appendix B. The latter approach is employed in the example considered in Section 6.4.*

4.3. Discretized weak form of the equilibrium equation

Considering now the partition of the triangulation (4.1), the discretized weak form of the equilibrium equation for finite-strain framework, introduced in (3.24), in LET takes the form

$$\sum_{i=1}^{2}\left(\sum_{\omega\in\mathcal{T}_i}\int_{\omega}\boldsymbol{P}^h:\operatorname{Grad}\delta\boldsymbol{u}^h\,\mathrm{d}V\right)+\sum_{\omega\in\mathcal{T}_{\mathrm{int}}}\int_{\omega}\bar{\boldsymbol{P}}^h:\operatorname{Grad}\delta\boldsymbol{u}^h\,\mathrm{d}V$$
$$-\sum_{\partial\omega\in\mathcal{S}_{\boldsymbol{t}}}\int_{\partial\omega}\boldsymbol{T}^*\cdot\delta\boldsymbol{u}^h\,\mathrm{d}S=0,\qquad\forall\,\delta\mathbf{p}_{\boldsymbol{u}},\tag{4.7}$$

where $\boldsymbol{P}^h$ denotes the approximated stress in the elements that are fully in the phase i,

$$\boldsymbol{P}^h=\boldsymbol{P}(\boldsymbol{F}^h)=\left.\frac{\partial\psi_i(\boldsymbol{F})}{\partial\boldsymbol{F}}\right|_{\boldsymbol{F}=\boldsymbol{F}^h},\tag{4.8}$$

and $\bar{\boldsymbol{P}}^h$ is the overall (macroscopic) stress in the laminated microstructure in the elements containing the interface,

$$\bar{\boldsymbol{P}}^h=\bar{\boldsymbol{P}}(\boldsymbol{F}^h,\eta^{(\omega)},\boldsymbol{N}^{(\omega)})=\left.\frac{\partial\bar{\psi}(\boldsymbol{F},\eta^{(\omega)},\boldsymbol{N}^{(\omega)})}{\partial\boldsymbol{F}}\right|_{\boldsymbol{F}=\boldsymbol{F}^h}.\tag{4.9}$$

In Eq. (4.8), $\boldsymbol{P}$ is the first Piola–Kirchhoff stress tensor, and ψ_i is the free energy density function for i-th phase, see Eqs. (3.3) and (3.2). In Eq. (4.9), $\bar{\psi}=\bar{\psi}(\boldsymbol{F},\eta^{(\omega)},\boldsymbol{N}^{(\omega)})$ is the overall free energy of the laminate characterized by $\eta^{(\omega)}$ and $\boldsymbol{N}^{(\omega)}$. Recall that $\eta^{(\omega)}$ and $\boldsymbol{N}^{(\omega)}$ depend on the level-set function ϕ^h, see Eqs. (4.5) and (4.6).

The formulation of LET for small deformations is not essentially different from that outlined above. The discretized weak form of the equilibrium equation for such a case is given

$$\sum_{i=1}^{2}\left(\sum_{\omega\in\mathcal{T}_i}\int_{\omega}\boldsymbol{\sigma}^h:\delta\boldsymbol{\varepsilon}^h\,\mathrm{d}V\right)+\sum_{\omega\in\mathcal{T}_{\mathrm{int}}}\int_{\omega}\bar{\boldsymbol{\sigma}}^h:\delta\boldsymbol{\varepsilon}^h\,\mathrm{d}V$$
$$-\sum_{\partial\omega\in\mathcal{S}_{\boldsymbol{t}}}\int_{\partial\omega}\boldsymbol{t}^*\cdot\delta\boldsymbol{u}^h\,\mathrm{d}S=0,\qquad\forall\,\delta\mathbf{p}_{\boldsymbol{u}},\tag{4.10}$$

where the local constitutive equation for elements fully in phase i reads

$$\boldsymbol{\sigma}^h=\boldsymbol{\sigma}(\boldsymbol{\varepsilon}^h)=\left.\frac{\partial\psi_i(\boldsymbol{\varepsilon})}{\partial\boldsymbol{\varepsilon}}\right|_{\boldsymbol{\varepsilon}=\boldsymbol{\varepsilon}^h}=\mathbb{L}_i:(\boldsymbol{\varepsilon}^h-\boldsymbol{\varepsilon}_i^{\mathrm{t}}),\tag{4.11}$$

while for the elements cut by the interface, the equation reads

$$\bar{\boldsymbol{\sigma}}^h=\bar{\boldsymbol{\sigma}}(\boldsymbol{\varepsilon}^h,\eta^{(\omega)},\boldsymbol{n}^{(\omega)})=\left.\frac{\partial\bar{\psi}(\boldsymbol{\varepsilon},\eta^{(\omega)},\boldsymbol{n}^{(\omega)})}{\partial\boldsymbol{\varepsilon}}\right|_{\boldsymbol{\varepsilon}=\boldsymbol{\varepsilon}^h}=\bar{\mathbb{L}}:(\boldsymbol{\varepsilon}^h-\bar{\boldsymbol{\varepsilon}}^{\mathrm{t}}).\tag{4.12}$$

In Eq. (4.11), $\boldsymbol{\sigma}$ is the Cauchy stress tensor, ψ_i is the free energy density function for i-th phase, $\mathbb{L}_i$ is the stiffness tensor for i-th phase, and $\boldsymbol{\varepsilon}_i^{\mathrm{t}}$ is the transformation strain for i-th phase, see Eqs. (3.8)–(3.10). In Eq. (4.12), $\bar{\psi} = \bar{\psi}(\boldsymbol{\varepsilon}, \eta^{(\omega)}, \boldsymbol{n}^{(\omega)})$ is the overall free energy of the laminate characterized by $\eta^{(\omega)}$ and $\boldsymbol{n}^{(\omega)}$, $\bar{\mathbb{L}} = \bar{\mathbb{L}}(\eta^{(\omega)}, \boldsymbol{n}^{(\omega)})$ is the overall stiffness tensor, and $\bar{\boldsymbol{\varepsilon}}^{\mathrm{t}} = \bar{\boldsymbol{\varepsilon}}^{\mathrm{t}}(\eta^{(\omega)}, \boldsymbol{n}^{(\omega)})$ is the overall inelastic (transformation) strain. In this context, the unit normal vector $\boldsymbol{n}^{(\omega)}$ is identical to the one introduced in (4.6), specifically $\boldsymbol{n}^{(\omega)} = \boldsymbol{N}^{(\omega)}$. However, to maintain consistency with prior notation, it is represented using a lowercase letter.

The obtained variational Eqs. (4.7) or (4.10) define the set of equations, in general non-linear, that can be written in the following residual form

$$\mathbf{R}_{\boldsymbol{u}}(\mathbf{p}_{\boldsymbol{u}}) = \mathbf{0}. \tag{4.13}$$

The solution of this system of equations is done by applying the Newton–Raphson method.

Comparing Eqs. (3.24) with (4.7) and (3.27) with (4.10), the novelty of the LET becomes clear. It consists in extracting, during the numerical integration process, the elements cut by the interface. These elements are then subjected to a special treatment involving the homogenization of the laminated microstructures, which allows modelling using nonconforming meshes. The numerical examples demonstrating the performance of LET can be found in Chapter 6.

5. Hybrid diffuse-semisharp treatment of propagating interfaces (LET-PF)

5.1. Idea of the method

The idea of the proposed hybrid diffuse–semisharp approach is to combine the phase-field (PF) method with LET, thus the method will be referred to as LET-PF. Specifically, diffuse interfaces, their propagation and the corresponding microstructure evolution are modelled in a manner similar to the phase-field method. At the same time, the order parameter ϕ plays the role of the level-set function in the LET-based treatment of the mechanical subproblem. As noted in the introduction of Subsection 3.2.1, the considerations of moving interfaces are limited to the scope of the small-strain framework only. Consequently, the LET-PF formulation presented in this chapter does not encompass scenarios involving finite deformations.

5.2. Discretized weak forms of the equilibrium and evolution equations

As discussed in Subsection 3.2.3, the weak formulation of the discretized conventional phase-field method is specified by Eqs. (3.64) and (3.65). In LET-PF, the virtual work principle (3.64) is replaced by that of the LET method,

$$\sum_{i=1}^{2}\left(\sum_{\omega\in\mathcal{T}_i}\int_{\omega}\boldsymbol{\sigma}^h:\delta\boldsymbol{\varepsilon}^h\,\mathrm{d}V\right)+\sum_{\omega\in\mathcal{T}_{\mathrm{int}}}\int_{\omega}\bar{\boldsymbol{\sigma}}^h:\delta\boldsymbol{\varepsilon}^h\,\mathrm{d}V - \sum_{\partial\omega\in\mathcal{S}_{\boldsymbol{t}}}\int_{\partial\omega}\boldsymbol{t}^*\cdot\delta\boldsymbol{u}^h\,\mathrm{d}S=0,\qquad\forall\,\delta\mathbf{p}_{\boldsymbol{u}},\tag{5.1}$$

which here refers to the current time instant $t = t_{n+1}$ with the microstructure specified by the order parameter field ϕ^h at the current time t_{n+1}. The time-discrete evolution of the order parameter ϕ^h is governed by the following weak form,

$$\sum_{\omega\in\mathcal{T}} \int_{\omega} \left[\left(\frac{\phi^h - \phi^h_n}{m\tau} + \frac{\partial \psi_{\mathrm{int}}}{\partial \phi} \right) \delta\phi^h + \frac{\partial \psi_{\mathrm{int}}}{\partial \nabla \phi} \cdot \nabla \delta\phi^h \right] \mathrm{d}V$$

$$+ \sum_{\omega\in\mathcal{T}_{\mathrm{int}}} \int_{\omega} \sum_{i=1}^{N_{\mathrm{n}}} \frac{\partial \bar{\psi}_{\mathrm{bulk}}}{\partial \phi_i^{(\omega)}} \, \delta\phi_i^{(\omega)} \mathrm{d}V = 0, \qquad \forall\, \delta\mathbf{p}_\phi, \tag{5.2}$$

which replaces the weak form (3.65) of the conventional phase-field model. The first term in Eq. (5.2) includes the interfacial energy contribution and the viscous evolution term and is identical to the respective part of the weak form (3.65). The second term in Eq. (5.2) describes the driving force resulting from the bulk energy $\bar{\psi}_{\mathrm{bulk}}$ of the laminated elements along the interface. This term is the counterpart of the respective term in the LET form of the virtual work principle, see Eqs. (4.10) and (4.12). Note that, in LET-PF, the bulk energy depends on the order parameter field ϕ^h only in the laminated elements $\omega \in \mathcal{T}_{\mathrm{int}}$ (through $\eta^{(\omega)}$ and $\boldsymbol{n}^{(\omega)}$). Actually, also the set $\mathcal{T}_{\mathrm{int}}$ itself depends on ϕ^h (likewise, $\mathcal{T}_1$ and $\mathcal{T}_2$) and may change during a time step and even between the individual iterations of the global Newton scheme. Accordingly, to improve the convergence behaviour, a regularization of the formula for $\eta^{(\omega)}$ in Eq. (4.5) is employed, as discussed in the next section.

5.3. Discussion

Summarizing, the difference with respect to the conventional phase-field method is that, in LET-PF, the two sub-models are coupled only within the laminated interface elements in $\mathcal{T}_{\mathrm{int}}$. This is, in particular, apparent in Eq. (4.10), where $\bar{\boldsymbol{\sigma}}$ is the only term that depends on ϕ^h, in addition to the set $\mathcal{T}_{\mathrm{int}}$ itself. Likewise, in Eq. (5.2), the coupling occurs only through the overall bulk energy $\bar{\psi}_{\mathrm{bulk}}$ of the laminates that is defined only within the laminated interface elements in $\mathcal{T}_{\mathrm{int}}$. At the same time, in the conventional phase-field method, the coupling occurs within the whole volume of the diffuse interfaces, i.e., whenever $0 < \phi < 1$.

And for this reason, the LET-PF has been described as the *hybrid diffuse-semisharp* approach. While the interfacial energy ψ_{int} remains diffuse and the effective thickness of the transition region between two phases can be roughly estimated by 4ℓ, as in the conventional phase-field model, in the case of the bulk energy, LET-PF smears it out within the layer of only one-element thickness. This is also the reason why the bulk part of LET-PF is called "semisharp" rather than "sharp" – after all, the interface is still smeared out, albeit to a smaller degree. Together with the minimum resolution constraint, $h \leqslant \ell/2$ [58], it makes the interface at least eight times "sharper" than in the case of the conventional phase-field method, see Fig. 5.1. It also means that for problems with the dominant

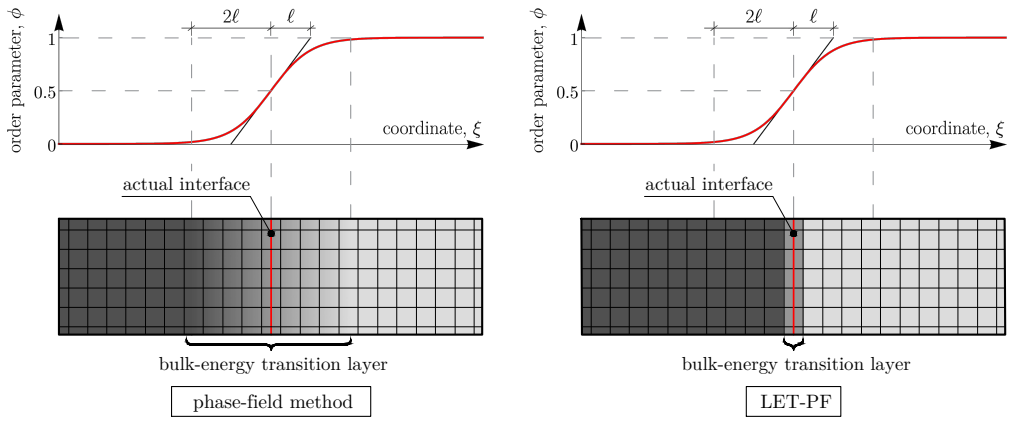

Fig. 5.1. LET-PF compared to the conventional phase-field method. The profile of the order parameter is sketched in the upper figures. The shading of the mesh in the bottom figures indicates the volume fraction of the phases that governs the bulk energy. In the conventional phase-field method, the transition layer is diffuse and spans several elements (left), while in the semisharp LET-PF method, it is localized to only one layer of elements (right).

contribution of the bulk-energy-related driving force, LET-PF should give more accurate overall results even for coarse meshes, which will be demonstrated in Chapter 7. However, when using LET-PF, the mesh size h should still not be too large compared to the thickness parameter ℓ – as mentioned in Section 4.2, it is desirable for the level-set function (here: the order parameter ϕ) to be smooth and approximately proportional to the signed distance from the interface within the range of one element.

Finally, it is worth noting that if the driving force related to the total interfacial energy dominates that caused by the total bulk energy, the interface propagation is effectively governed by the same evolution equation regardless of the method used, whether LET-PF or conventional phase-field. This observation comes from that in Eqs. (3.65) and (5.2), the term associated with the bulk energy becomes negligibly small and can be neglected. Consequently, these equations become identical, rendering both methods indistinguishable in this particular aspect. This effect will be exhibited later in Chapter 7.

Note that the mixing based on laminated microstructures, thus in a sense similar to LET-PF, is employed in some formulations of the phase-field method [8,38,106,132], however, consistent with the phase-field framework, it is applied within the entire diffuse interface.

The proposed approach bears some similarity to the level-set method [115] combined with X-FEM [108,109,146]. That approach appears attractive because X-FEM is a sharp-interface technique so that the interfaces can be modelled with a high accuracy using a non-matching mesh. However, compared to the

phase-field method, the related applications for microstructure evolution problems are much more scarce, e.g. [37,62,111]. The LET approach used in LET-PF is not as accurate as X-FEM [35], but it is much simpler, in particular, its implementation is carried out solely at the element level and does not require intervention into the structure of the finite-element code. Another pronounced difference between the two approaches is in the way the interfacial energy is treated. The level-set function in the level-set method is a signed distance function and its role is only to (implicitly) define the position of the sharp interface. The interfacial energy (density per unit area) is then assigned directly to the sharp interface. In LET-PF, a diffuse-interface description of the interfacial energy is adopted as in the conventional phase-field method so that the interfacial energy contribution to the total energy is a bulk-like energy (density per unit volume) distributed in the vicinity of the interfaces.

5.4. Regularized volume fraction formula

As mentioned in the previous section, the LET-PF method uses a regularization of the volume fraction formula for $\eta^{(\omega)}$, given in Eq. (4.5). As is well known, the absolute value function $|\square|$, which is the essential part of this formula, is a function that is non-smooth at zero, so its first derivative suffers a jump at this point. For this reason, its use in the LET-PF method may be a source of convergence stability problems. Therefore, the modified absolute value function is proposed to overcome this problem. The new function, defined as

$$|\phi|_{\mathrm{reg}} = \begin{cases} |\phi|, & |\phi| \geqslant \phi_{\mathrm{reg}}, \\ \dfrac{1}{2\phi_{\mathrm{reg}}}(\phi^2 + \phi_{\mathrm{reg}}^2), & |\phi| < \phi_{\mathrm{reg}}, \end{cases} \tag{5.3}$$

at the point of the aforementioned discontinuity is smoothed by a parabola connecting the two branches of the absolute value function, i.e., $-\phi$ and ϕ, as shown in Fig. 5.2a. The function $|\phi|_{\mathrm{reg}}$ depends on the regularization parameter ϕ_{reg}, which describes how large the span of the parabola is, but also how large the curvature is at the point $(0, |0|_{\mathrm{reg}})$, being inversely proportional to the regularization parameter. Hence, one can conclude that when the regularization parameter tends to zero, $\phi_{\mathrm{reg}} \to 0$, the curvature tends to infinity, and thus the function (5.3) becomes an absolute value function, i.e., $|\phi|_{\mathrm{reg}} \to |\phi|$.

As a result of the modified absolute value function (5.3), the Macaulay brackets function, used in Eq. (4.5), will also be modified, namely

$$\langle\phi\rangle_{\mathrm{reg}} = \frac{1}{2}\left(\phi + |\phi|_{\mathrm{reg}}\right), \tag{5.4}$$

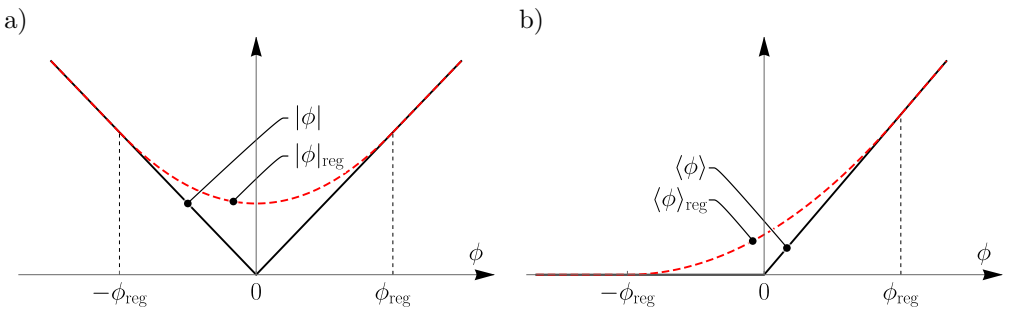

Fig. 5.2. Regularized (a) absolute value and (b) Macaulay brackets functions.

whose visualization is shown in Fig. 5.2b. Finally, the elemental volume fraction will be calculated from the formula

$$\eta^{(\omega)} = \frac{\displaystyle\sum_{k=1}^{N_{\mathrm{n}}} \left\langle \phi_k^{(\omega)} - \frac{1}{2} \right\rangle_{\mathrm{reg}}}{\displaystyle\sum_{k=1}^{N_{\mathrm{n}}} \left| \phi_k^{(\omega)} - \frac{1}{2} \right|_{\mathrm{reg}}}. \tag{5.5}$$

The consequence of applying this formula will be that, as the interface approaches some fixed distance, depending on the regularization parameter ϕ_{reg}, to the node(s) of the cut element, the value of the volume fraction in the adjacent element, calculated according to the formula (5.5), will be in the interval $0 < \eta^{(\omega)} < 1$. This means that such a neighbouring element, despite the absence of the interface within it, will be classified in the set of interface elements $\mathcal{T}_{\mathrm{int}}$, where the lamination treatment is applied. Let this effect be called "an activation" of a neighbouring element. It is shown in Fig. 5.3, which presents an example of the sequence of successive stages of interface evolution.

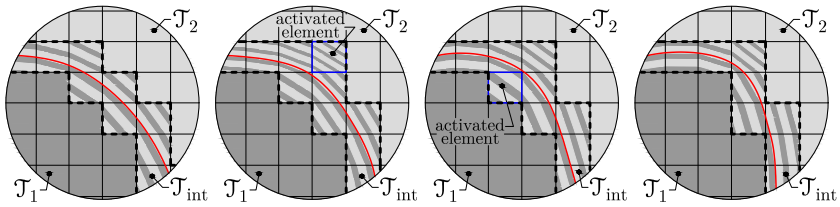

Fig. 5.3. Exemplary sequence of the interface evolution showing the effect of neighbouring element activation.

It therefore remains to determine what value the regularization parameter ϕ_{reg} should be. It was mentioned earlier that it is related to the span of the

parabola smoothing the absolute value function. It cannot therefore be too large, so that the effect of activation of neighbouring elements does not occur too early, i.e., when the distance of the interface to the node(s) is, with respect to the mesh size h, relatively large. It would therefore be necessary to relate the value of the regularization parameter ϕ_{reg} to the size of the finite element h. Furthermore, it is worth noting that its span will also depend on the slope of the function ϕ within the interface, and hence on the assumed interface thickness parameter ℓ. Therefore, the value of the regularization parameter can be roughly estimated according to the formula

$$\phi_{\mathrm{reg}} \approx \frac{h}{2\ell} d, \tag{5.6}$$

where $d > 0$ denotes the relative distance from the node(s), related to the mesh size h, within which the appearance of the interface activates a neighbouring element fully in one of the phases.

The above regularization significantly improves the convergence behaviour. The analysis can proceed with a larger time step, while it has a small effect on the results. In Appendix D, the illustration of this effect is shown based on the additional simulations of the problem studied in Section 7.1.

6. Numerical experiments – material interfaces*

The performance of LET is examined in this chapter through several numerical examples. In all examples, a regular quadrilateral (2D) or hexahedral (3D) mesh is used. In all cases, the results are compared to those obtained using two simple non-conforming mesh approaches that will be referred to as ELA (element-level assignment) and GPLA (Gauss-point-level assignment), see Fig. 6.1. Whenever applicable a conforming mesh is also used.

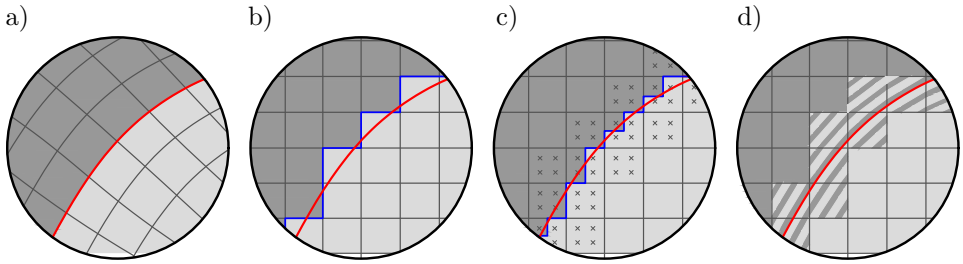

Fig. 6.1. Discretization approaches employed in this work: a) conforming mesh, b) element-level assignment (ELA), c) Gauss-point-level assignment (GPLA), and d) laminated element technique (LET). In ELA (resp. GPLA), the whole element (resp. Gauss point) belongs to a single phase that is determined by the value of the level-set function in the element centre (resp. at the Gauss point).

As illustrated in Fig. 6.1b, in ELA, the whole element is assigned to one of the phases, and this approach, sometimes called digital-image-based FEM or voxel-based FEM, is commonly used for segmented 2D and 3D images of the microstructure or for rasterized representation of the microstructure, e.g. [70, 93, 151]. In GPLA, Fig. 6.1c, individual integration (Gauss) points are assigned to one of the phases according to the position of the integration point, possibly combined with an increased number of integration points, e.g. [42, 109]. In the context of voids and free boundaries, this latter approach is closely related to the finite cell method [116].

*The content of this chapter has been entirely excerpted from the article of Dobrzański *et al.* [35]. Minor modifications may have been applied to the text and figures.

6.1. Elastic inclusion

In this section, a 2D elastic inclusion problem in the small-strain framework is considered. The problem is adopted from [109,146]. Figure 6.2a shows a body that consists of two domains, Ω_1 (inclusion) and Ω_2, with the elastic constants (E_1, ν_1) and (E_2, ν_2) that are constant within each domain and suffer discontinuity at the (bonded) interface Γ. The radius of the inclusion and the outer radius are denoted by a and b, respectively. The loading is applied by prescribing the radial displacement $u_r = u_r^*$ and zero circumferential displacement $u_\theta = 0$ at the outer boundary Λ. This problem admits an analytical solution that can be found in [146].

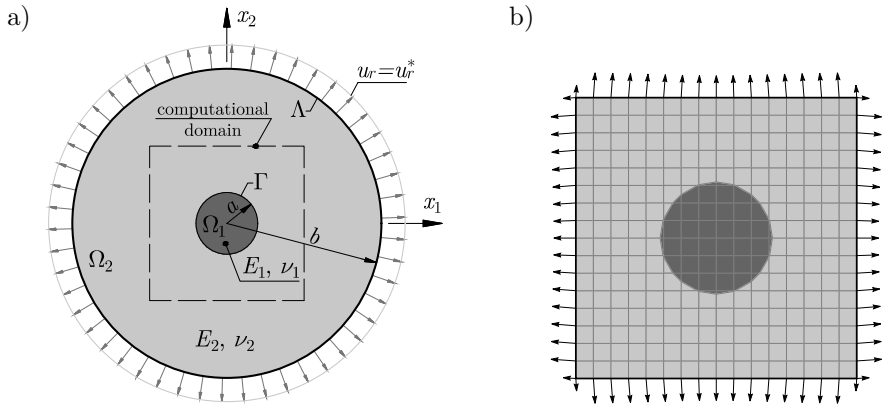

Fig. 6.2. Elastic inclusion problem: a) scheme of the problem; b) computational domain with a regular (non-conforming) mesh of quadrilateral elements (16×16 elements, $h = 0.125$). The interface Γ is approximated by the $\phi^h = 0.5$ level set. The arrows in panel (b) represent the nodal forces applied to the boundary nodes, which are calculated from the traction resulting from the analytical solution.

In the computational model, a square-shaped domain with the inclusion in the centre is considered, which is discretized into a regular mesh of isoparametric four-node elements. The dimensions of the computational domain are $L \times L$, where $L = 2$, while the parameters specifying the reference problem are adopted as $a = 0.4$ and $b = 2$. To ensure equivalence with the model described above, the traction resulting from the analytical solution is applied on the boundary of the computational domain. Additionally, appropriate displacement boundary conditions are imposed to prevent rigid-body motion.

To examine the performance of LET, the problem is solved for several mesh densities with the element size h varying between $h = 1$ (very coarse mesh with 2×2 elements) and $h \approx 0.001$. The elastic constants are adopted as $E_1 = 1$,

$\nu_1 = 0.25$, $E_2 = 10$, and $\nu_2 = 0.3$ ("soft inclusion" case) and as $E_1 = 200$, $\nu_1 = 0.25$, $E_2 = 1$, and $\nu_2 = 0.3$ ("hard inclusion" case). Convergence of the error is shown in Fig. 6.3. The error is here defined as the relative error in energy norm, as in [42, 109],

$$\bar{e}_E = \frac{1}{\left(\int\limits_\Omega 2\psi^{\mathrm{el}}(\boldsymbol{\varepsilon}^{\mathrm{exact}})\,\mathrm{d}\Omega \right)^{1/2}} \left\| \boldsymbol{u}^h - \boldsymbol{u}^{\mathrm{exact}} \right\|_{E(\Omega)} = \left(\frac{\int\limits_\Omega \psi^{\mathrm{el}}(\boldsymbol{\varepsilon}^h - \boldsymbol{\varepsilon}^{\mathrm{exact}})\,\mathrm{d}\Omega}{\int\limits_\Omega \psi^{\mathrm{el}}(\boldsymbol{\varepsilon}^{\mathrm{exact}})\,\mathrm{d}\Omega} \right)^{1/2}, \tag{6.1}$$

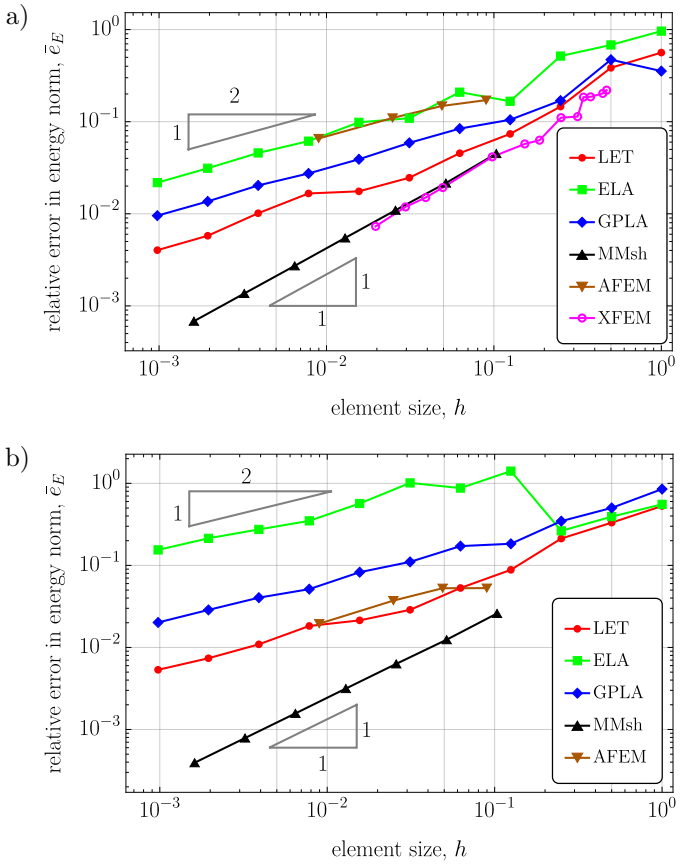

Fig. 6.3. Elastic inclusion problem: rate of convergence in energy norm for: a) soft inclusion ($E_2/E_1 = 10$) and b) hard inclusion ($E_2/E_1 = 0.005$). The results obtained for a matching mesh of four-node quadrilateral elements are labelled "MMsh". The results for X-FEM are taken from [109], and those for A-FEM from [42].

where ψ^{el} is the elastic strain energy density function, $\boldsymbol{u}^{\text{exact}}$ and $\boldsymbol{\varepsilon}^{\text{exact}}$ are the exact displacement and strain obtained from the analytical solution, and $\boldsymbol{u}^h$ and $\boldsymbol{\varepsilon}^h$ are the displacement and strain resulting from the computational model. The integrals are evaluated by applying the 2×2 Gauss quadrature. Note that, in the case of LET, the local strains in each phase are known at the Gauss points of the laminated elements, and the respective local strains are used to evaluate the error.

Figure 6.3 shows the results obtained for LET, and for comparison, for ELA and GPLA, the two simple non-conforming mesh approaches that will be used as a reference in all subsequent examples. Figure 6.3 includes also the results obtained for a matching mesh as well as the results taken from the literature for exactly the same problem, specifically, for X-FEM [109] (available only for the soft inclusion case) and for A-FEM [42]. It follows from Fig. 6.3 that the convergence rate of LET, ELA, GPLA, and A-FEM is similar, approximately equal to 0.5, but the error is the lowest for LET (in the hard inclusion case, the error of LET and A-FEM is similar). Since these methods employ a non-conforming approximation of the displacement field, the optimal convergence rate of 1, characteristic for a matching mesh and also for X-FEM, cannot be achieved. This is also illustrated in Fig. 6.4 where the error in L_2 norm ($e_{L_2} = \|\boldsymbol{u}^h - \boldsymbol{u}^{\text{exact}}\|_{L_2(\Omega)}$) is shown. In this norm, the convergence rate is approximately equal to 1 for LET, ELA and GPLA, while it is equal to 2 for a matching mesh, as expected. It is stressed here that LET is not aimed to compete with more sophisticated methods, like X-FEM, in terms of accuracy. The advantage of LET is its simplicity and ease of implementation, and, at the same time, improved accuracy, as compared to ELA and GPLA.

Figure 6.5 shows the relative error in energy norm as a function of Young's moduli contrast E_2/E_1 evaluated for $E_1 = 1$ and $\nu_1 = \nu_2 = 0.25$, and for the element size $h = 0.004$ (500×500 elements). Again, the error is the lowest for LET, and the difference with respect to ELA and GPLA increases with increasing contrast, particularly in the case of hard inclusion ($E_2/E_1 < 1$).

The results reported so far concern the overall error. However, in some situations, the local error can also be important, for instance, the artificial stress concentrations resulting from the non-conforming representation of interfaces. To illustrate the respective performance of LET, ELA and GPLA, Fig. 6.6 presents the difference between the exact local stresses and those predicted by the three methods for the soft-inclusion problem and for a representative mesh density (128×128 elements). Specifically, the equivalent (von Mises) stress σ_{eq} is considered and the difference is normalized by the maximum stress in the analytical solution, $\sigma^{\text{exact}}_{\text{eq,max}}$. Note that the colour scale in Fig. 6.6 corresponds to the range of values between 0 and 0.01, while the respective maximum values are significantly higher and are provided below each figure. In LET, in the laminated elements, the local stresses in each phase are considered (marked as "micro") as well as the

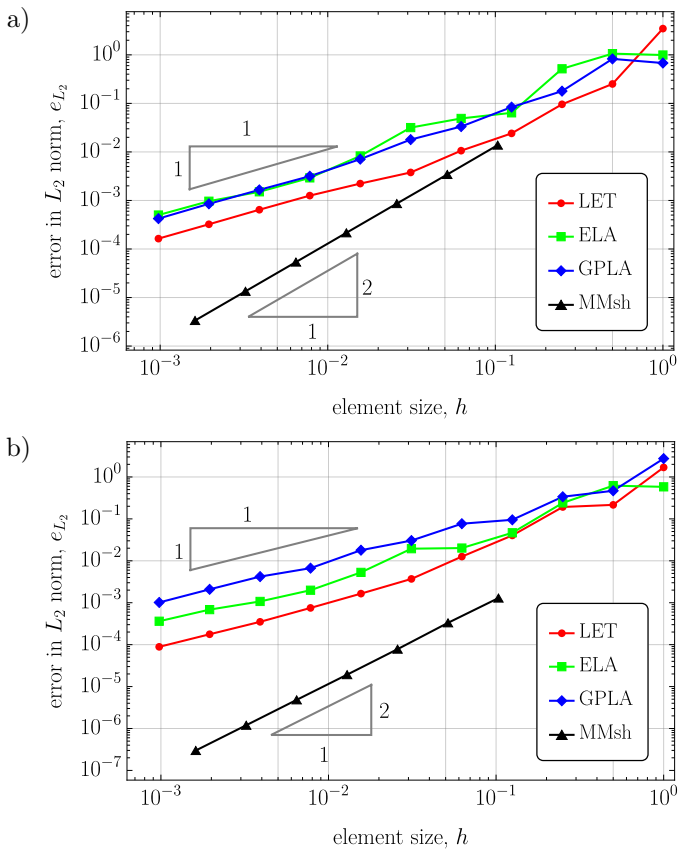

Fig. 6.4. Elastic inclusion problem: rate of convergence in L_2 norm for: a) soft inclusion ($E_2/E_1 = 10$) and b) hard inclusion ($E_2/E_1 = 0.005$).

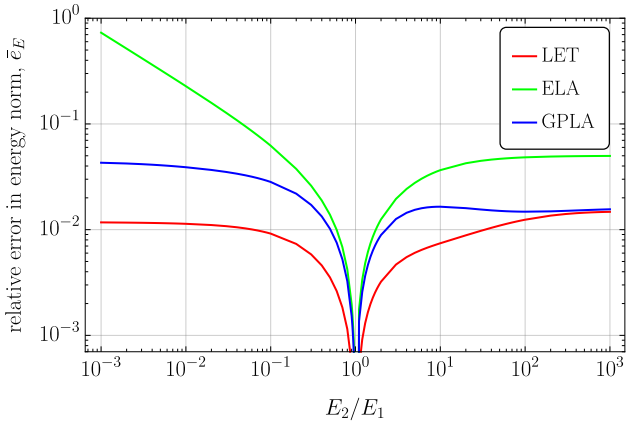

Fig. 6.5. Elastic inclusion problem: relative error in energy norm as a function of Young's moduli contrast E_2/E_1.

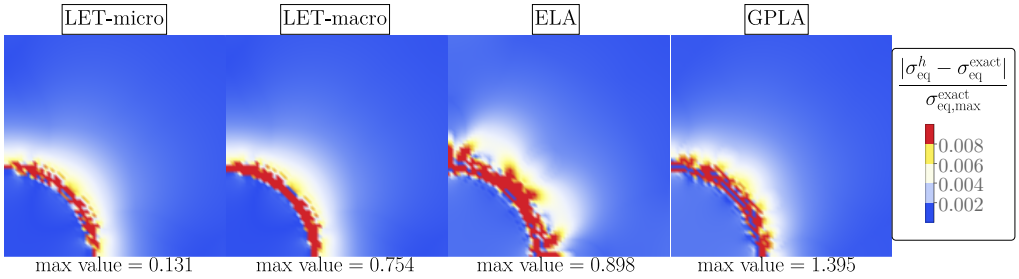

Fig. 6.6. Elastic inclusion problem: the difference between the exact local equivalent stress and those predicted by LET, ELA and GPLA normalized by the maximum stress $\sigma^{\rm exact}_{\rm eq,max}$ (soft inclusion, 128×128 elements, one quarter of the domain is shown).

overall stress of the laminate (marked as "macro"). It follows that LET performs much better than ELA and GPLA in representing the local stresses in each phase (the maximum difference is 0.131 in the case of LET-micro as compared to 0.898 for ELA and 1.395 for GPLA). In the case of the overall stress in LET, the maximum difference (0.754 for LET-macro) is only slightly smaller than in the case of ELA and GPLA.

6.2. Compatible eigenstrain at a planar interface

In this section, the behaviour of LET for a 2D problem of elasticity with eigenstrain in the small-strain framework is investigated. Two elastic domains are separated by a planar interface inclined at an angle α to the horizontal axis, see Fig. 6.7a. Each domain is homogeneous and is characterized by elastic constants E_i and ν_i and by a homogeneous eigenstrain $\boldsymbol{\varepsilon}^0_i$ so that the elastic strain energy is a function of the elastic strain, $\psi^{\rm el}_i = \psi^{\rm el}_i(\boldsymbol{\varepsilon}^{\rm el})$, $\boldsymbol{\varepsilon}^{\rm el} = \boldsymbol{\varepsilon} - \boldsymbol{\varepsilon}^0_i$.

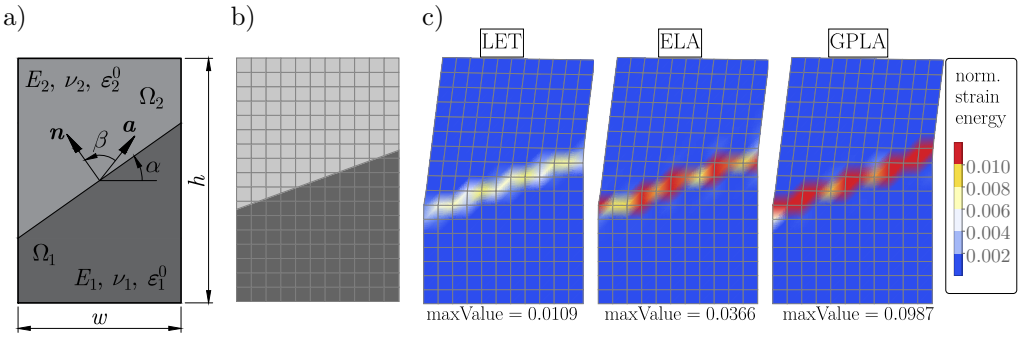

Fig. 6.7. Eigenstrain problem: a) scheme of the problem; b) computational domain with a coarse (non-conforming) mesh of 11×17 quadrilateral elements for a sample interface orientation $\alpha = \pi/9$ (the actual computations are carried out for a fine mesh of 101×151 elements); c) deformed coarse mesh with the colour map of the normalized elastic strain energy density, $\psi^{\rm el}/(a^2 E^*)$, for $\beta = \pi/2$ (displacements are scaled for better visibility).

The eigenstrains in both phases are assumed compatible so that

$$\Delta\boldsymbol{\varepsilon} = \boldsymbol{\varepsilon}_2^0 - \boldsymbol{\varepsilon}_1^0 = \frac{1}{2}\,(\boldsymbol{a}\otimes\boldsymbol{n} + \boldsymbol{n}\otimes\boldsymbol{a}), \tag{6.2}$$

where $\boldsymbol{n}$ is a unit normal to the interface, $\boldsymbol{a}$ is a prescribed vector, and to fix attention that $\boldsymbol{\varepsilon}_1^0 = \boldsymbol{0}$ is assumed. Accordingly, in the continuum setting, the total elastic strain energy vanishes,

$$\int_\Omega \psi^{\mathrm{el}}\left(\boldsymbol{\varepsilon} - \boldsymbol{\varepsilon}^0\right)\mathrm{d}\Omega = 0. \tag{6.3}$$

For a non-conforming finite-element mesh, the local incompatibilities introduced by the discretization are accommodated by elastic strains which are localized along the interface and vanish far from the interface in view of the overall compatibility of the eigenstrains, cf. Eq. (6.2). This is illustrated in Fig. 6.7c which shows the normalized elastic strain energy density, $\psi^{\mathrm{el}}/(a^2E^*)$, for a representative case of $\alpha = \pi/9$ and $\beta = \pi/2$ (a coarse mesh is used for illustration purposes). It can be seen that the elastic strain energy is visibly lower in case of LET than in case of ELA nad GPLA.

The corresponding total strain energy can be used as a measure of the error. The normalized error in energy norm is thus defined as

$$\tilde{e}_E = \frac{1}{(a^2E^*L)^{1/2}}\left\|\boldsymbol{u}^h - \boldsymbol{u}^{\mathrm{exact}}\right\|_{E(\Omega)} = \left(\frac{1}{a^2E^*L}\int_\Omega \psi^{\mathrm{el}}(\boldsymbol{\varepsilon}^h - \boldsymbol{\varepsilon}^0)\,\mathrm{d}\Omega\right)^{1/2}, \tag{6.4}$$

where the error is normalized by the interface length L and also by $a = \|\boldsymbol{a}\|$ and $E^* = \sqrt{E_1E_2}$ so that the error does not depend on a and depends on E_1 and E_2 only through their ratio, the contrast E_2/E_1.

The analysis is performed for a wide range of Young's moduli contrasts $E_2/E_1 \in (0.001, 1000)$ with $\nu_1 = \nu_2 = 0.25$ and for two values of the angle β between vectors $\boldsymbol{a}$ and $\boldsymbol{n}$, namely $\beta = 0$ and $\beta = \pi/2$. The actual computations are carried out for $E_1E_2 = 1$ and $a = 1$. Dimensions of the rectangular domain are $w = 10$ and $h = 15$, and the domain is discretized into a regular mesh of 101×151 elements (element size $h \approx 0.1$). An odd number of elements is adopted in each direction and the interface passes through the centre of the domain so that, for all orientation angles, the mesh is non-conforming (also for $\alpha = 0$ and $\pi/2$). The boundaries are free, only the rigid body motion is prevented by enforcing adequate boundary conditions.

Representative results are shown in Fig. 6.8 for $\beta = 0$ and in Fig. 6.9 for $\beta = \pi/2$. Intermediate values of β are not considered since the corresponding solutions can be obtained by the superposition of those for $\beta = 0$ and $\beta = \pi/2$

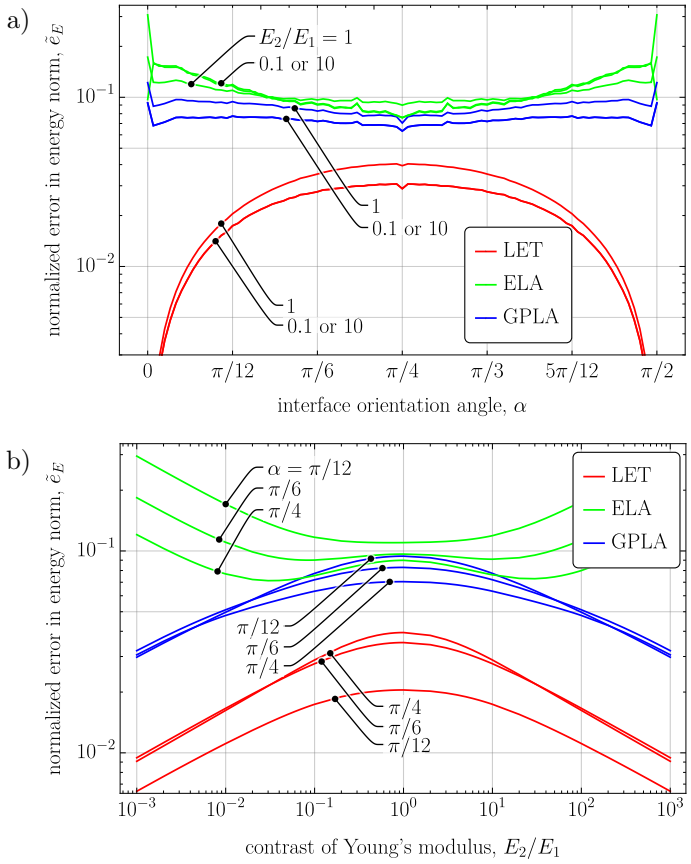

Fig. 6.8. Normalized error in energy norm for $\beta = 0$ as a function of: a) the interface orientation angle α and b) Young's moduli contrast E_2/E_1. (Due to an error found, this graphic has been corrected and differs from the one published in Dobrzański *et al.* [35].

(even if the error, as a nonlinear function of the solution, cannot be obtained by superposition).

Figures 6.8a and 6.9a show the dependence of the error on the interface orientation angle α. As expected, the individual diagrams exhibit symmetry with respect to $\alpha = \pi/4$. Likewise, the diagrams in Figs. 6.8b and 6.9b, which depict the dependence on the contrast E_2/E_1 exhibit symmetry with respect to $E_2/E_1 = 1$ (recall that $\nu_1 = \nu_2$ and $E_1 E_2 = 1$). It is also seen that, for LET, the error vanishes for $\alpha = 0$ and $\pi/2$, i.e., when the interface is parallel to element edges.

Figures 6.8 and 6.9 show that in most cases the error is the lowest for LET. However, for $\beta = \pi/2$, when the eigenstrain jump is a shear strain, LET performs better than GPLA only for moderate contrasts, see Fig. 6.9b.

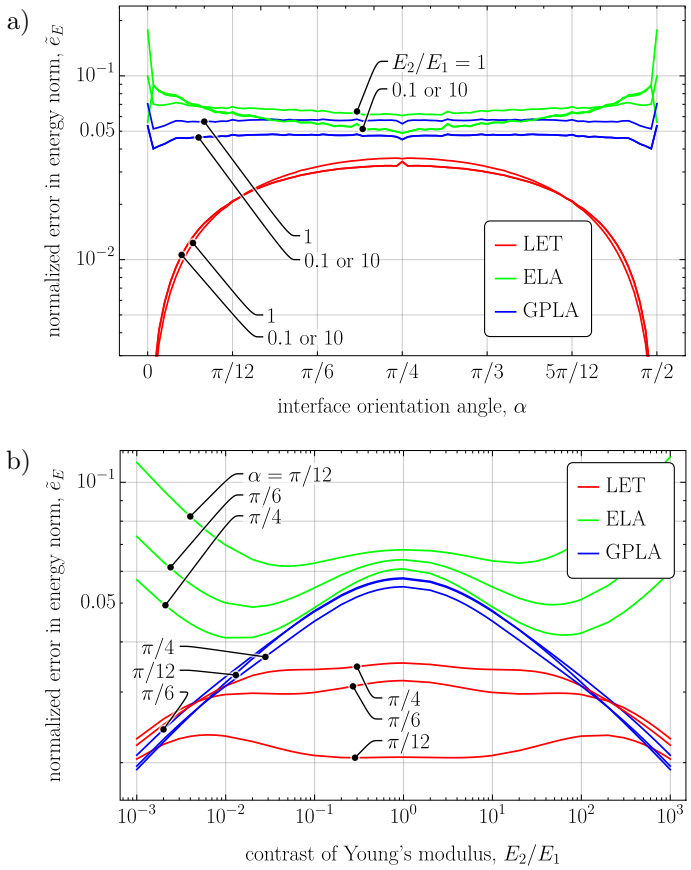

Fig. 6.9. Normalized error in energy norm for $\beta = \pi/2$ as a function of: a) the interface orientation angle α and b) Young's moduli contrast E_2/E_1. (Due to an error found, this graphic has been corrected and differs from the one published in Dobrzański *et al.* [35].)

6.3. Elastic inclusion with varying radius

One of the advantages of LET over ELA and GPLA is its ability to adapt to continuous changes in the position of the interface within a single finite element. In LET, if the position of the interface is varied in a continuous manner, the volume fractions of the phases and the orientation of the interface also change in a continuous manner, whereas in ELA and GPLA these changes are taken into account in a step-wise manner (volume fraction) or not at all (orientation of the interface). This effect is illustrated here by considering a 3D cubic cell of dimension L with a central inclusion of varying diameter D.

Both phases are linear elastic with the properties specified as $E_1 = 10$, $\nu_1 = 0.3$ (inclusion) and $E_2 = 1$, $\nu_2 = 0.2$ (matrix). The inclusion diameter

is varied between $D/L = 0.6$ and $D/L = 0.9$, and a regular mesh of $20 \times 20 \times 20$ elements is used, see Fig. 6.10. Periodic boundary conditions are enforced and the overall elastic moduli tensor is determined in a standard manner by subjecting the unit cell to 6 linearly independent macroscopic strains (actually 3 are sufficient due to symmetry). The overall elastic moduli tensor is then determined in terms of the resulting overall stress tensors. Below, the results are reported in terms of the directional Young's modulus $E_{100} = (S_{1111})^{-1}$, where S_{ijkl} denotes the components of the elastic compliance tensor.

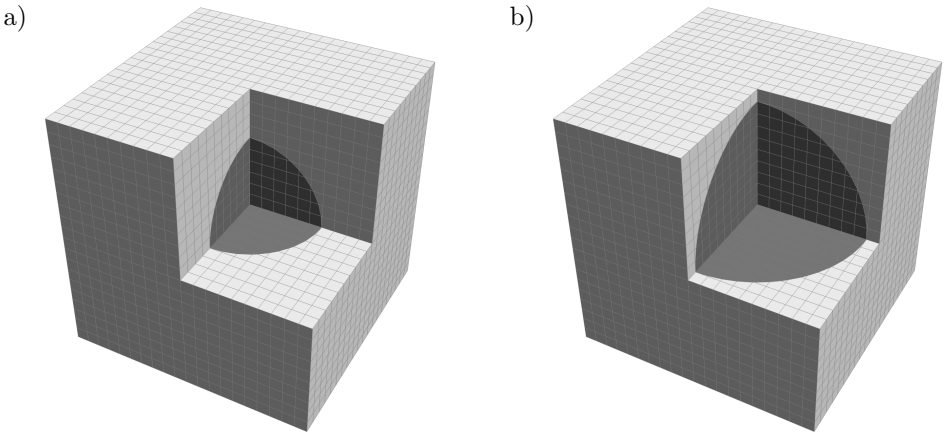

Fig. 6.10. Periodic unit cell with a spherical elastic inclusion of the diameter that varies between $D/L = 0.6$ (a) and $D/L = 0.9$ (b). A fixed regular finite-element mesh ($20 \times 20 \times 20$ elements) is used.

Figure 6.11a shows the dependence of E_{100} on the inclusion diameter. The mesh is here rather coarse, hence the predictions of the three methods (LET, ELA, GPLA) differ visibly. However, the important difference is that the dependence is smooth in the case of LET, while in the case of ELA and GPLA the overall properties change in a step-wise manner, see the inset in Fig. 6.11a. Here, the overall moduli (e.g., E_{100}) exhibit a jump whenever the element (for ELA) or Gauss point (for GPLA) is assigned to a different phase when the interface position is changed. Clearly, LET is free of such artefacts, and the overall moduli depend on the inclusion diameter in a continuous fashion.

For completeness, the derivative of the dependence of E_{100} on D, as predicted by LET, is shown Fig. 6.11b. The derivative is here computed using the finite difference scheme in terms of two subsequent data points. The small irregularities that can be seen in Fig. 6.11b result from the error introduced by LET. It follows that the response is continuous and its derivative is meaningful, which suggests that LET can be considered as a candidate for treating moving interface problems, such as microstructure evolution or shape optimization.

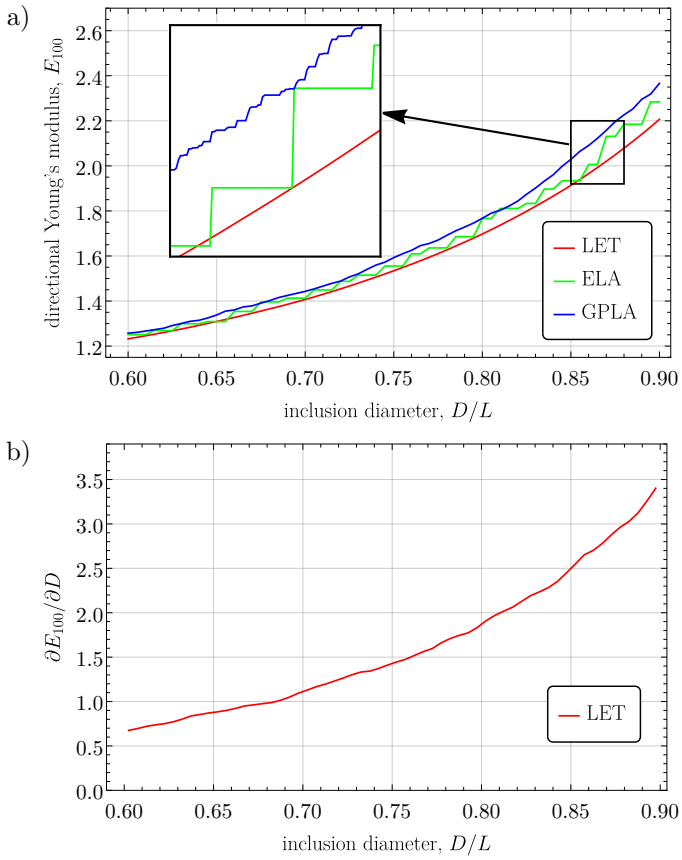

Fig. 6.11. a) Dependence of the directional Young's modulus, E_{100}, on the inclusion diameter D. The inset shows the results computed with a finer step so that the jumps are clearly visible for both ELA and GPLA; b) dependence of the derivative of the directional Young's modulus, $\partial E_{100}/\partial D$, on the inclusion diameter D.

6.4. Hyperelastic woven microstructure

In this example, unlike the previous ones, the internal geometry is more complex, and for this reason the real advantage of LET over conforming-mesh discretization can be appreciated. The model consists of a 3D periodic cell of the dimensions $L \times L \times H = 2 \times 2 \times 0.7$, in which four interlaced fibres are immersed in the matrix, Fig. 6.12.

For a coarse mesh, it may happen that one element is cut by two interfaces. Accordingly, as commented in Remark 4.1 in Section 4.2 and in Appendix B, a separate level-set function is introduced for each fibre. If an element is cut by two interfaces, so that it contains portions of the matrix and two fibres, the total volume fraction of the fibres is simply taken as the sum of the volume fractions of

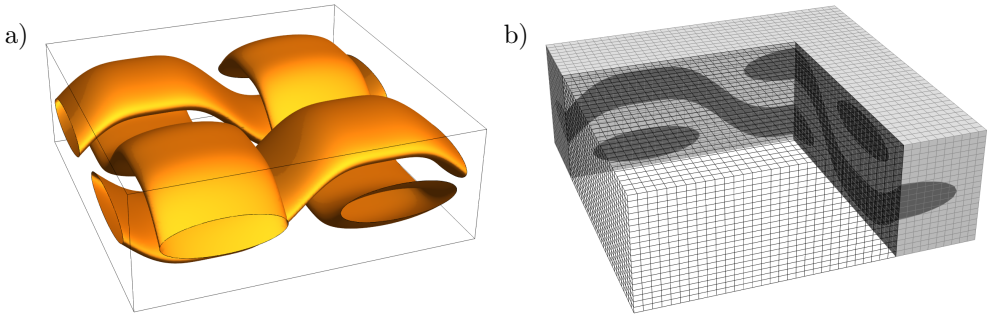

Fig. 6.12. Periodic woven-cell problem: a) geometry, b) finite-element mesh ($40 \times 40 \times 20$ elements).

the individual fibres and the lamination orientation is determined by averaging those determined individually for each interface.

The geometry of the fibres aligned with the x_2-axis is defined by the centreline $(\pm x_1^0, x_2, \mp x_3^0(x_2))$ parameterized by x_2 and by the elliptical cross-section (in the (x_1, x_3)-plane) specified by the following inequality

$$\sqrt{\left(\frac{x_1 \pm x_1^0}{a}\right)^2 + \left(\frac{x_3 \pm x_3^0(x_2)}{b}\right)^2} - 1 \leqslant 0, \tag{6.5}$$

where $a = 0.35$ and $b = 0.11$ are the semi-major and semi-minor axes of the ellipse, $x_1^0 = L/4$ defines the offset between the fibres in the x_1-direction, function $x_3^0(y)$ is specified as

$$x_3^0(x_2) = A\left(\frac{9}{8}\sin\left(\frac{2\pi x_2}{L}\right) + \frac{1}{8}\sin\left(\frac{6\pi x_2}{L}\right)\right), \tag{6.6}$$

and $A = 0.2$ is the amplitude of the function $x_3^0(x_2)$. The origin of the coordinate system is located at the centre of the unit cell. The geometry of the fibres aligned with the x_1-axis is defined analogously.

The finite-deformation framework is employed, and both the matrix and the fibres are assumed to be hyperelastic, characterized by a compressible neo-Hookean strain energy function. The elastic properties are specified as $E_1 = 100$ (fibres), $E_2 = 1$ (matrix), and $\nu_1 = \nu_2 = 0.45$.

Periodic boundary conditions are imposed and loading is applied by prescribing the overall deformation gradient $\bar{\boldsymbol{F}}$. Three deformation modes are considered, namely isochoric tension and two cases of simple shear. The isochoric tension along the x_1-axis is specified by

$$\bar{\boldsymbol{F}} = (1+\epsilon)\boldsymbol{e}_1 \otimes \boldsymbol{e}_1 + \frac{1}{\sqrt{1+\epsilon}}(\boldsymbol{e}_2 \otimes \boldsymbol{e}_2 + \boldsymbol{e}_3 \otimes \boldsymbol{e}_3), \tag{6.7}$$

where ϵ denotes the elongation, and $\boldsymbol{e}_i$ are the orthonormal basis vectors. The simple shear is specified by

$$\bar{\boldsymbol{F}} = \boldsymbol{I} + \gamma\, \boldsymbol{s} \otimes \boldsymbol{n}, \tag{6.8}$$

with $\boldsymbol{s} = \boldsymbol{e}_1$ and $\boldsymbol{n} = \boldsymbol{e}_2$ (case #1) and $\boldsymbol{s} = \frac{1}{\sqrt{2}}(\boldsymbol{e}_1 + \boldsymbol{e}_2)$ and $\boldsymbol{n} = \frac{1}{\sqrt{2}}(\boldsymbol{e}_2 - \boldsymbol{e}_1)$ (case #2).

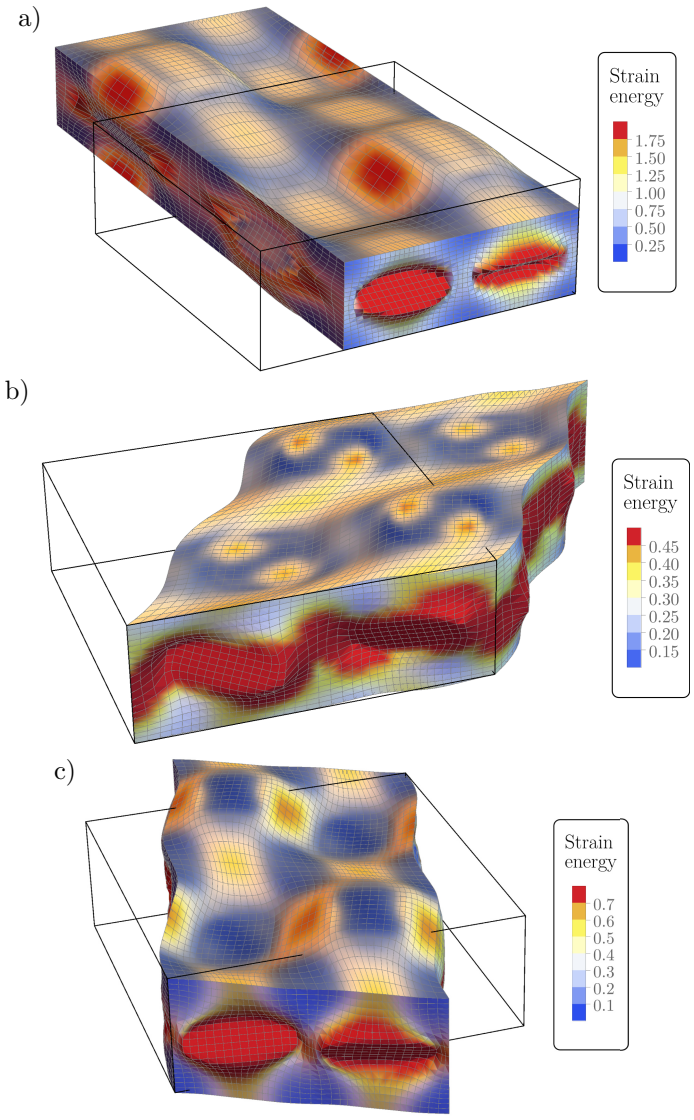

Fig. 6.13. Woven cell: deformed configuration for: a) isochoric tension ($\epsilon = 0.8$), b) simple shear (case #1, $\gamma = 0.7$), and c) simple shear (case #2, $\gamma = 0.7$). Colour maps show the elastic strain energy density ψ^{el}.

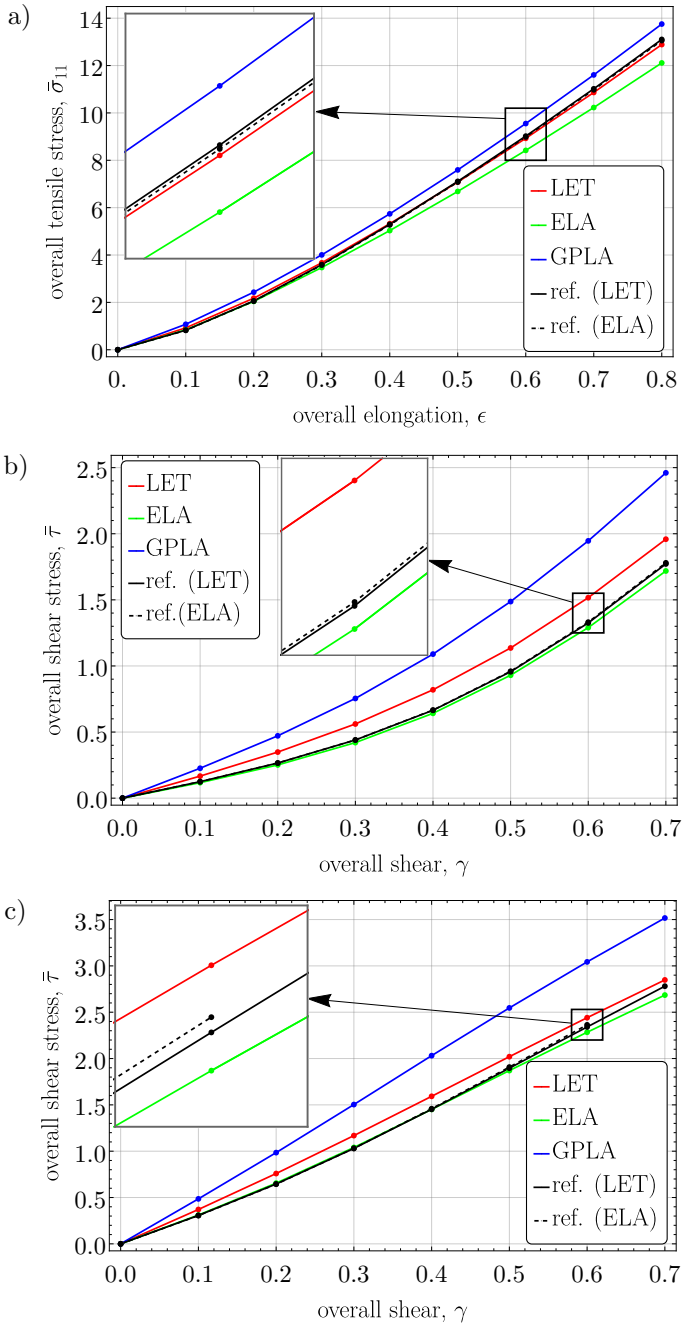

Fig. 6.14. Woven cell: overall stress–strain response for: a) isochoric tension, b) simple shear (case #1), and c) simple shear (case #2). The results correspond to the mesh of $20 \times 20 \times 10$ elements (element size $h = 0.1$). As a reference, the LET and ELA results obtained for a fine mesh ($80 \times 80 \times 40$ elements, $h = 0.025$) are used.

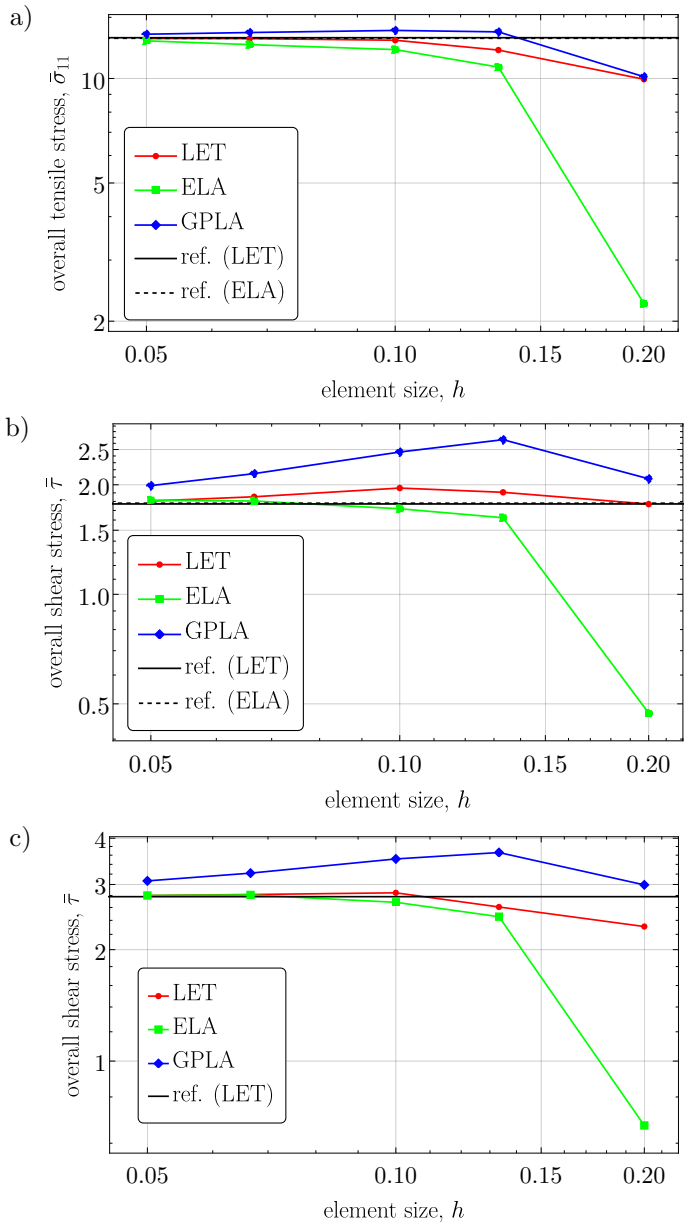

Fig. 6.15. Woven cell: convergence of the overall stress (at the maximum strain, see Fig. 6.14) with element size h for: a) isochoric tension, b) simple shear (case #1), and c) simple shear (case #2). As a reference, the LET and ELA results obtained for a fine mesh ($80 \times 80 \times 40$ elements, $h = 0.025$) are used.

In the convergence studies reported below, a family of regular meshes of hexahedral elements is used with 10 to 40 elements along the x_1- and x_2-directions

(element size h varied between 0.2 and 0.05) and with 5 to 20 elements in the x_3-direction, respectively. As a reference, the results obtained for a fine mesh of $80\times80\times40$ elements ($h = 0.025$) are used, and both LET and ELA are employed for this purpose (the two methods give very similar results; for ELA, in the simple shear case #2, the solution could not be achieved at the maximum load due to convergence problems). The F-bar formulation is employed to avoid volumetric locking effects [32]. Figure 6.13 illustrates the three deformation modes for the mesh of $40 \times 40 \times 20$ elements.

The overall stress–strain response predicted using the $20 \times 20 \times 10$ mesh is shown in Fig. 6.14. In the case of isochoric tension, the $\bar{\sigma}_{11}$ component of the overall Cauchy stress $\bar{\boldsymbol{\sigma}}$ is shown as a function of the overall elongation ϵ, Fig. 6.14a. In the case of simple shear, the shear stress $\bar{\tau} = \boldsymbol{s} \cdot \bar{\boldsymbol{\sigma}} \cdot \boldsymbol{n}$ is shown as a function of the overall shear γ, Figs. 6.14b and 6.14c. Results obtained for a four times finer mesh are included in Fig. 6.14 as a reference.

In Fig. 6.14, the mesh is relatively coarse, hence the visible differences between the three methods (LET, ELA, GPLA). In all cases, GPLA delivers the stiffest response, with the largest error with respect to the reference results. The remaining two methods (LET and ELA) deliver similar results that agree well with the reference ones, except for simple-shear case #1, where the LET results are visibly stiffer. Accordingly, for this specific mesh density ($h = 0.1$), ELA seems to perform the best. However, this conclusion does not apply to other mesh densities, as illustrated below.

Figure 6.15 shows the overall stress at the maximum strain as a function of the mesh size h. It follows that predictions of LET are stable (i.e., reasonably close to the reference solution) over the entire range of mesh densities studied. Likewise, GPLA delivers stable results, although with a significantly higher error. On the other hand, ELA performs badly for coarser meshes, which is associated with a poor representation of the internal geometry by ELA.

6.5. Elasto-plastic composite

In this example, a 2D periodic unit cell with a circular inclusion is considered. Both phases are elastic-plastic and plane-strain conditions are assumed. In the continuum setting, the position of the inclusion within the unit cell is arbitrary in view of periodicity, and it does not affect the overall response. This is not the case in the discrete setting when the position of the inclusion with respect to the finite-element mesh is an additional geometric feature that may affect the response, as revealed by the preliminary studies. Accordingly, in this section, this effect is examined in detail. Specifically, the overall response under simple shear is studied for 100 randomly selected positions of the inclusion and for a family of regular meshes of $N \times N$ elements with $N = 2, 4, 8, ..., 256$.

Below, for each method considered (LET, ELA, GPLA), the responses obtained for a given mesh density are averaged and compared to the reference ("exact") solution obtained using a high-resolution conforming mesh involving over 3 million elements. The standard deviation is also examined as an indicator of the sensitivity of the response to the position of the inclusion.

The geometric and material parameters adopted in this example are the following. The dimensions of the unit cell are $L \times L$ with $L = 2$, and the inclusion radius is $R = 0.6$. The finite-deformation framework is adopted and both phases are governed by the finite-strain J_2 plasticity model with linear isotropic hardening, see C for more details. The yield stress σ_y is thus specified by $\sigma_y(\alpha) = \sigma_y^0 + K\alpha$, where α denotes the accumulated plastic strain. The elastic properties of the matrix and inclusion are the same, $E = 70\,000$, $\nu = 0.25$, and so is the hardening modulus $K = 2000$. The initial yield stress of the inclusion, $\sigma_{y,1}^0 = 70$, is lower than that of the matrix, $\sigma_{y,2}^0 = 120$, which induces an inhomogeneous deformation within the unit cell once plastic deformation occurs.

The unit cell is loaded in simple shear by prescribing the overall deformation gradient $\bar{\boldsymbol{F}}$ according to Eq. (6.8) with $\boldsymbol{s} = \boldsymbol{e}_1$ and $\boldsymbol{n} = \boldsymbol{e}_2$. The initial stage of deformation is considered with the overall shear γ increasing from 0 to 0.004 so that the details of the elastic-to-plastic transition are revealed. A sample finite-element mesh with the inclusion at a sample position within the unit cell is shown in Fig. 6.16a, and the deformation mode along with the shear component σ_{12} of the Cauchy stress tensor are shown in Figs. 6.16b–d for three selected mesh densities.

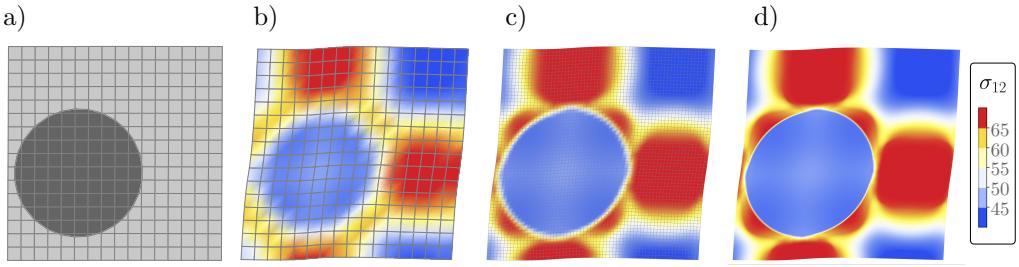

Fig. 6.16. Elasto-plastic composite: a) 16×16 mesh with a randomly positioned circular inclusion; b)–d) deformed mesh (displacements scaled 20 times) with the distribution of the shear component σ_{12} of the Cauchy stress tensor for 16×16 (b), 64×64 (c) and 256×256 (d) mesh.

Figure 6.17 shows the overall stress–strain response ($\bar{\sigma}_{12}$ component of the overall Cauchy stress as a function of the overall shear γ) for a coarse mesh of 4×4 elements. Here, the average response is compared to the reference solution and, moreover, the shaded area represents the spread of the individual responses

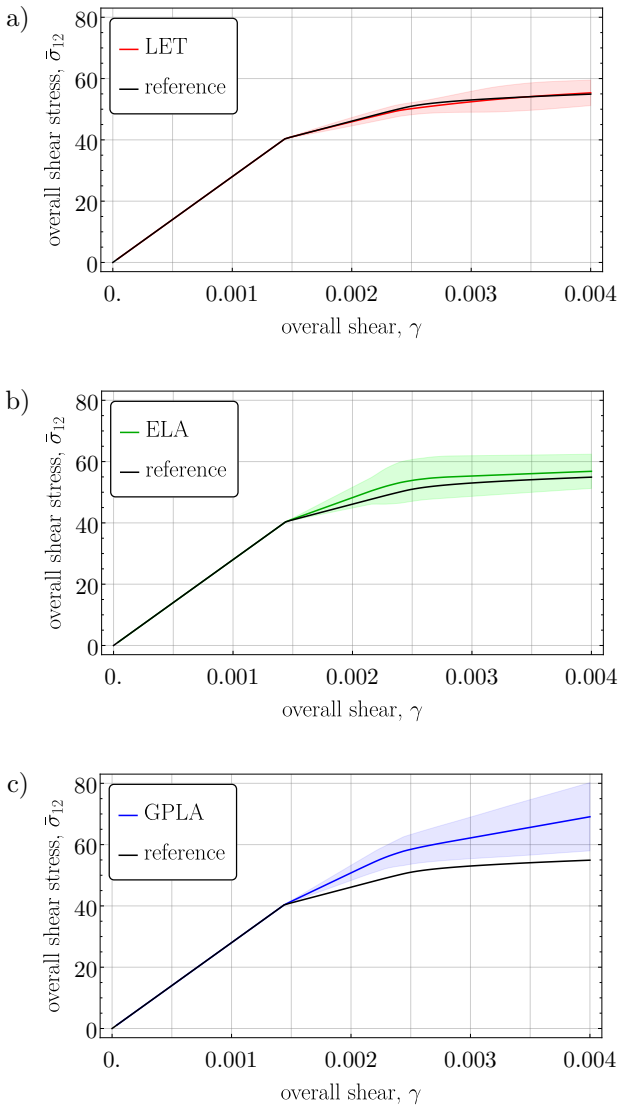

Fig. 6.17. Elasto-plastic composite: overall stress–strain ($\bar{\sigma}_{12}$–γ) response obtained for the 4×4 mesh (element size $h = 0.5$) and for: a) LET, b) ELA, and c) GPLA. In each case, the average over 100 random inclusion positions is indicated by a solid line and the corresponding shaded area indicates the spread (± 3 standard deviations).

corresponding to the randomly positioned inclusions (the width of the shaded area is set equal to ± 3 standard deviations). Since the mesh is here coarse (4×4 elements), visible differences with respect to the reference solution are apparent. It can be seen that LET delivers the most accurate results in terms of both the

average and the spread. The accuracy is visibly worse in the case of ELA and significantly worse in the case of GPLA.

Convergence of the results with mesh refinement is illustrated in Fig. 6.18. This figure, in addition to simple shear, includes also the results corresponding to isochoric tension (i.e., pure shear). In the case of LET and ELA, the averaged stress converges quickly to the reference value, LET converging somewhat faster. However, in the case of LET, the spread vanishes significantly faster than in the case of ELA. Consistent with the other results, the accuracy of GPLA is the worst.

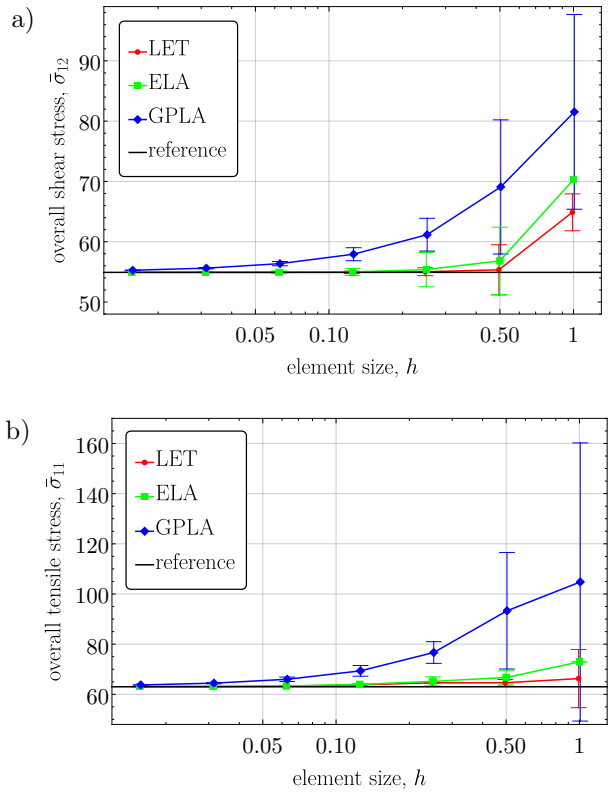

Fig. 6.18. Elasto-plastic composite: dependence of the average overall stress on the element size h for: a) simple shear (shown is the shear stress at $\gamma = 0.004$) and b) isochoric tension (shown is the tensile stress at the elongation of 0.004). The error bars indicate the spread (± 3 standard deviations).

Note that in the case of ELA, the results obtained for the coarsest mesh considered (2×2 elements, $h = 1$) exhibit no spread, see Fig. 6.18. This is because in this case all elements are assigned to the matrix phase regardless of the position of the inclusion (and the unit cell is thus homogeneous).

6.6. Summary

Several numerical examples have been studied and the proposed approach has been shown to be, in most cases, superior in terms of accuracy to two alternative methods in which the whole element or individual Gauss points are assigned to a specific phase. However, the rate of convergence with mesh refinement is not improved, and therefore, in terms of accuracy, the proposed method cannot compete, and is not aimed to compete, with more sophisticated methods, such as X-FEM, which can achieve the optimal convergence rate typical for conforming-mesh FEM. On the other hand, it is an important feature of the proposed approach that the response is a continuous function of the position of the interface, which opens the possibility of its application in various problems involving moving interfaces. This compelling proposition will undergo scrutiny in the subsequent chapter, where the LET-PF method (LET combined with the phase-field method) will be systematically examined in the context of challenges including moving interfaces.

7. Numerical experiments – moving interfaces*

7.1. Evolving circular inclusion

The aim of this study is to evaluate the overall performance of LET-PF and to compare it to the conventional phase-field method (abbreviated to PFM in the sequel) for a 2D problem that has an analytical solution, to be used as a reference. The sharp-interface problem is specified first, followed by the description of the computational model and by the results of a comprehensive study.

7.1.1. Sharp-interface benchmark problem

An elastic circular domain Ω_2 (matrix) of the radius R and an evolving elastic circular inclusion Ω_1 of the radius $\rho = \rho(t)$ are considered, see Fig. 7.1a. The phase transformation and thus the evolution of the inclusion are induced by the internal stresses resulting from the volumetric eigenstrain $\boldsymbol{\varepsilon}_1^{\mathrm{t}} = \epsilon \boldsymbol{I}$ in the

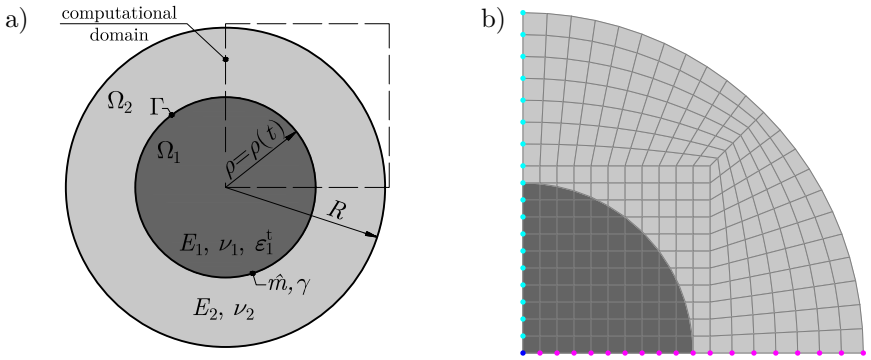

Fig. 7.1. Evolving circular inclusion: a) scheme of the problem; b) computational domain with a regular (non-conforming) mesh of quadrilateral elements. A coarse mesh of 11×11 elements within the internal square part (element size $h = 0.1$) is shown, the actual computations are carried out using significantly finer meshes.

*The content of this chapter has been entirely excerpted from the article of Dobrzański and Stupkiewicz [34]. Minor modifications may have been applied to the text and figures.

inclusion and by the energy of the interface Γ of the density γ. Propagation of the interface is assumed to be governed by the viscous kinetic law, cf. Eq. (3.48),

$$\hat{v}_n = -\dot{\rho} = \hat{m}\hat{f}, \qquad \hat{f} = \hat{f}_{\text{bulk}} + \hat{f}_{\text{int}}, \tag{7.1}$$

where $\hat{f}_{\text{bulk}}$ and $\hat{f}_{\text{int}}$ denote the local thermodynamic driving forces originating from the bulk and interfacial energy, respectively. The outer boundary is assumed to be free.

The sharp-interface problem specified above is a 1D problem and admits an analytical solution that is derived in Appendix E. In the special case of identical elastic properties of the two phases, the evolution of the inclusion radius is governed by the following differential equation, cf. Eq. (E.13),

$$\dot{\rho} = -\frac{\hat{m}\gamma}{\rho}\left(1 + A\frac{\rho}{\rho_0}\left(\frac{1}{2} - \left(\frac{\rho}{R}\right)^2\right)\right), \qquad A = \frac{\rho_0 E\epsilon^2}{(1-\nu^2)\gamma}, \tag{7.2}$$

where ρ_0 denotes the initial radius of the inclusion, E is Young's modulus and ν is Poisson's ratio. Note that a dimensionless parameter A has been introduced which combines all the problem parameters related to both the elastic strain energy and the interfacial energy (the chemical energy contribution is not considered, hence the elastic strain energy is the only contribution to the bulk energy). For small values of A, the evolution is mainly governed by the interfacial energy, and for large values of A by the elastic strain energy. Exact integration of Eq. (7.2) is not possible; integration is thus performed numerically.

The explicit formulae for the driving force contributions $\hat{f}_{\text{bulk}}$ and $\hat{f}_{\text{int}}$ are given by Eq. (E.15). Specifically, $\hat{f}_{\text{int}} = \gamma/\rho$ is the driving force originating from the interfacial energy of the density γ, and the interface curvature is $1/\rho$. The driving force $\hat{f}_{\text{bulk}}$ originates from the elastic strain energy induced by the inclusion eigenstrain. It is proportional to the elastic modulus E and squared eigenstrain magnitude ϵ^2 and depends on the geometrical factor ρ/R. For $\rho_0 = R/2$, as assumed in the computations below, the driving force $\hat{f} = \hat{f}_{\text{bulk}} + \hat{f}_{\text{int}}$ is positive and hence $\dot{\rho}$ is negative, which means that the inclusion decreases in size and ultimately vanishes.

7.1.2. Computational model

The two methods (LET-PF and PFM) involve identical material and numerical parameters, including those related to the finite-element model, and the specifications provided below apply to both methods. The finite-element computations are carried out in 2D on a computational domain encompassing one quarter of the circular domain with adequate symmetry conditions imposed along the horizontal and vertical edges, see Fig. 7.1b. In the computations, it is assumed that the material properties of the inclusion and matrix are identical

with Young's modulus $E = 1$ and Poisson's ratio $\nu = 0.25$. The radius of the domain is $R = 2$, and the initial radius of the inclusion is $\rho_0 = 1$. The volumetric eigenstrain of the inclusion is assumed as $\epsilon = 0.1$. The effective mobility parameter is set to $\hat{m} = 1$, and the actual mobility parameter m used in the computations is then specified as a function of ℓ according to Eq. (3.57).

One of the goals here is to study the performance of LET-PF over a wide range of the values of the interfacial energy density γ. To this end, the values of γ have been chosen from within the range $\gamma \in [0.0001, 0.003]$ (12 values have been chosen), so that the dimensionless parameter A varies within the range $A \in [3.6, 107.]$. This range has been chosen such that the extreme values correspond to two regimes of interest. For $\gamma = 0.0001$ ($A = 107.$), the bulk contribution $\hat{f}_{\text{bulk}}$ to the driving force is much greater than the interfacial contribution $\hat{f}_{\text{int}}$ over nearly the whole range of inclusion radii ρ (note that $\hat{f}_{\text{int}} \to \infty$ for $\rho \to 0$), see Fig. 7.2. Accordingly, in this (elasticity-driven) regime, evolution is mostly governed by the elastic strain (bulk) energy. On the other hand, for $\gamma = 0.003$ ($A = 3.6$), both contributions are initially of the same order, see Fig. 7.2. The third regime, in which $\hat{f}_{\text{int}} \gg \hat{f}_{\text{bulk}}$, is not interesting here because the evolution is then fully governed by the interfacial energy and the effect of LET-PF is negligible. Moreover, it has been checked that the response and the performance of both methods are then quite similar as for $\hat{f}_{\text{int}} \approx \hat{f}_{\text{bulk}}$.

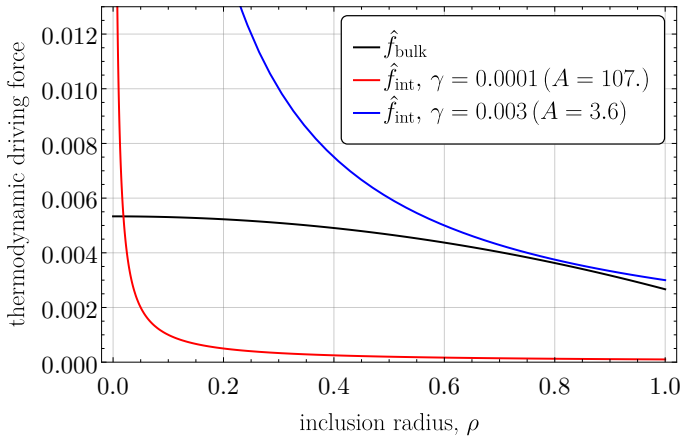

Fig. 7.2. Thermodynamic driving forces $\hat{f}_{\text{bulk}}$ and $\hat{f}_{\text{int}}$ as a function of the inclusion radius ρ, see Eq. (E.15).

The impact of the interface thickness parameter ℓ on the accuracy of the results is also examined, with the values of ℓ specified relative to the characteristic element size h, namely, $\ell/h \in \{0.75, 1, 1.5, 2\}$. As mentioned earlier, for the selected parameter values, the inclusion disappears completely during the evolution process by gradually reducing its radius to zero. Therefore, a regu-

lar grid of square finite elements is employed in the central region containing the inclusion, and quadrilateral elements with somewhat less regular shapes are employed in the remaining part of the domain, as depicted in Fig. 7.1b. The main computations are performed for two mesh sizes, $h = 0.02$ and $h = 0.01$, which correspond to, respectively, 55×55 and 110×110 elements in the central region. At the initial time $t = 0$, the initial profile of the order parameter ϕ is prescribed according to formula (3.56) with ξ replaced by the radius r and ξ_0 replaced by the initial inclusion radius ρ_0.

In all computations, an adaptive time incrementation scheme has been used, such that the time increment is increased or decreased depending on the current convergence behaviour. In each case, the maximum time increment $\Delta t_{\max}$ has been prescribed relative to T_{exact}, the time of the complete evolution as resulting from the analytical solution.

The results will be presented in terms of the mean inclusion radius $\bar{\rho}$ which is defined as the average radius of the inclusion defined by the $\phi = \frac{1}{2}$ level set. The individual radii are measured along a number of directions taken every 1 degree.

7.1.3. Results

The time evolution of the mean inclusion radius $\bar{\rho}$ is shown in Fig. 7.3 for the two extreme values of the interfacial energy, $\gamma = 0.0001$ and $\gamma = 0.03$. As a reference, the analytical solution is also included in Fig. 7.3.

The computations have been performed with small time increments, $\Delta t_{\max} = T_{\text{exact}}/500$, so that the error introduced by the time integration is insignificant. It can be seen that, in the elasticity-driven regime ($\gamma = 0.0001$), PFM is highly inaccurate (Fig. 7.3b), while LET-PF performs much better (Fig. 7.3a). In the interfacial-energy-driven regime ($\gamma = 0.003$), both methods perform similarly well. Figure 7.3 illustrates also a significant effect of the interface thickness parameter ℓ.

The effect of mesh density and time increment is illustrated in Fig. 7.4 for an intermediate value of the interfacial energy, $\gamma = 0.0008$. In addition to the small time increment ($\Delta t_{\max} = T_{\text{exact}}/500$) and thus highly accurate time integration, see the top figures in Fig. 7.4, the analysis has also been performed with no restriction on the time increment ($\Delta t_{\max} = T_{\text{exact}}$) so that the actual time increments result from the current convergence behaviour and are significantly larger, see the bottom figures in Fig. 7.4. It can be seen that the effect of the time step is significant. As discussed later, the number of time steps needed to complete the simulation can be (and will be) used as a measure of the robustness of the model. Concerning the effect of mesh density, it is more pronounced in the case of PFM than LET-PF. Again, this effect will be studied in more detail later.

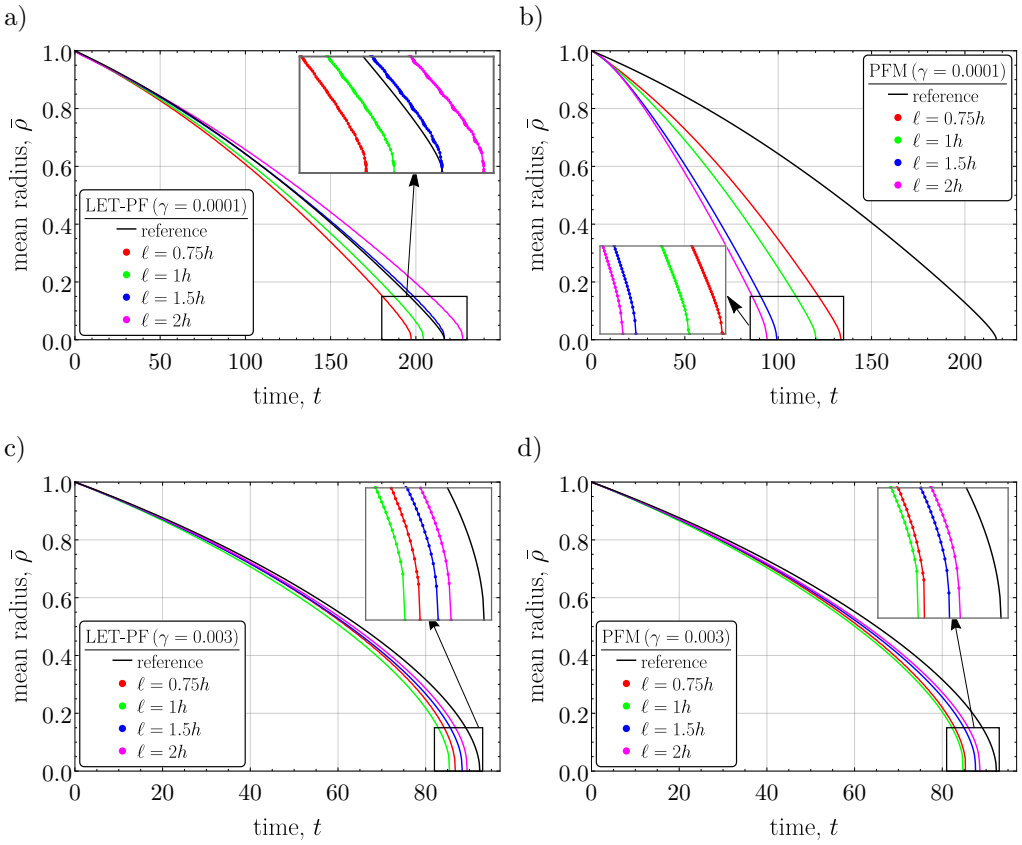

Fig. 7.3. Time evolution of the mean inclusion radius $\bar{\rho}$ predicted by LET-PF (a, c) and PFM (b, d) for $\gamma = 0.0001$ (a, b) and for $\gamma = 0.003$ (c, d). The computations are performed using a coarse mesh, $h = 0.02$, and small time increment, $\Delta t_{\max} = T_{\text{exact}}/500$. As a reference, the analytical solution is depicted by a solid black line.

Figure 7.5 shows the maps of the order parameter ϕ, radial stress σ_{rr} and hoop stress $\sigma_{\theta\theta}$ at the instant when the inclusion radius reaches $\bar{\rho} \approx 0.85$. While the order parameter ϕ and the hoop stress $\sigma_{\theta\theta}$ exhibit no substantial differences between LET-PF and PFM, the radial stress σ_{rr}, which according to the analytical solution should be continuous at the interface, is better represented by LET-PF. This is particularly evident along the horizontal and vertical edges of the computational domain, as the interface is then approximately parallel to the element edges and the LET technique is then highly accurate [35]. A more profound insight into these fields behaviours is presented in Fig. 7.6, showing the profiles of the radial and hoop stresses along the horizontal direction. Regarding the radial stress, as shown in Fig. 7.6a, a significant distinction between the two methods is readily apparent. PFM exhibits fluctuations within the interface re-

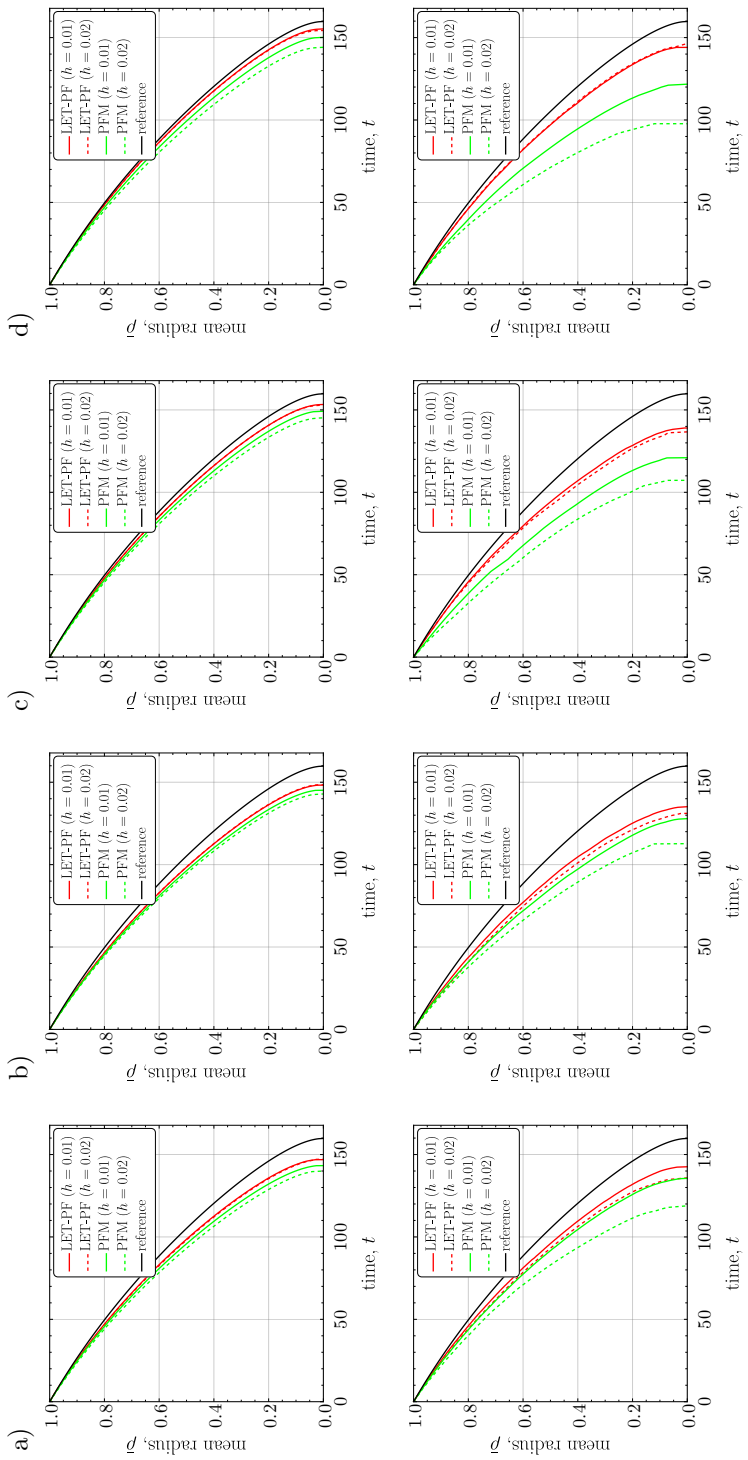

Fig. 7.4. Time evolution of the mean inclusion radius $\bar{\rho}$ for $\gamma = 0.0008$: a) $\ell = 0.75h$, b) $\ell = h$, c) $\ell = 1.5h$, d) $\ell = 2h$. The results shown in the top row are obtained for a small time increment (adaptive time stepping with $\Delta t_{\max} = T_{\text{exact}}/500$), and those in the bottom row for significantly larger time increments ($\Delta t_{\max} = T_{\text{exact}}$).

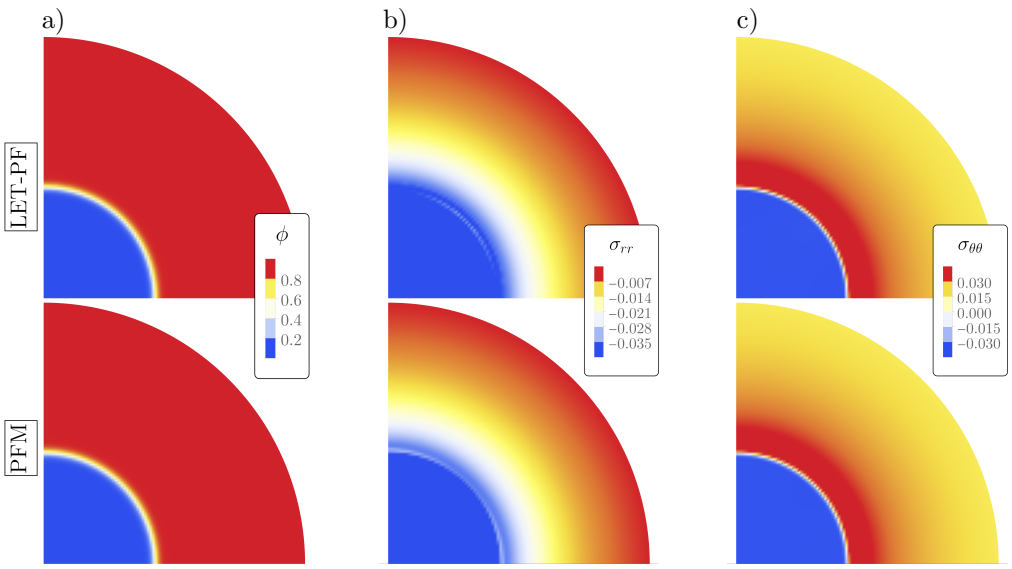

Fig. 7.5. Maps of the order: a) parameter ϕ, b) radial stress σ_{rr}, and c) hoop stress $\sigma_{\theta\theta}$ obtained using LET-PF (top) and PFM (bottom) at the instant when the inclusion radius reaches $\bar{\rho} \approx 0.85$ ($\gamma = 0.0008$, $h = 0.02$, $\ell = 1.5h$).

gion, while LET-PF produces results much closer to the analytical solution. As for the hoop stress, as illustrated in Fig. 7.6b, the situation appears somewhat different–both methods seem to yield a similar response. However, it is crucial to note that, when utilizing LET-PF, the information is available also about the local strains and stresses resulting from the homogenization process in the laminated elements. The local stresses are indicated in the insets in Fig. 7.6 by markers, thereby revealing that LET-PF provides also the local response that aligns more closely with the analytical solution.

The results presented in Figs. 7.3 and 7.4 suggest that LET-PF outperforms PFM in terms of accuracy. To examine the accuracy and efficiency of LET-PF in more detail, a comprehensive study has been performed by varying the governing material and numerical parameters. The material parameters are fully characterized by the dimensionless parameter A, Eq. $(7.2)_2$, and this parameter is controlled by varying the interfacial energy γ, as described above, while the remaining material parameters are fixed. Concerning the numerical parameters, two mesh densities are considered, $h \in \{0.01, 0.02\}$, four values of the interface thickness parameter, $\ell/h \in \{0.75, 1, 1.5, 2\}$, and two values of the maximum time increment, $\Delta t_{\max} \in \{T_{\text{exact}}, T_{\text{exact}}/500\}$.

As shown in Fig. 7.2, when the inclusion radius approaches zero, the thermodynamic driving force, and specifically its interfacial contribution $\hat{f}_{\text{int}}$, increases to infinity. The evolution is then fully governed by $\hat{f}_{\text{int}}$ and the difference between

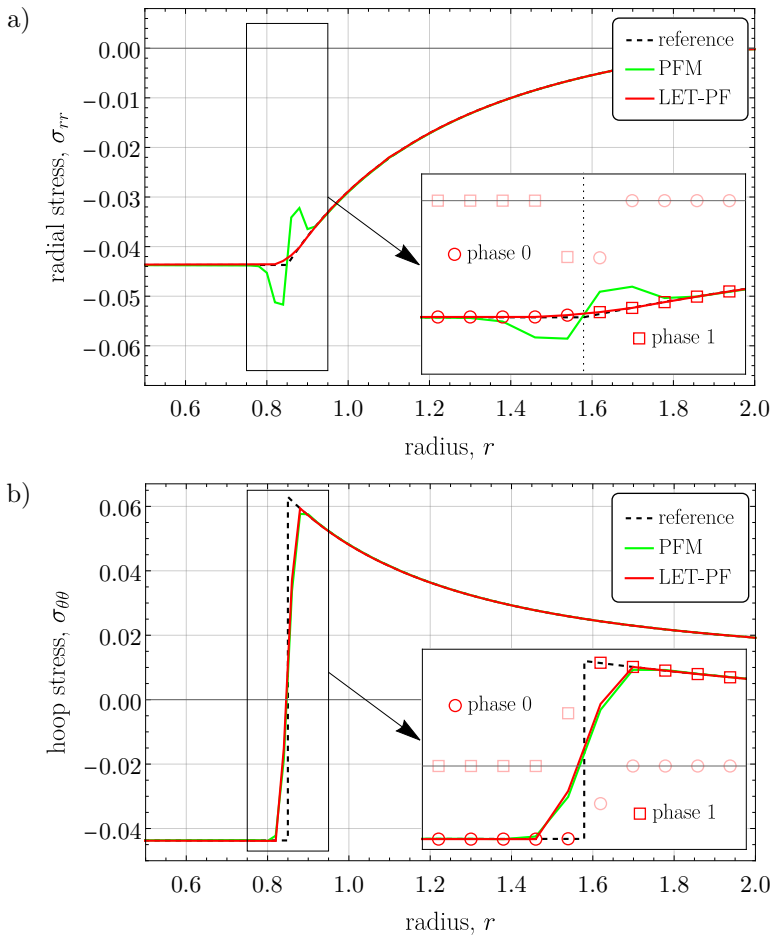

Fig. 7.6. Profiles of the: a) radial stress σ_{rr} and b) hoop stress $\sigma_{\theta\theta}$ along the bottom edge of the computational domain ($\bar{\rho} \approx 0.85$, $\gamma = 0.0008$, $h = 0.02$, $\ell = 1.5h$). The lines depict the overall stresses, while the markers in the insets represent the local stresses within each phase, as predicted by LET-PF.

LET-PF and PFM diminishes. Moreover, the radius of curvature of the interface becomes then small compared to the element size and interface thickness so that additional effects influence the solution. Accordingly, in the following, the final part of the evolution is excluded from the analysis, and only the range of the inclusion radii between ρ_0 and $0.15\rho_0$ is considered. The corresponding duration of the evolution process, resulting from the analytical solution, depends on A and is denoted by T_{exact}. The maximum time increment $\Delta t_{\max}$ in the adaptive time incrementation scheme is then expressed in terms of T_{exact}, as specified above.

Figure 7.7 presents the relative error as a function of parameter A. The relative error is defined here as

$$\text{relative error} = \frac{\displaystyle\int_{0.15\rho_0}^{\rho_0} |\tau^{\text{exact}}(r) - \tau^{\text{num}}(r)|\,\mathrm{d}r}{\displaystyle\int_{0.15\rho_0}^{\rho_0} \tau^{\text{exact}}(r)\,\mathrm{d}r}, \tag{7.3}$$

where $\tau = \rho^{-1}$ is the inverse function of $\rho(t)$ that describes the time as a function of the inclusion radius, and τ^{exact} and τ^{num} correspond to the analytical

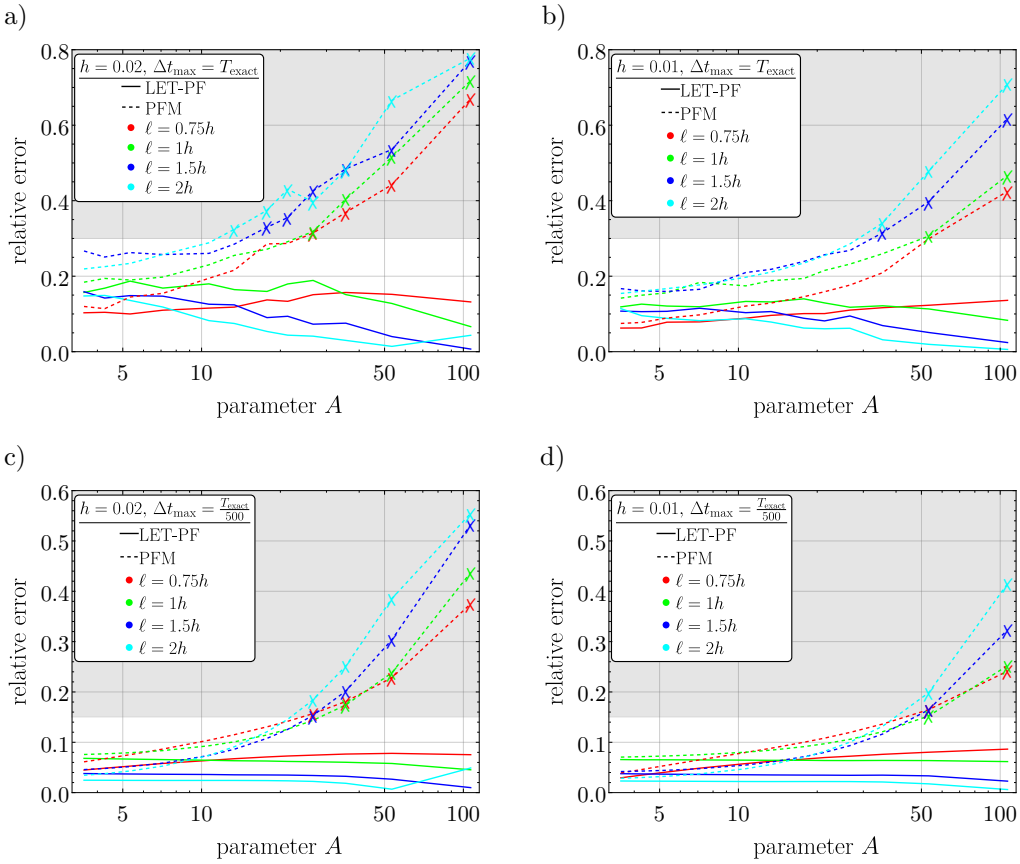

Fig. 7.7. Relative error, Eq. (7.3), evaluated for all considered cases for LET-PF (solid lines) and PFM (dashed lines). The shaded regions correspond to the error that is approximately twice higher than the average error of LET-PF, i.e., exceeding 0.3 for $\Delta t_{\max} = T_{\text{exact}}$ (panels a and b) and exceeding 0.15 for $\Delta t_{\max} = T_{\text{exact}}/500$ (panels c and d). The data points falling within the shaded regions are marked with crosses, see also Fig. 7.8.

and numerical solutions, respectively. The use of the inverse function ρ^{-1} is here necessary because the duration of the evolution process in each simulation is, in general, different than the duration in the analytical solution so that integration of $|\rho^{\text{exact}}(t) - \rho^{\text{num}}(t)|$ would not be feasible. The integration in Eq. (7.3) is performed numerically using the trapezoidal rule. The results in Fig. 7.7 illustrate that, in terms of accuracy, LET-PF outperforms PFM in all cases studied. Although both methods exhibit similar trends for lower values of A (where the interfacial energy has a greater contribution), LET-PF demonstrates superior performance as the contribution of the bulk (elastic) energy becomes more prominent. This is particularly evident in Figs. 7.7a and 7.7b, where the errors for PFM reach extreme values of nearly 0.8, while LET-PF performs much better. In general, it can be seen that the accuracy of LET-PF only weakly depends on A.

Figure 7.8 shows the number of time steps needed to complete the simulation for all cases included in Fig. 7.7. When there is no restriction on the maxi-

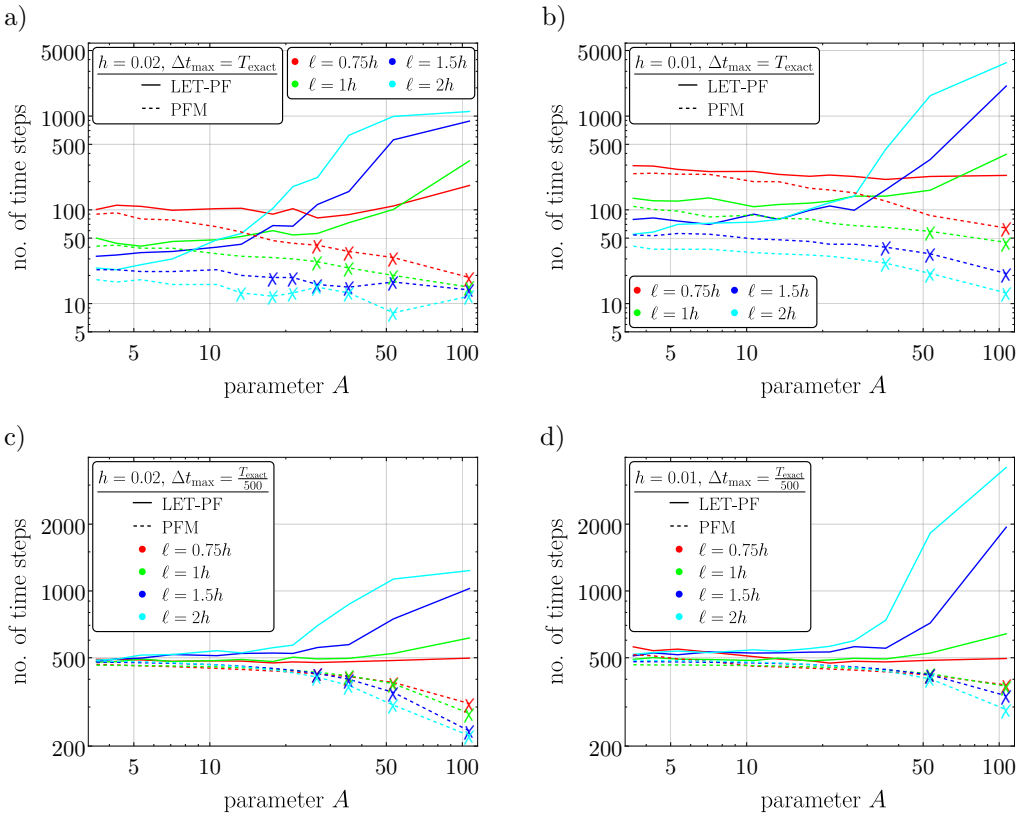

Fig. 7.8. The number of time steps needed to complete the simulation for $\Delta t_{\max} = T_{\text{exact}}$ (a, b) and for $\Delta t_{\max} = T_{\text{exact}}/500$ (c, d). Two mesh sizes are used, namely $h = 0.02$ (a, c) and $h = 0.01$ (b, d). The results correspond to the cases shown in Fig. 7.7, and the cross markers indicate the data points of exceedingly high error, see Fig. 7.7.

mum time increment ($\Delta t_{\max} = T_{\text{exact}}$), so that the simulation proceeds with the time increment dictated by the current convergence behaviour, the number of time steps may serve as an indicator of the robustness of the computational scheme (the smaller the number of time steps, the more robust the scheme). Moreover, the number of time steps quantifies the computational cost since the total computation time is proportional to the number of time steps. However, in terms of the cost, the comparison of LET-PF and PFM is not immediate, because the cost of evaluation of the element quantities (residual vector and tangent matrix) differs for the two methods. The corresponding results are presented in Figs. 7.8a and 7.8b. It can be seen that, for small A, the number of time steps is similar for both methods, PFM being slightly more efficient. For high values of A, the number of time steps significantly increases for LET-PF, while it slightly decreases for PFM. However, caution is needed when interpreting these results. As has been shown in Fig. 7.7, PFM is highly inaccurate for high A, and the corresponding data points are marked with crosses in Fig. 7.8, consistent with Fig. 7.7. It follows that PFM is indeed cheaper and more robust for high A, but it is then unacceptable in terms of accuracy. On the other hand, for high A, LET-PF can only proceed with small time increments, but it delivers results of similar accuracy as for small A.

When the time increment is small ($\Delta t_{\max} = T_{\text{exact}}/500$), for small and intermediate A, the simulation proceeds with the prescribed maximum time increment, and the number of time steps is close to 500 for both LET-PF and PFM, see Figs. 7.8c and 7.8d. For high A, in the case of LET-PF, the number of time steps increases as in the case of $\Delta t_{\max} = T_{\text{exact}}$. On the other hand, in the case of PFM, the number of time steps decreases for high A, and this is related to the high error of the method and to the related reduction of the duration of the evolution process, see, for instance, Fig. 7.3b. Note that the corresponding data points are marked by crosses, as in Fig. 7.7.

The results reported in Fig. 7.7 show that the relative error significantly depends on the parameter A, on the maximum time increment $\Delta t_{\max}$, and on the interface thickness parameter ℓ. The effect of mesh density, although present, is hard to perceive as the other dependencies prevail. Accordingly, additional computations have been performed in which four mesh densities have been used, $h \in \{0.05, 0.02, 0.01, 0.005\}$, and two scenarios concerning the interface thickness parameter ℓ have been considered. In the first scenario, ℓ is proportional to the mesh size h and is set to $\ell = h$. In the second scenario, ℓ is set to a constant value $\ell = 0.02$ so that $\ell/h \in \{0.4, 1, 2, 4)$. The simulations are performed for $\gamma = 0.0008$ and $\Delta t_{\max} = T_{\text{exact}}/200$. Figure 7.9 shows the total elastic strain energy Ψ_{el} as a function of the mean inclusion radius $\bar{\rho}$.

The energy is normalized by the area of the inclusion, $\Psi_{\text{el}}/(\pi\bar{\rho}^2)$, so that the differences between the individual curves are better visible. It can be seen that LET-PF outperforms PFM in both scenarios. In the first scenario ($\ell = h$),

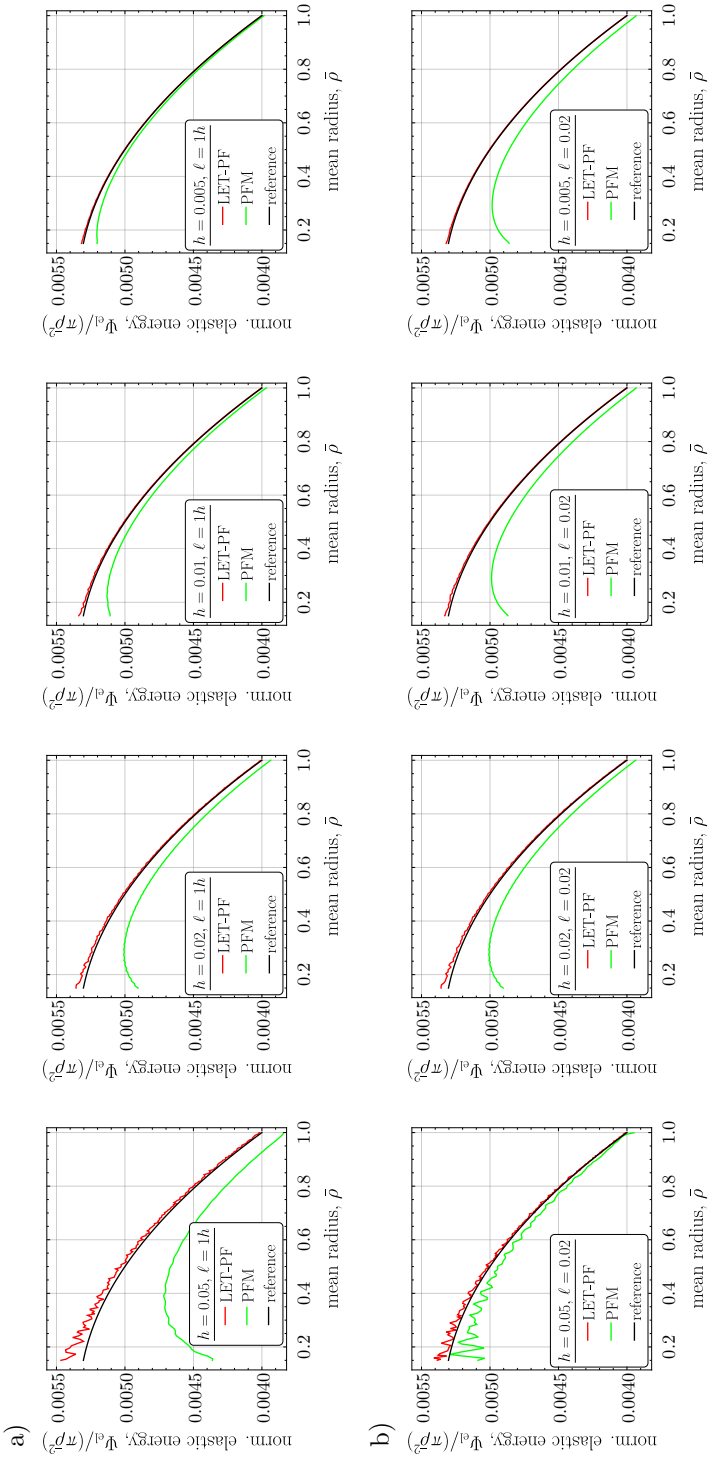

Fig. 7.9. Normalized total elastic strain energy $\Psi_{\text{el}}/(\pi\bar{\rho}^2)$ as a function of the mean radius $\bar{\rho}$ for increasing mesh density (element size h decreases from left to right) and for two scenarios: a) $\ell = h$, b) $\ell = 0.02$ ($\gamma = 0.0008$, $\Delta t_{\max} = T_{\text{exact}}/200$).

LET-PF converges to the analytical solution visibly faster than PFM, see Fig. 7.9a. This is because LET-PF treats the interface in a semisharp manner, and it is the diffuseness of the interface in PFM that is the source of the observed error. This is illustrated in Fig. 7.9b, where the interface thickness is kept constant ($\ell = 0.02$) and PFM converges to a solution that is significantly different from the correct one, particularly at small $\bar{\rho}$, when the interface thickness is large relative to the inclusion radius. At the same time, the large thickness of the interface does not affect the performance of LET-PF because the $\phi = \frac{1}{2}$ level set, which specifies the actual interface in the elasticity problem, only weakly depends on the thickness of the diffuse interface.

Since the reference sharp-interface problem is axisymmetric and the interface Γ is then a circle, any deviation from the circular shape can be treated as a measure of the numerical solution error. As a quantitative measure of this deviation, the coefficient of variation of the radius can be calculated at each time instant,

$$\mathrm{CV}_\rho = \frac{\sigma_\rho}{\bar{\rho}}, \tag{7.4}$$

where σ_ρ is the standard deviation of the orientation-dependent inclusion radius $\rho(\theta)$. Some representative results presenting CV_ρ as a function of the mean inclusion radius $\bar{\rho}$ are shown in Fig. 7.10. It follows that the deviation from the circular shape depends on the model parameters and varies during the evolution process, including small oscillations resulting from the interface traversing the finite-element mesh. Anyway, the deviation is relatively small in all cases (typically $\mathrm{CV}_\rho < 0.02$).

In order to comprehensively investigate this characteristic, the mean value of CV_ρ has been calculated for each case,

$$\overline{\mathrm{CV}_\rho} = \frac{1}{0.85\rho_0} \int_{0.15\rho_0}^{\rho_0} \mathrm{CV}_\rho \,\mathrm{d}\rho, \tag{7.5}$$

and the aggregated results, separately for the two mesh sizes, are shown in Fig. 7.11. This analysis reveals that both LET-PF and PFM result in a low mean value of the coefficient of variation of the radius with a maximum value of less than 2%. However, it can be seen that, for the interface thickness $\ell = 0.75h$, for both methods the deviation from the circular shape is higher than for larger interface thicknesses, which can be attributed to the interface pinning which is expected to diminish with the interface thickness increasing relative to the element size.

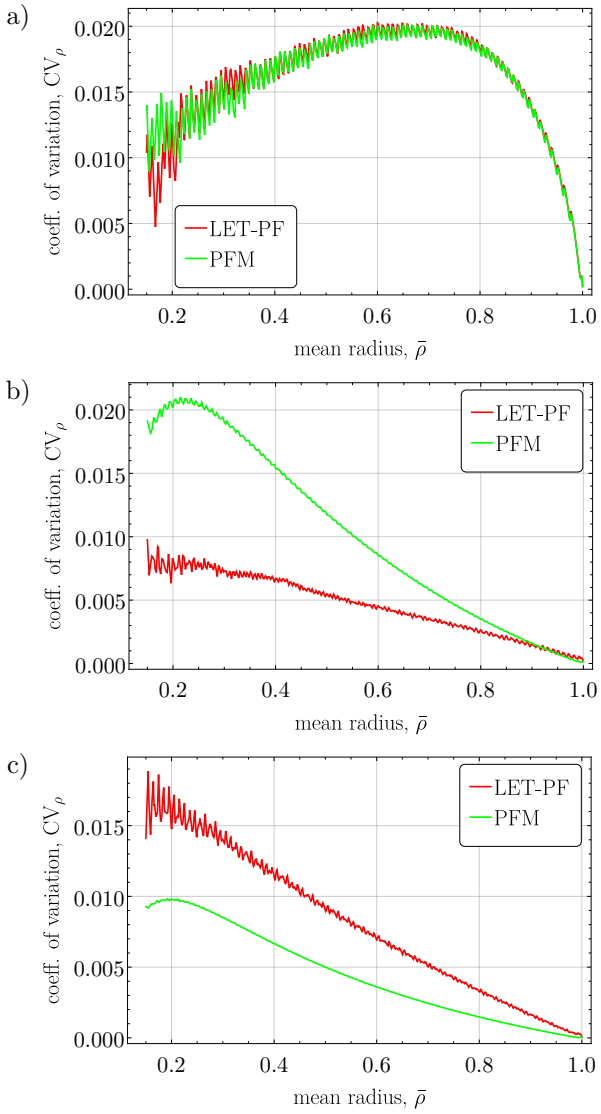

Fig. 7.10. Deviation of the inclusion shape from a circular one, quantified by the coefficient of variation of the radius, CV_ρ, Eq. (7.4), as a function of the mean inclusion radius $\bar{\rho}$ for three representative cases: a) $\gamma = 0.003$, $\ell = 0.75h$; b) $\gamma = 0.0001$, $\ell = 0.75h$; c) $\gamma = 0.0001$, $\ell = 1.5h$ ($h = 0.01$, $\Delta t_{\max} = T_{\mathrm{exact}}/500$).

7.2. Single inclusion in a constrained domain

In this example, a 2D square domain with a single evolving inclusion is considered. To ensure a non-trivial steady-state solution, the displacements are fully constrained on the boundary and a volumetric eigenstrain of the same value but

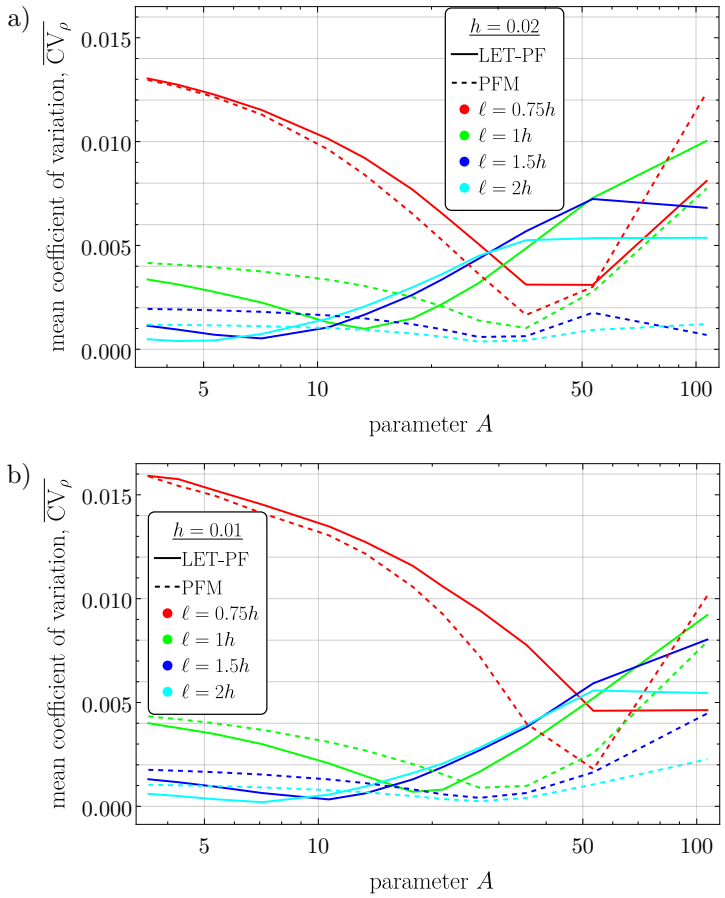

Fig. 7.11. Mean coefficient of variation of the inclusion radius $\overline{\mathrm{CV}_\rho}$, Eq. (7.5), for: a) $h = 0.02$ and b) $h = 0.01$ ($\Delta t_{\max} = T_{\mathrm{exact}}/500$).

with opposite signs is introduced in both phases, namely $\boldsymbol{\varepsilon}_2^{\mathrm{t}} = -\boldsymbol{\varepsilon}_1^{\mathrm{t}} = \epsilon \boldsymbol{I}$ with $\epsilon = 0.1$. Accordingly, considering a viscous evolution towards the minimum of the elastic strain energy, a steady-state solution is expected with the overall volume fraction of both phases close to 0.5, because this leads to a null overall eigenstrain in the domain, thus effectively minimizing the total elastic strain energy (the chemical energy is not considered).

The dimensions of the domain are 1×1, the inclusion is initially located in the domain centre and its initial radius is $\rho_0 = 0.1$. Homogeneous elastic properties are assumed, specifically, Young's modulus $E = 1$ and Poisson's ratio $\nu = 0.25$. Further, the following interface parameters are assumed: the interfacial energy density $\gamma = 0.0003$, the effective mobility $\hat{m} = 1$, and the interface thickness parameter $\ell = 1.5h$.

Preliminary computations have been performed on the mesh of 100×100 elements. Figure 7.12 illustrates the evolution of the inclusion shape for both methods, starting from $t = 0$ and ending in a steady state at $t \to \infty$ (a sufficiently large final time has been adopted). Discernible differences between LET-PF and PFM become evident almost instantaneously. The final shape of the inclusion is different, with the corners being more acute for PFM. Also, the evolution towards a square-like shape proceeds faster for PFM, compare the snapshots corresponding to $t = 15$. Moreover, for PFM, artefacts manifest in the corners of the domain at a relatively early stage, a phenomenon not observed for LET-PF. Finally, in the case of PFM, the interface thickness increases with respect to the theoretical one, which is prescribed at $t = 0$, while no visible difference in the interface thickness is observed for LET-PF.

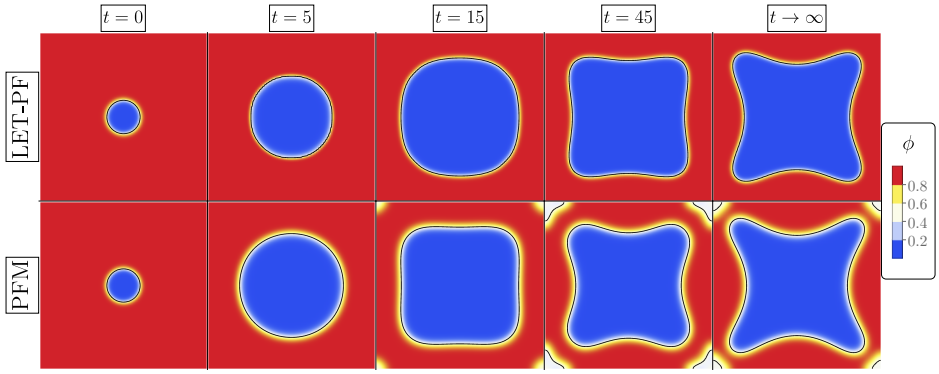

Fig. 7.12. Evolution of the inclusion within a constrained domain for LET-PF (top) and PFM (bottom) obtained for the mesh of 100×100 elements. The colour maps depict the order parameter ϕ. The black contours indicate the position of the $\phi = \frac{1}{2}$ level set.

To get a better insight, the computations have been performed for a range of mesh densities with $N \times N$ elements where $N \in \{26, 50, 100, 200, 400, 800, 1600\}$. Figure 7.13 shows the steady-state shapes for selected mesh densities (the results for the two finest meshes are omitted, as no differences are visible with further mesh refinement). Based on the results obtained, a clear advantage of LET-PF over PFM can be observed. For coarse meshes, PFM fails, yielding a trivial solution with $\phi = 0.5$ in the entire domain. This stands in contrast to LET-PF which produces qualitatively correct results already for the coarsest mesh. Secondly, while the final shape seems to converge to the same solution for both methods, the convergence is faster for LET-PF. This is also apparent in Fig. 7.14 which shows the total elastic strain energy Ψ_{el} and the total interfacial energy Ψ_{int} in the steady state as a function of mesh density.

To examine the evolution of shape quantitatively, the distance from the centre to the interface (level set $\phi = 0.5$), measured in the horizontal direction and

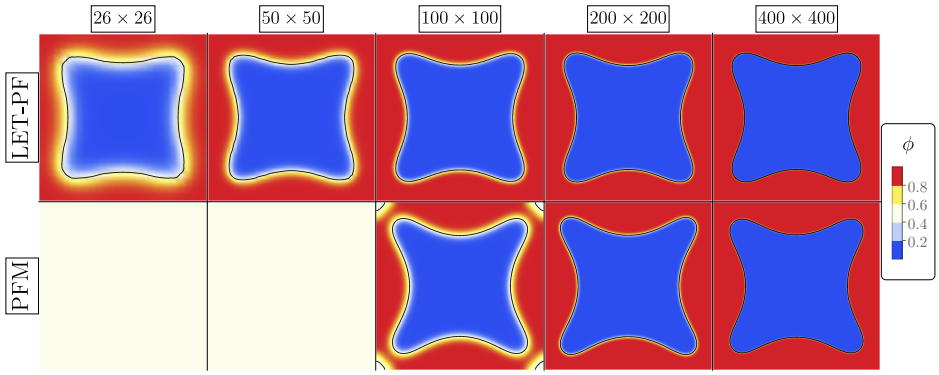

Fig. 7.13. Steady-state shapes for LET-PF (top) and PFM (bottom) as a function of mesh density (increasing from left to right).

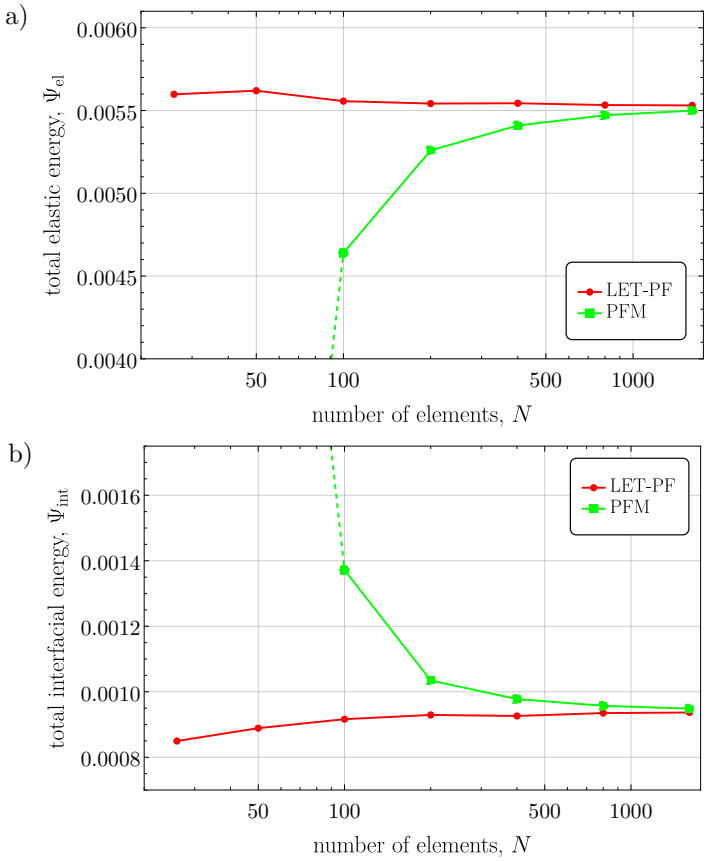

Fig. 7.14. Convergence of: a) the total elastic strain energy Ψ_{el} and b) the total interfacial energy Ψ_{int} with mesh refinement. The points corresponding to the trivial solution obtained for PFM for $N = 26$ and $N = 50$ are not included, the dashed lines show that these points lie well outside the plot range.

along the diagonal, is shown in Fig. 7.15 for three mesh densities. For the finest mesh ($N = 1600$), the results obtained for LET-PF and PFM are very close one to the other, which again suggests that both methods converge to the same solution. However, consistent with Fig. 7.14, the convergence rate is visibly different. For PFM, the difference between the results obtained for $N = 200$ and $N = 1600$ is significantly larger than in the case of LEF-PF. For the coarsest mesh ($N = 26$), a trivial solution is obtained for PFM, while LET-PF delivers a reasonably accurate solution.

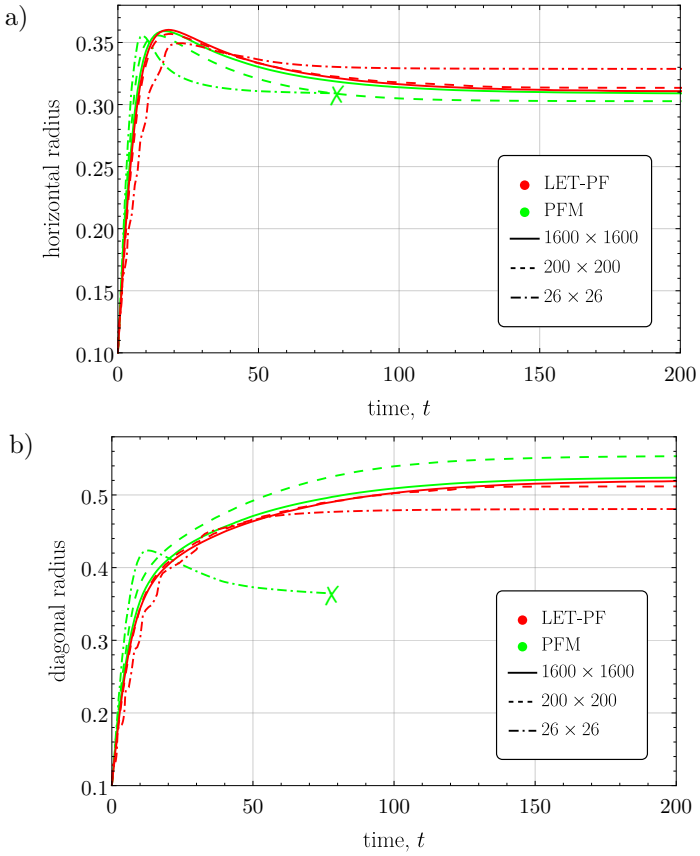

Fig. 7.15. Evolution of the inclusion size expressed by the distance from the centre to the propagating interface measured in the horizontal (a) and diagonal (b) directions, shown for selected mesh densities. Cross markers indicate the instant when the trivial solution is achieved for PFM with $\phi = 0.5$ in the entire domain.

7.3. Three inclusions in a constrained domain

As the last example, a problem similar to that of Section 7.2 is studied with the only difference that three inclusions are considered in the initial conditions.

The initial inclusion radii are 0.1, 0.15 and 0.2, and the corresponding positions of the inclusion centres are (0.25, 0.25), (0.75, 0.30) and (0.35, 0.75), respectively, for the origin of the coordinate system located in the lower-left corner of the domain. The remaining parameters of the problem are the same as in Section 7.2.

Figure 7.16 shows selected snapshots of the evolution process for four mesh densities. Consider first the case of the finest mesh of 400×400 elements. Here,

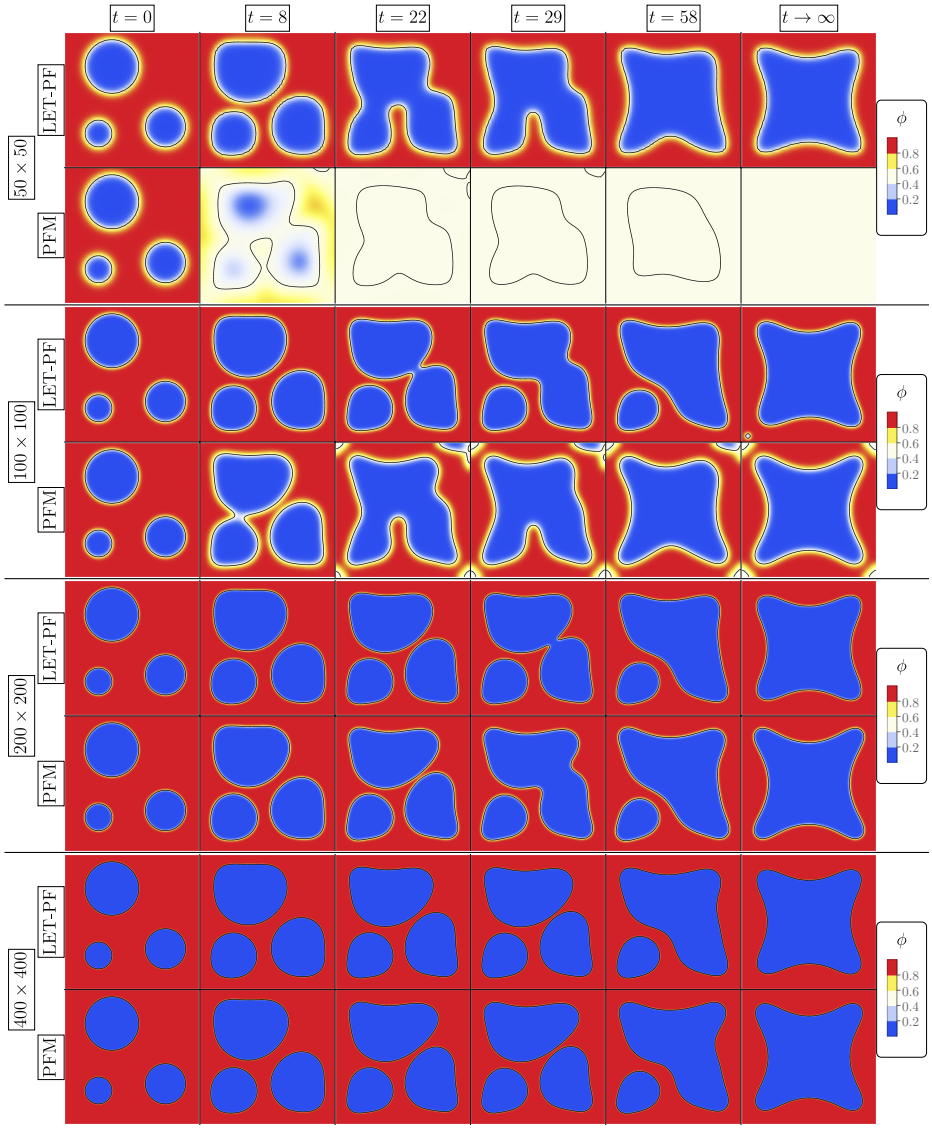

Fig. 7.16. Evolution of three inclusions within a constrained domain obtained for four mesh densities and for LET-PF (upper snapshots) and PFM (lower snapshots). The colour maps depict the order parameter ϕ. The black contours indicate the position of the $\phi = 0.5$ level set.

the evolution is very similar for LET-PF and PFM. At the beginning, all inclusions start to grow. Then two inclusions coalesce and grow further, while the third inclusion (that in the lower-left corner) shrinks and ultimately vanishes. In the case of LET-PF, this scenario is obtained also for two coarser meshes, although the two inclusions coalesce at an earlier stage (at $t = 29$ for $N = 200$ and at $t = 22$ for $N = 100$), and only for the coarsest mesh ($N = 50$) a different scenario is obtained in which all inclusions coalesce. However, in the case of PFM, the correct scenario is obtained for $N = 200$, even if the evolution proceeds then significantly faster (see the snapshot at $t = 29$). At the same time, an incorrect scenario is obtained for $N = 100$ (three inclusions coalesce), while for $N = 50$ the microstructure evolves towards the trivial solution, as in Section 7.2.

The final shapes correspond, in general, to those obtained for the single-inclusion problem in Section 7.2. Note that, for LET-PF and $N = 100$, the shrinking inclusion does not vanish completely, rather a small remnant inclusion persists in the steady state, see the lower-left corner of the domain. Also, the final shape obtained for LET-PF for $N = 50$ is not perfectly symmetric with the upper-right corner of the inclusion being somewhat more rounded than the other ones. Both effects suggest that LET-PF may be prone to mesh pinning, and this effect may require further attention in the future.

Nevertheless, the present numerical example confirms that LET-PF performs significantly better than PFM for the class of problems considered here, in particular, it is capable of capturing the correct evolution scenario for a coarser mesh.

7.4. Summary

A comprehensive set of numerical examples has been investigated, demonstrating that the proposed LET-PF method is, in certain cases, superior to the conventional phase-field method. The performance of the LET-PF method has been assessed in simulations involving different regimes of interest, corresponding to various contributions of both interfacial and elastic strain energies to the total thermodynamic driving force. The obtained results reveal that when the thermodynamic driving force primarily originates from the interfacial energy, both LET-PF and PFM methods show no fundamental differences. However, in cases where the thermodynamic driving force is mainly influenced by the elastic strain energy, the LET-PF method yields significantly more accurate results than PFM. Consequently, coarser meshes (along with a larger interface thickness) can be employed in LET-PF to achieve results of similar accuracy, thereby reducing computational costs.

8. Final remarks

8.1. Summary

A new finite-element approach for modelling both material and moving weak discontinuities has been developed. The formulation of the proposed technique has been presented in the thesis and the performance of the method has been demonstrated through numerous computational examples from the field of solid mechanics, involving both material and moving interface problems.

One of the features of the developed technique is that the discretization (finite-element mesh) is independent of the internal geometry of the modelled body so that the elements may be cut by the interface (i.e., a non-conforming mesh is used). To handle such a situation, a special treatment of such elements must be performed. To this end, the mechanics of laminated microstructures is employed, which is the foundation of the new method. These finite elements, where two phases are present, are replaced by the laminated ones which means that their behaviour is fully determined by the simple laminate, hence the name – *laminated element technique* (LET).

The content of the thesis is conceptually divided into two parts. The first one is devoted to the computational modelling of material weak discontinuities, while the second part covers the topics related to the modelling of moving weak discontinuities. In both parts, the respective formulation has been presented, followed by numerical experiments, the results of which have been compared with analytical solutions (whenever possible) and other existing computational methods.

The first part of the thesis serves as a prelude to the second part, which is the focal point of the dissertation. It focuses on modelling material interfaces, presenting the necessary equations that constitute the formulation of the method ready for direct implementation in the finite-element framework. This part of the work is concluded with a series of computational examples in the field of static problems of mechanics, demonstrating the performance of the developed approach.

The second part of the thesis, directly related to the title of the dissertation, focuses on the concerns related to the modelling of moving weak discontinuities. The method proposed in this part is the result of coupling the method formulated in the first part of the thesis with the popular and well-established phase-field

model. As before, the content of this part of the thesis consists of the formulation in a form ready for use within the finite-element framework. Additionally, a brief discussion on the new method and its comparison with other known methods in the literature is included. Extensive numerical analyses using quasi-static problems of solid mechanics conclude this part of the work.

8.1.1. Original contributions of the thesis

- Formulation and finite-element implementation of a new approach for computational modelling of material weak discontinuities (laminated element technique, LET).
- Verification of the performance of LET through simulations of numerous static problems in the field of solid mechanics and comparison of results with other alternative computational methods.
- Formulation and finite-element implementation of a new technique for computational modelling of moving weak discontinuities by coupling LET with a well-established phase-field model (LET-PF).
- Comparative analysis of LET-PF with the conventional phase-field method and with the analytical solutions (whenever possible) through numerical simulations of selected microstructure evolution problems.
- Demonstration of the superiority of LET-PF over the conventional phase-field method in certain cases.

The research results presented in this dissertation have also been published in peer-reviewed journals, see [34, 35].

8.2. Conclusions

The use of a non-matching mesh of finite elements offers several advantages over modelling with a conforming mesh. However, it comes with the trade-off of losing accuracy associated with the inaccurate representation of interface geometry. Therefore, the objective of LET has been to improve accuracy while simultaneously maintaining simplicity meaning that the implementation is carried out solely at the finite element level and no additional global degrees of freedom are added.

LET is general in the sense that any material model can be applied within each phase. The constitutive behaviour of each laminated element is determined by the closed-form, exact micro-to-macro transition relations for simple laminates. For nonlinear materials (e.g., plasticity, finite deformations), a system of nonlinear equations needs to be solved at each Gauss point. This makes the effective constitutive model within laminated elements somewhat more compli-

cated, but efficient computer implementation, including consistent linearization, is feasible, as demonstrated in the case of plasticity under finite deformations.

LET has been tested through numerical simulations of several solid mechanics problems involving material interfaces. The examples include both two- and three-dimensional cases, considering linear elasticity as well as hyperelastic and elasto-plastic constituents. The obtained results demonstrate the superiority of LET over two alternative simple approaches. Where possible, the results of the proposed method have been compared with those of a well-established and more sophisticated method, such as X-FEM. This comparison reveals that LET is unable to achieve the optimal convergence rate, in contrast to the X-FEM method.

However, the goal of formulating a new method for modelling material interfaces was not to compete with X-FEM. The proposed technique, while maintaining simplicity and ease of implementation, possesses the advantage of the ability to adapt to continuous changes in the position of the interface within a single finite element. This property of LET opens the possibility to generalize the method to the modelling of moving interfaces. To this end, the well-established phase-field method has been employed and coupled with LET, thus leading to a new approach, LET-PF.

The main assumption of the conventional phase-field method (PFM) is that the interface is treated in a diffuse manner and has some specified, finite thickness. This leads to both the associated interfacial energy and the transition region, where the change from one phase to another occurs, being smeared out within this diffuse interface. Although in the part related to modelling interfacial energy LET-PF does not fundamentally differ from conventional PFM, its main improvement over PFM pertains to modelling bulk energy. While in the conventional PFM the phases are mixed within the entire diffuse interface that spans several elements (at least 3–4, say), in LET-PF, the two phases are mixed only within a thin layer of laminated elements (of the thickness of one element) along the sharp interface. Consequently, this leads to a more precise representation of the sharp interface and, therefore, to an increase in results accuracy. The above property is the reason why LET-PF can be classified as a *hybrid diffuse–semisharp* approach.

The performance of LET-PF has been demonstrated through a comprehensive set of numerical examples. The obtained results, in certain cases, reveal a clear advantage over the conventional PFM. Significant differences in the results are particularly noticeable in regimes where the elastic strain energy contribution dominates (elasticity-driven evolution) – in such cases, LET-PF exhibits significantly higher accuracy compared to the conventional PFM. Consequently, coarser discretization (along with a larger interface thickness) can be applied in LET-PF to achieve results of similar accuracy, thereby reducing computational expense.

Overall, LET-PF appears to be a promising method for problems involving moving interfaces. Nevertheless, further research on the method should be undertaken to enhance its robustness and to test it across a wider range of problems. Possible extensions and improvements are discussed in the next section.

8.2.1. Future plans and developments

The results presented in this thesis appear to be satisfactory. In the part of the work related to modelling material weak discontinuities, the proposed method has been thoroughly investigated, and at present no areas have been identified where significant improvements could be made to the new computational approach. However, many issues related to modelling moving interfaces remain unexplored, and their development would make it possible to maximize the potential of the computational technique presented.

In the investigations of the performance of LET-PF, numerical examples have been limited to two-dimensional cases within linear elasticity. However, as demonstrated with LET in Chapter 6, the generalization of the method to three-dimensional cases is straightforward and does not require the development of additional significant procedures. Similarly, the consideration of finite deformations is straightforward because LET is general in terms of the material model used within each phase; therefore, LET-PF should easily handle the hyperelastic constituents.

In the assessment of the performance of LET-PF, the focus has been also limited to the viscous case of the kinetic law. As mentioned in Subsection 3.2.1, this is a rather common practice, and the application of other kinetic laws in phase-field modelling is relatively rare. However, it is one of the areas where a broader analysis could be ventured into, testing other kinetic laws, such as those where dissipation is rate-independent or of mixed-type (including both viscous and rate-independent types), and where exceeding the threshold value of the thermodynamic driving force is needed to initialize the interface evolution.

The improvement of LET presented in Appendix B and utilized in the numerical example in Section 6.4, was intended for consideration of more than one interface within a single finite element. However, it can also be readily accessible within LET-PF as well, where it can serve as a framework for modelling the evolution of microstructures composed of more than two phases. In such cases, the challenge may to be find, or even to invent an appropriate treatment to handle those finite elements where so-called triple junctions occur, i.e., points where three interfaces between the three phases meet.

When discussing the improvements and challenges facing the presented method, it is also important to mention the modelling of nucleation. LET-PF, in its current form, although capable of simulating the propagation, coalescence, and annihilation of interfaces, is not able to model nucleation, that is, the sponta-

neous formation of inclusions of a given phase, triggered by a small perturbation of the order parameter or additional noise (thermal fluctuation), e.g. [86,165,170], or by an inhomogeneous driving force exceeding the transformation threshold, e.g. [126, 161]. This is because in LET-PF, similar to X-FEM-based microstructure evolution modelling approaches, the mechanical contribution to the driving force for transformation is non-zero only when the interface actually exists and this requires a sufficiently large perturbation of the order parameter such that it passes the threshold of 0.5. Accordingly, the nuclei would have to be introduced explicitly, e.g., according to a suitable nucleation theory, as is the case of some phase-field models, e.g. [95, 96, 137].

Finally, it should be noted that LET-PF has been tested for a rather narrow class of problems. In Chapter 7, the scope is limited only to examples where the subproblem was mechanical. The phase-field method has a wide range of applications, and it is reasonable to expect that LET-PF will achieve similar success in other applications, such as heat transfer problems or optimization.

Appendix A. Other ways to calculate the elemental volume fraction

The way in which the volume fractions of the phases within a finite element are calculated is a key part of the LET (and subsequently LET-PF). As mentioned in Section 4.2, this component of the method can be replaced by any other suitable formulation.

In the early stages of research on the method proposed in this thesis, two approaches alternative to Eq. (4.5) were used in numerical simulations to calculate the volume fractions. These techniques, denoted as `VFC1` and `VFC2` and applicable only to two-dimensional quadrilateral elements, are characterized by a purely geometric approach, utilizing a simple approximation of the interface shape within a finite element, as illustrated in Fig. A.1.

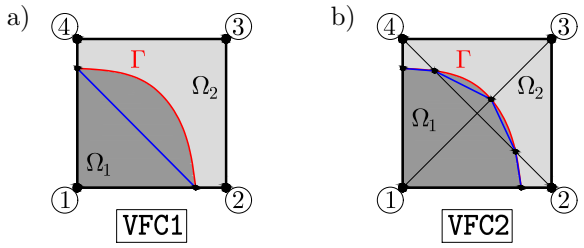

Fig. A.1. A conceptual sketch of the two simple approaches of calculating the elemental volume fraction: a) `VFC1` and b) `VFC2`. In both figures, the finite element is shown, where two subdomains, Ω_1 and Ω_2, are present, and the element nodes are numbered from 1 to 4. The figures show how the original shape of the interface Γ (solid red line) is approximated (solid blue line) in the given approach.

In the `VFC1` approach, see Fig. A.1a, intersection points of the interface are determined based on interpolation along the edges of the finite element. The straight line connecting these points serves as an approximation of the interface within that finite element. Assuming the presence of only one interface within the element, the calculation of the volume fractions involves computing the corresponding area of the triangle or trapezoid and relating it to the total area of the finite element. For more details, refer to Algorithm 1, which outlines a simple procedure for a reference square element with a side of unit length.

Algorithm 1
`VFC1[ ]`: procedure (type 1) for the volume fraction of the phase 2, $\eta^{(\omega)}$. Whenever the subscript i occurs, the expression should be calculated for $i \in \{1, 2, 3, 4\}$.

input: $\phi_i^{(\omega)}$
$\mathsf{a}_i \leftarrow \phi_i^{(\omega)} - \frac{1}{2}$
if $\forall_{i=1}^{4}(\mathsf{a}_i \geqslant 0)$ **then** ▷ element entirely in the phase 2
  $\eta^{(\omega)} \leftarrow 1$
else if $\forall_{i=1}^{4}(\mathsf{a}_i \leqslant 0)$ **then** ▷ element entirely in the phase 1
  $\eta^{(\omega)} \leftarrow 0$
else ▷ cut element
  $$\mathsf{s}_i \leftarrow \begin{cases} 0, & \mathsf{a}_i\mathsf{a}_{i+1} > 0 \\ \dfrac{\mathsf{a}_i}{\mathsf{a}_i - \mathsf{a}_{i+1}}, & \text{otherwise} \end{cases}$$
  if $\prod_{i=1}^{4} \mathsf{a}_i > 0$ **then** ▷ case when the interface cuts two opposite edges
    $\mathsf{sgn} \leftarrow \operatorname{sign} \mathsf{a}_1$
    $\{\mathsf{b}_1, \mathsf{b}_2\} \leftarrow \{\mathsf{s}_1 + \mathsf{s}_2, \mathsf{s}_3 + \mathsf{s}_4\}$
    $\mathsf{vol} \leftarrow \frac{1}{2}\left(\mathsf{b}_1 + (1 - \mathsf{b}_2)\right)\mathsf{sgn}$ ▷ signed area of the unit height trapezoid
    $$\eta^{(\omega)} \leftarrow \begin{cases} \mathsf{vol}, & \mathsf{sgn} > 0 \\ \mathsf{vol} + 1, & \text{otherwise} \end{cases}$$
  else ▷ case when the interface cuts two neighbouring edges
    $$\mathsf{r}_i \leftarrow \begin{cases} 0, & \mathsf{a}_i\mathsf{a}_{i-1} > 0 \\ \dfrac{\mathsf{a}_i}{\mathsf{a}_i - \mathsf{a}_{i-1}}, & \text{otherwise} \end{cases}$$
    $\mathsf{q}_i \leftarrow \frac{1}{2}\mathsf{s}_i\mathsf{r}_i \operatorname{sign} \mathsf{a}_i$ ▷ signed area of the triangle
    $\mathsf{vol} \leftarrow \sum_{i=1}^{4} \mathsf{q}_i$
    $$\eta^{(\omega)} \leftarrow \begin{cases} 1/2, & \mathsf{vol} = 0 \\ \mathsf{vol}, & \mathsf{vol} > 0 \\ \mathsf{vol} + 1, & \text{otherwise} \end{cases}$$
  end if
end if
return: $\eta^{(\omega)}$

The `VFC2` approach, see Fig. A.1b, is a slightly more sophisticated version of the `VFC1` approach. Using standard bilinear shape functions for the quadrilateral element, the approximated value of the level-set function ϕ is calculated at the element centre as the mean value of nodal values. Using the diagonals, the original element is divided into four triangular subelements, within which the interface is approximated by straight lines. These lines connect the intersection points of the interface with the edges of the original element and its diagonals. Subsequently, the volume fractions are independently computed in each

Algorithm 2

`VFC2[ ]`: procedure (type 2) for the volume fraction of the phase 2, $\eta^{(\omega)}$. Whenever the subscript i occurs, the expression should be calculated for $i \in \{1,2,3,4\}$.

input: $\phi_i^{(\omega)}$

$\mathsf{a}_i \leftarrow \phi(\omega)_i - \frac{1}{2}$

if $\forall_{i=1}^{4}(\mathsf{a}_i \geqslant 0)$ **then** ▷ element entirely in the phase 2

$\eta^{(\omega)} \leftarrow 1$

else if $\forall_{i=1}^{4}(\mathsf{a}_i \leqslant 0)$ **then** ▷ element entirely in the phase 1

$\eta^{(\omega)} \leftarrow 0$

else ▷ cut element

$\mathsf{a}_0 \leftarrow \frac{1}{4}\sum_{i=1}^{4}\mathsf{a}_i$ ▷ app. value of the level-set function in the element centre

$$\mathsf{s}_i \leftarrow \begin{cases} 0, & \mathsf{a}_i\mathsf{a}_{i+1} > 0 \\ \dfrac{\mathsf{a}_i}{\mathsf{a}_i - \mathsf{a}_{i+1}}, & \text{otherwise} \end{cases}$$

if $\mathsf{a}_0 = 0$ **then** ▷ interface cuts through the element centre

$$\mathsf{q}_i \leftarrow \begin{cases} \frac{1}{4}\mathsf{s}_i \operatorname{sign}\mathsf{a}_i, & \mathsf{s}_i \neq 0 \\ \begin{cases} \frac{1}{4}\operatorname{sign}\mathsf{a}_{i+1}, & \mathsf{a}_i = 0, \\ \frac{1}{4}\operatorname{sign}\mathsf{a}_i, & \text{otherwise}, \end{cases} & \text{otherwise} \end{cases}$$

$$\mathsf{vol}_i \leftarrow \begin{cases} \mathsf{q}_i + \frac{1}{4}, & \mathsf{q}_i < 0 \\ \mathsf{q}_i, & \text{otherwise} \end{cases}$$

$\eta^{(\omega)} \leftarrow \sum_{i=1}^{4}\mathsf{vol}_i$

else

$$\mathsf{r}_i \leftarrow \begin{cases} 0, & \mathsf{a}_i\mathsf{a}_{i-1} > 0, \\ \dfrac{\mathsf{a}_i}{\mathsf{a}_i - \mathsf{a}_{i-1}}, & \text{otherwise}, \end{cases} \qquad \mathsf{d}_i \leftarrow \begin{cases} 0, & \mathsf{a}_i\mathsf{a}_0 > 0 \\ \dfrac{\mathsf{a}_i}{\mathsf{a}_i - \mathsf{a}_0}, & \text{otherwise} \end{cases}$$

$$\mathsf{p}_i \leftarrow \begin{cases} 0, & \mathsf{a}_i\mathsf{a}_0 > 0 \\ \dfrac{\mathsf{a}_0}{\mathsf{a}_0 - \mathsf{a}_i}, & \text{otherwise} \end{cases}$$

$\{\mathsf{t}_{i1}, \mathsf{t}_{i2}, \mathsf{t}_{i3}\} \leftarrow \{\frac{1}{4}\mathsf{s}_i\mathsf{d}_i \operatorname{sign}\mathsf{a}_i,\ \frac{1}{4}\mathsf{r}_{i+1}\mathsf{d}_{i+1}\operatorname{sign}\mathsf{a}_{i+1},\ \frac{1}{4}\mathsf{p}_i\mathsf{p}_{i+1}\operatorname{sign}\mathsf{a}_0\}$

$\mathsf{q}_i \leftarrow \sum_{i=1}^{3}\mathsf{t}_{ij}$

$$\mathsf{vol}_i \leftarrow \begin{cases} 1/4, & (\mathsf{a}_i \geqslant 0) \wedge (\mathsf{a}_{i+1} \geqslant 0) \wedge (\mathsf{a}_0 \geqslant 0) \\ 0, & (\mathsf{a}_i \leqslant 0) \wedge (\mathsf{a}_{i+1} \leqslant 0) \wedge (\mathsf{a}_0 \leqslant 0) \\ \max\mathsf{t}_{ij}, & \max\mathsf{t}_{ij} \cdot \min\mathsf{t}_{ij} \neq 0 \\ \mathsf{q}_i, & \mathsf{q}_i > 0 \\ \mathsf{q}_i + 1/4, & \text{otherwise} \end{cases}$$

$\eta^{(\omega)} \leftarrow \sum_{i=1}^{4}\mathsf{vol}_i$

end if

end if

return: $\eta^{(\omega)}$

subelement. Finally, the overall elemental volume fraction is obtained as the weighted sum of the subelemental volume fractions. This procedure is detailed in Algorithm 2.

It should be emphasized that the above-mentioned procedures are susceptible to cases of highly complex interface shapes within a given finite element. These may occur in situations with a very coarse mesh, where the size of a single finite element is relatively large, and the internal geometry exhibits significant variability. However, with mesh refinement, the shape of the interface within a finite element converges to a straight line, and for such cases, the above approaches, `VFC1` and `VFC2`, operate then effectively.

As mentioned, the presented two alternative approaches to calculating volume fractions apply to two-dimensional cases only. Although the procedures outlined in Algorithms 1 and 2 are not overly complicated, ensuring their reliability (by accounting for all exceptions) required a considerable amount of time and effort. Therefore, the generalization of these procedures to three-dimensional cases has not been pursued, and the method of calculating volume fractions has been replaced by a much simpler Eq. (4.5), which directly generalizes to 3D cases.

Appendix B. LET with multiple level-set functions

As discussed in Remark 4.1, the LET formulation presented in Section 4.2 is applicable when only one interface is present within the finite element. In practice, this situation is rather common than rare, as the simplest solution to this problem is to refine the mesh in the vicinity of the two interfaces that are close to each other. However, LET can be easily generalized to cases where more than one interface is present within the finite element. To this end, additional level-set functions are introduced,

$$\phi_\alpha : \Omega \subset \mathbb{R}^n \to \mathbb{R}, \tag{B.1}$$

one for each α-th separate interface,

$$\Gamma_\alpha = \{\boldsymbol{X} \in \Omega \subset \mathbb{R}^n \mid \phi_\alpha(\boldsymbol{X}) = 0.5\}. \tag{B.2}$$

Then, the finite-element approximation of each of these fields is given,

$$\phi_\alpha^h = \sum_k N_k^{(\phi)} \phi_{\alpha,k}, \tag{B.3}$$

where $N_k^{(\phi)}$ are the usual finite-element basis functions and $\phi_{\alpha,k}$ are the nodal values. For each individual interface Γ_α, the elemental volume fraction can be calculated,

$$\eta_\alpha^{(\omega)} = \frac{\sum_{k=1}^{N_\mathrm{n}} \left\langle \phi_{\alpha,k}^{(\omega)} - \frac{1}{2} \right\rangle}{\sum_{k=1}^{N_\mathrm{n}} \left| \phi_{\alpha,k}^{(\omega)} - \frac{1}{2} \right|}, \tag{B.4}$$

where $\phi_{\alpha,k}^{(\omega)}$ are the nodal values of the α-th level-set function ϕ in the element, N_n is the number of nodes in the element, and $\langle \square \rangle$ denotes the Macaulay brackets. If for each level-set function ϕ_α values greater than 0.5 correspond to the same subdomain, the overall volume fraction of that subdomain within the finite element can be thus obtained as a sum of the partial elemental volume fractions $\eta_\alpha^{(\omega)}$,

$$\eta^{(\omega)} = \sum_{\alpha=1}^{N_{LS}} \eta_\alpha^{(\omega)}, \tag{B.5}$$

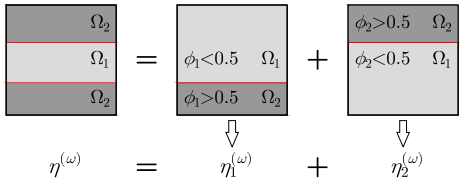

Fig. B.1. A conceptual scheme presenting the procedure to calculate the volume fraction within the finite element where two interfaces are present. It is worth noticing that it is crucial to choose the proper subdomain that is represented by the values of the level-set functions greater than 0.5 – if in the above example, the subdomain Ω_1 was represented by the values of ϕ_α greater than 0.5, the overall volume fraction would be greater than 1.

where N_{LS} is the number of level-set functions used. The volume fraction obtained in such a way may be then applied instead of formula (4.5) in the formulation of LET. The idea of this procedure is simply presented in Fig. B.1.

In the case of more than one interface present within the finite element, the unit normal vector in Eq. (4.6) can be replaced by the overall interface orientation. The calculation of this is a little bit more complicated than in the case of the overall volume fraction, but still very simple. The unit normal vector for each individual level-set function ϕ_α^h is computed according to the formula (4.6). Subsequently, the weighted sum of these vectors gives the overall interface orientation $\boldsymbol{N}^{(\omega)}$, see details in Algorithm 3.

Algorithm 3

`N_avg[ ]`: procedure returning the overall interface orientation, $\boldsymbol{N}^{(\omega)}$, within the finite element.

input: $\phi_\alpha^h,\ \eta_\alpha^{(\omega)}$

$$\boldsymbol{N}_\alpha^{(\omega)} \leftarrow \frac{\nabla\phi_\alpha^h(\boldsymbol{X}_0^{(\omega)})}{\|\nabla\phi_\alpha^h(\boldsymbol{X}_0^{(\omega)})\|}$$

$$\mathsf{mx} \leftarrow \arg\max_\alpha \eta_\alpha^{(\omega)}$$

$$\left\{\eta_{\max}^{(\omega)},\ \boldsymbol{N}_{\max}^{(\omega)}\right\} \leftarrow \left\{\eta_\alpha^{(\omega)},\ \boldsymbol{N}_\alpha^{(\omega)}\right\}\Big|_{\alpha=\mathsf{mx}}$$

$$\boldsymbol{N}_{\alpha,\mathrm{mod}}^{(\omega)} \leftarrow \begin{cases} \boldsymbol{N}_\alpha^{(\omega)}, & \boldsymbol{N}_\alpha^{(\omega)} \cdot \boldsymbol{N}_{\max}^{(\omega)} \geqslant 0 \\ -\boldsymbol{N}_\alpha^{(\omega)}, & \text{otherwise} \end{cases}$$

$$\boldsymbol{N}^{(\omega)} \leftarrow \frac{\sum_\alpha \eta_\alpha^{(\omega)} \boldsymbol{N}_{\alpha,\mathrm{mod}}^{(\omega)}}{\left\|\sum_\alpha \eta_\alpha^{(\omega)} \boldsymbol{N}_{\alpha,\mathrm{mod}}^{(\omega)}\right\|}$$

return: $\boldsymbol{N}^{(\omega)}$

These two procedures enabled the use of coarser meshes in the woven-cell problem presented in Section 6.4.

Appendix C. Incremental computational scheme for an elastic-plastic simple laminate*

In this appendix, the case of a simple laminate composed of two elastic-plastic materials is discussed. As discussed below, the corresponding computational model involves a nested iterative-subiterative Newton scheme. Its consistent linearization is crucial so that the Newton method can be effectively used on the structural level. In this work, this is achieved by using the automatic differentiation (AD) technique that is available in *AceGen* [76,78], and below the compact AD-based notation introduced in [76] is used.

The incremental constitutive equations of finite-strain plasticity are rather standard [138], and the details are omitted here. The specific AD-based formulation of elastoplasticity which is adopted here follows that developed in [76], see also [77,78]. On the other hand, the treatment of the laminated microstructure is based on that developed in [129] for the incremental Mori–Tanaka scheme (with due differences). The corresponding AD-based formulation is provided below in the form of a pseudocode with only short comments, while for the details the reader is referred to [129].

The AD-based notation employed in the pseudocodes below uses a special notation to denote the computational derivative, i.e., the derivative evaluated by AD. The computational derivative is denoted by $\hat{\delta} f / \hat{\delta} \mathbf{A}$, where f is a function defined by an algorithm (or computer program) in terms of independent variables collected in vector $\mathbf{A}$. The actual dependencies present in the algorithm can be overridden or modified by introducing the so-called AD exceptions that are denoted by a vertical bar following the derivative with additional specifications in the subscript. The details can be found in [76, 78].

Adopting the finite-strain framework, the elastic strain energy of phase i is expressed as a function of the deformation gradient $\boldsymbol{F}_i = \boldsymbol{F}_i^{n+1}$ and the vector $\mathbf{h}_i = \mathbf{h}_i^{n+1}$ of internal (history) variables at the current time step $t = t_{n+1}$,

$$W_i = W_i(\boldsymbol{F}_i, \mathbf{h}_i), \tag{C.1}$$

*The content of this appendix has been entirely excerpted from the article of Dobrzański *et al.* [35]. Minor modifications may have been applied to the text.

and the Piola stress $\boldsymbol{P}_i = \boldsymbol{P}_i^{n+1}$ is thus given by

$$\boldsymbol{P}_i = \frac{\partial W_i(\boldsymbol{F}_i, \mathbf{h}_i)}{\partial \boldsymbol{F}_i}. \tag{C.2}$$

Here and below, the superscript $n+1$ denoting the quantities at t_{n+1} is omitted to make the notation more compact. Time-discrete evolution of the internal variables $\mathbf{h}_i$ is governed by a set of nonlinear equations written symbolically in the residual form as

$$\mathbf{Q}_i(\boldsymbol{F}_i, \mathbf{h}_i, \mathbf{h}_i^n) = \mathbf{0}, \tag{C.3}$$

where $\mathbf{h}_i^n$ denotes the known internal variables at the previous time step $t = t_n$. In computational plasticity, the incremental equations of elastoplasticity are usually solved using the return-mapping algorithm, which leads to the *state update algorithm* that is outlined in Algorithm 4 using the AD-based notation. In this algorithm, the local problem (C.3) is solved iteratively using the Newton method,

Algorithm 4
`StateUpdate[ ]`: state update algorithm for phase i

input: $\boldsymbol{F}_i$, $\mathbf{h}_i^n$
$\phi_i^{\text{trial}} \leftarrow \phi_i(\boldsymbol{F}_i, \mathbf{h}_i^n)$
if $\phi_i^{\text{trial}} < 0$ **then**
  $\mathbf{h}_i \leftarrow \mathbf{h}_i^n$
  $\mathbf{G}_i \leftarrow \mathbf{0}$
else
  $\mathbf{h}_i \leftarrow \mathbf{h}_i^n$
  repeat
    $\mathbf{A}_i \leftarrow \dfrac{\hat{\delta}\mathbf{Q}_i\,(\boldsymbol{F}_i, \mathbf{h}_i, \mathbf{h}_i^n)}{\hat{\delta}\mathbf{h}_i}$ ▷ tangent matrix, $\mathbf{A}_i = \dfrac{\partial \mathbf{Q}_i}{\partial \mathbf{h}_i}$
    $\Delta\mathbf{h}_i \leftarrow -\mathbf{A}_i^{-1}\mathbf{Q}_i$
    $\mathbf{h}_i \leftarrow \mathbf{h}_i + \Delta\mathbf{h}_i$
  until $\|\Delta\mathbf{h}_i\| \le tol$
  $\mathbf{G}_i \leftarrow -\mathbf{A}_i^{-1}\, \dfrac{\hat{\delta}\mathbf{Q}_i}{\hat{\delta}\boldsymbol{F}_i}\bigg|_{\mathbf{h}_i=\text{const}}$ ▷ $\mathbf{G}_i = \dfrac{\partial \mathbf{h}_i}{\partial \boldsymbol{F}_i}$
end if
$\mathbf{h}_i \leftarrow \mathbf{h}_i\big|_{\frac{\mathrm{D}\mathbf{h}_i}{\mathrm{D}\boldsymbol{F}_i}=\mathbf{G}_i}$ ▷ introduce the implicit dependence of $\mathbf{h}_i$ on $\boldsymbol{F}_i$
$\boldsymbol{P}_i \leftarrow \dfrac{\hat{\delta}W_i(\boldsymbol{F}_i, \mathbf{h}_i)}{\hat{\delta}\boldsymbol{F}_i}\bigg|_{\mathbf{h}_i=\text{const}}$ ▷ AD exception ensures that $\boldsymbol{P}_i$ is computed correctly
return: $\mathbf{h}_i$, $\boldsymbol{P}_i$, $\mathbf{G}_i$

and the derivative of the implicit dependence of the solution $\mathbf{h}_i$ on $\boldsymbol{F}_i$ (denoted by $\mathbf{G}_i$ in Algorithm 4) is computed in the standard manner [76, 102],

$$\frac{\partial \mathbf{h}_i}{\partial \boldsymbol{F}_i} = -\left(\frac{\partial \mathbf{Q}_i}{\partial \mathbf{h}_i}\right)^{-1} \frac{\partial \mathbf{Q}_i}{\partial \boldsymbol{F}_i}. \tag{C.4}$$

The specific constitutive functions of the finite-strain J_2 plasticity model used in this work, see Section 6.5, are summarized in Box 1, see the formulation I-C-C-b in Box 1 in [77]. Box 1 provides also the corresponding definitions of the vector of internal variables $\mathbf{h}_i$ and of the local residual $\mathbf{Q}_i$. For brevity, the subscript i is omitted in Box 1.

Box 1: Constitutive equations of finite-strain J_2 plasticity with isotropic hardening. Phase index i is omitted for brevity.

Given: $\boldsymbol{F}, \boldsymbol{C}_{\mathrm{p},n}^{-1}, \gamma_n$ Find: $\boldsymbol{C}_{\mathrm{p}}^{-1}, \gamma$	
$\boldsymbol{b}_{\mathrm{e}} = \boldsymbol{F}\boldsymbol{C}_{\mathrm{p}}^{-1}\boldsymbol{F}^{\mathrm{T}}$	
$I_1 = tr\boldsymbol{b}_{\mathrm{e}}, \quad I_3 = \det \boldsymbol{b}_{\mathrm{e}}$	
$W = \frac{1}{2}\mu\,(I_1 - 3 - \log I_3) + \frac{1}{4}\lambda\,(I_3 - 1 - \log I_3)$	
$\boldsymbol{\tau} = 2\boldsymbol{b}_{\mathrm{e}}\dfrac{\partial W}{\partial \boldsymbol{b}_{\mathrm{e}}}$	▷ automation: $\boldsymbol{\tau} \leftarrow 2\boldsymbol{b}_{\mathrm{e}}\dfrac{\hat{\delta} W_{\mathrm{e}}}{\hat{\delta}\boldsymbol{b}_{\mathrm{e}}}$
$\boldsymbol{\tau}' = \boldsymbol{\tau} - \frac{1}{3}\,(tr\boldsymbol{\tau})\,\boldsymbol{I}$	
$\phi = \sqrt{\frac{3}{2}\boldsymbol{\tau}' \cdot \boldsymbol{\tau}'} - \sigma_{\mathrm{y}}(\gamma)$	
$\boldsymbol{n} = \dfrac{\partial \phi}{\partial \boldsymbol{\tau}}$	▷ automation: $\boldsymbol{n} \leftarrow \dfrac{\hat{\delta}\phi}{\hat{\delta}\boldsymbol{\tau}}$
$\mathfrak{Z} = \boldsymbol{F}\boldsymbol{C}_{\mathrm{p}}^{-1} - \exp\left(-2\,(\gamma - \gamma_n)\,\boldsymbol{n}\right)\boldsymbol{F}\boldsymbol{C}_{\mathrm{p},n}^{-1}$	
$\mathbf{h} = \left\{C_{\mathrm{p},11}^{-1} - 1, C_{\mathrm{p},22}^{-1} - 1, C_{\mathrm{p},33}^{-1} - 1, C_{\mathrm{p},23}^{-1}, C_{\mathrm{p},13}^{-1}, C_{\mathrm{p},12}^{-1}, \gamma\right\}$	
$\mathbf{Q} = \{\mathfrak{Z}_{11}, \mathfrak{Z}_{22}, \mathfrak{Z}_{33}, \mathfrak{Z}_{23}, \mathfrak{Z}_{13}, \mathfrak{Z}_{12}, \phi\}$	

Consider now a simple laminate in which both phases are governed by an elastic-plastic material model. Expressing the local deformation gradients in terms of $\bar{\boldsymbol{F}}$ and $\boldsymbol{c}$, as in Eq. (3.69), the macroscopic elastic strain energy $\bar{W} = \langle W \rangle$ reads

$$\bar{W}(\bar{\boldsymbol{F}}, \boldsymbol{c}, \mathbf{h}_1, \mathbf{h}_2) = (1-\eta) W_1(\boldsymbol{F}_1, \mathbf{h}_1) + \eta W_2(\boldsymbol{F}_2, \mathbf{h}_2), \tag{C.5}$$

and the macroscopic stress is obtained as

$$\bar{\boldsymbol{P}} = \frac{\partial \bar{W}(\bar{\boldsymbol{F}}, \boldsymbol{c}, \mathbf{h}_1, \mathbf{h}_2)}{\partial \bar{\boldsymbol{F}}} = (1-\eta)\frac{\partial W_1}{\partial \boldsymbol{F}_1}\frac{\partial \boldsymbol{F}_1}{\partial \bar{\boldsymbol{F}}} + \eta \frac{\partial W_2}{\partial \boldsymbol{F}_2}\frac{\partial \boldsymbol{F}_2}{\partial \bar{\boldsymbol{F}}} = (1-\eta)\boldsymbol{P}_1 + \eta \boldsymbol{P}_2. \tag{C.6}$$

The unknown vector $\boldsymbol{c}$ is obtained by solving, using the Newton method, the compatibility condition (3.4) written here in the residual form as

$$\mathbf{R}(\bar{\boldsymbol{F}}, \boldsymbol{c}, \mathbf{h}_1, \mathbf{h}_2) = (\boldsymbol{P}_2 - \boldsymbol{P}_1)\boldsymbol{N} = \boldsymbol{0}, \tag{C.7}$$

where the internal variables $\mathbf{h}_i$ depend on $\boldsymbol{c}$ through $\boldsymbol{F}_i$, thus $\mathbf{h}_i = \mathbf{h}_i(\boldsymbol{F}_i(\bar{\boldsymbol{F}}, \boldsymbol{c}))$, and this dependence must be taken into account when the residual $\mathbf{R}$ is linearized. The complete computational scheme is summarized in Algorithm 5, which in-

Algorithm 5
AD-based formulation of the incremental scheme for an elasto-plastic two-phase composite

input: $\bar{\boldsymbol{F}}$, $\boldsymbol{c}^n$, $\mathbf{h}_1^n$, $\mathbf{h}_2^n$
$\boldsymbol{c} \leftarrow \boldsymbol{c}^n$
repeat
  $\boldsymbol{F}_1 \leftarrow \bar{\boldsymbol{F}} - \eta \boldsymbol{c} \otimes \boldsymbol{N}$
  $\boldsymbol{F}_2 \leftarrow \bar{\boldsymbol{F}} + (1-\eta) \boldsymbol{c} \otimes \boldsymbol{N}$
  $\{\mathbf{h}_1, \boldsymbol{P}_1, \mathbf{G}_1\} \leftarrow \texttt{StateUpdate}\,[\boldsymbol{F}_1, \mathbf{h}_1^n]$
  $\{\mathbf{h}_2, \boldsymbol{P}_2, \mathbf{G}_2\} \leftarrow \texttt{StateUpdate}\,[\boldsymbol{F}_2, \mathbf{h}_2^n]$
  $\mathbf{R} \leftarrow (\boldsymbol{P}_2 - \boldsymbol{P}_1)\,\boldsymbol{N}$
  $\mathbf{B} \leftarrow \dfrac{\hat{\delta}\mathbf{R}}{\hat{\delta}\boldsymbol{c}}$ ▷ tangent matrix, $\mathbf{B} = \dfrac{\partial \mathbf{R}}{\partial \boldsymbol{c}}$
  $\Delta \boldsymbol{c} \leftarrow -\mathbf{B}^{-1}\mathbf{R}$
  $\boldsymbol{c} \leftarrow \boldsymbol{c} + \Delta \boldsymbol{c}$
until $\|\Delta \boldsymbol{c}\| \leq tol$
$\boldsymbol{c} \leftarrow \boldsymbol{c}\Big|_{\frac{\mathrm{D}\boldsymbol{c}}{\mathrm{D}\bar{\boldsymbol{F}}} = -\mathbf{B}^{-1}\frac{\hat{\delta}\mathbf{R}}{\hat{\delta}\bar{\boldsymbol{F}}}\big|_{\boldsymbol{c}=\mathrm{const}}}$
$\boldsymbol{F}_1 \leftarrow \bar{\boldsymbol{F}} - \eta \boldsymbol{c} \otimes \boldsymbol{N}$
$\boldsymbol{F}_2 \leftarrow \bar{\boldsymbol{F}} + (1-\eta) \boldsymbol{c} \otimes \boldsymbol{N}$
$\mathbf{h}_1 \leftarrow \mathbf{h}_1\Big|_{\frac{\mathrm{D}\mathbf{h}_1}{\mathrm{D}\boldsymbol{F}_1} = \mathbf{G}_1}$ ▷ introduce the implicit dependence of $\mathbf{h}_1$ on $\boldsymbol{F}_1$
$\mathbf{h}_2 \leftarrow \mathbf{h}_2\Big|_{\frac{\mathrm{D}\mathbf{h}_2}{\mathrm{D}\boldsymbol{F}_2} = \mathbf{G}_2}$ ▷ introduce the implicit dependence of $\mathbf{h}_2$ on $\boldsymbol{F}_2$
$\bar{W} \leftarrow (1-\eta)\, W_1(\boldsymbol{F}_1, \mathbf{h}_1) + \eta W_2(\boldsymbol{F}_2, \mathbf{h}_2)$
$\bar{\boldsymbol{P}} \leftarrow \dfrac{\hat{\delta}\bar{W}}{\hat{\delta}\bar{\boldsymbol{F}}}\Big|_{\boldsymbol{c}=\mathrm{const},\, \mathbf{h}_1=\mathrm{const},\, \mathbf{h}_2=\mathrm{const}}$ ▷ AD exception ensures that $\bar{\boldsymbol{P}}$ is computed correctly
$\bar{\mathbb{L}}^{\mathrm{alg}} \leftarrow \dfrac{\hat{\delta}\bar{\boldsymbol{P}}}{\hat{\delta}\bar{\boldsymbol{F}}}$
return: $\boldsymbol{c}$, $\bar{\boldsymbol{P}}$, $\bar{\mathbb{L}}^{\mathrm{alg}}$, $\mathbf{h}_1$, $\mathbf{h}_2$

cludes consistent linearization of the nested iterative-subiterative scheme. In particular, once the implicit dependencies are correctly identified and introduced into the code, the consistent overall tangent (denoted as $\bar{\mathbb{L}}^{\mathrm{alg}}$ in Algorithm 5) is obtained as the computational derivative $\hat{\delta}\bar{\boldsymbol{P}}/\hat{\delta}\bar{\boldsymbol{F}}$.

In practice, the iterative Newton scheme in Algorithm 5 can be enhanced by a line search technique which improves the robustness of the computational scheme. The related details are omitted here.

Appendix D. Regularization of the phase volume fraction in laminated elements*

As discussed in Section 5.4, the formula (4.5) for the phase volume fraction $\eta^{(\omega)}$ in the laminated elements is regularized according to Eq. (5.5). In this appendix, the effect of the regularization parameter ϕ_{reg} on the efficiency and accuracy of LET-PF is illustrated.

Additional simulations of the problem studied in Section 7.1 have thus been performed for three values of $\phi_{\text{reg}} \in \{0.001, 0.01, 0.1\}$ and for a wide range of model parameters. Figure D.1 presents representative results concerning the efficiency and robustness (quantified by the total number of time steps when $\Delta t_{\max} = T_{\text{exact}}$) and concerning the accuracy (expressed by the relative error, Eq. (7.3)). In the latter case, small time increments have been used ($\Delta t_{\max} = T_{\text{exact}}/500$) to isolate the error related to the regularization from that resulting from time integration. It has been observed that the dependence of both indicators on the interfacial energy γ is (approximately) monotonic, hence only the extreme values $\gamma = 0.0001$ and $\gamma = 0.003$ are included in Fig. D.1. The computations have been performed for the coarse mesh ($h = 0.02$) and for two representative values of the interface thickness parameter $\ell \in \{h, 1.5h\}$.

Figure D.1a shows that the number of time steps needed to complete the simulation decreases with increasing ϕ_{reg} for $\gamma = 0.0001$, and it only weakly depends on ϕ_{reg} for $\gamma = 0.003$. This confirms that the robustness and efficiency of the method increases with increasing ϕ_{reg}. Note that, in many cases, the simulations could not be completed without regularization, i.e., for $\phi_{\text{reg}} = 0$. Concerning the relative error, Fig. D.1b, the effect of ϕ_{reg} is weak, except one case ($\ell = 1.5h$, $\gamma = 0.0001$) when the error visibly increases with increasing ϕ_{reg}.

Concluding, the results presented above, as well as other results not reported here, do not give a definite answer on the choice of the regularization parameter. Higher values of ϕ_{reg} are, in general, beneficial for robustness and computational efficiency. At the same time, the effect on accuracy is in general weak.

*The content of this appendix has been entirely excerpted from the article of Dobrzański and Stupkiewicz [34]. Minor modifications may have been applied to the text and figures.

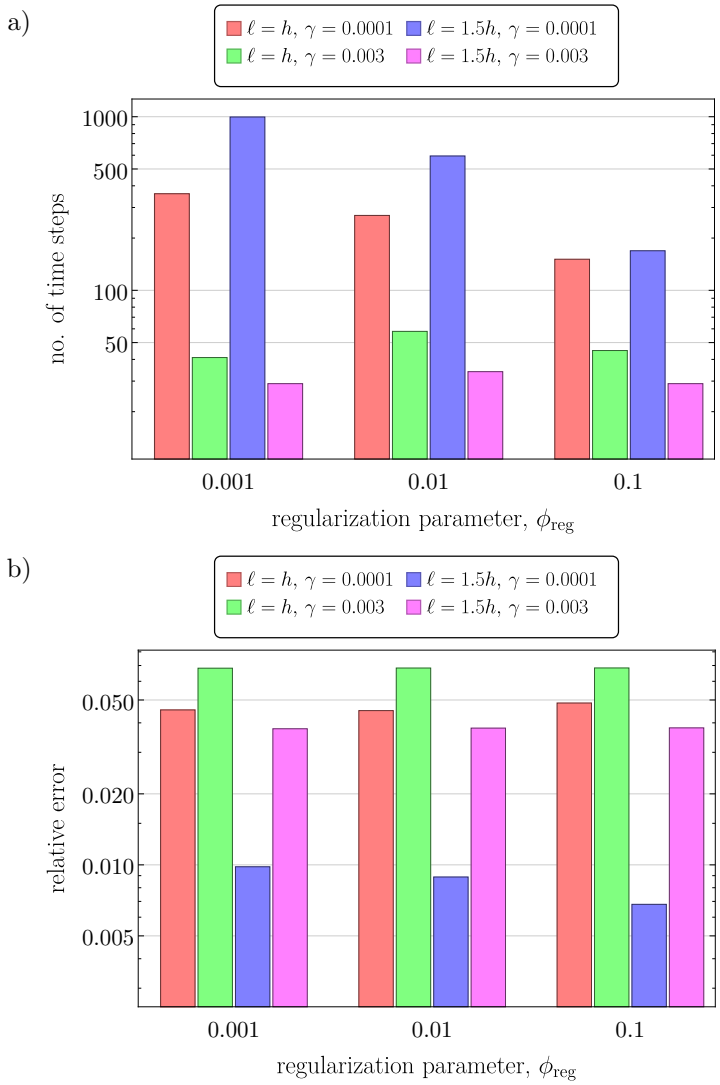

Fig. D.1. The effect of regularization parameter ϕ_{reg}: a) on the total number of time steps (for $\Delta t_{\max} = T_{\text{exact}}$), b) on the relative error (for $\Delta t_{\max} = T_{\text{exact}}/500$).

Appendix E. Analytical solution for the evolving circular inclusion

The Lamé solution of a thick-walled cylinder under internal pressure is a well-known classical problem in linear elasticity theory. It seeks to determine the stress state, deformation field, and displacement field of a plane circular disc of radius R_2 with a centrally located circular hole of radius R_1. The disc is assumed to be made of a weightless, homogeneous, and isotropic linear-elastic material, commonly referred to as Hooke's material. The object is subjected to a homogeneous normal load of magnitude q_1 at the inner surface and a homogeneous normal load of magnitude q_2 at the outer surface, see Fig. E.1a. Since it is an axis-symmetric problem, the circumferential displacement is zero, $u_\theta = 0$, and the radial displacement is expressed as

$$u_r(r) = \frac{q_2 R_2^2 - q_1 R_1^2}{2(\mu+\lambda)(R_2^2 - R_1^2)} r + \frac{R_1^2 R_2^2 (q_2 - q_1)}{2\mu(R_2^2 - R_1^2)} \frac{1}{r}, \tag{E.1}$$

where μ and λ are the Lamé constants.

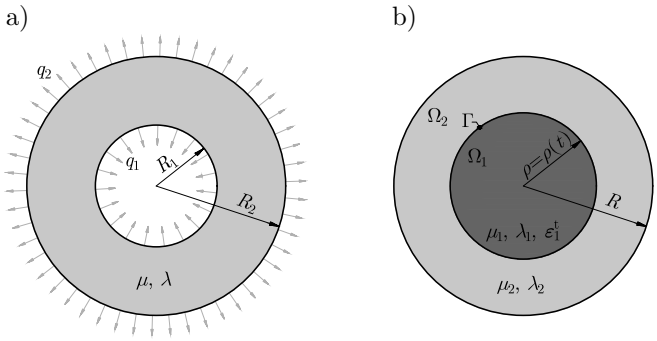

Fig. E.1. Scheme of the: a) classical Lamé problem, b) bimaterial Lamé problem with eigenstrain.

Using the general solution (E.1), the solution for bimaterial Lamé problem with eigenstrain can be obtained. Consider an unloaded, circular body of radius R occupying domain Ω that is divided into two subdomains – the circular inclusion Ω_1 of radius ρ and the matrix Ω_2, $\Omega = \Omega_1 \cup \Omega_2$, with homogeneous material

properties within these subdomains. The subdomains are separated by the interface denoted by Γ, $\Gamma = \Omega_1 \cap \Omega_2$. In the inclusion Ω_1 the volumetric eigenstrain is present, $\boldsymbol{\varepsilon}_1^{\mathrm{t}} = \epsilon \boldsymbol{I}$, where $\boldsymbol{I}$ is the second-order identity tensor, see Fig. E.1b. The elastic strain energy density function for the i-th phase takes the form

$$\psi_i^{\mathrm{el}} = \frac{1}{2}\lambda_i \left(\operatorname{tr} \boldsymbol{\varepsilon}^{\mathrm{el}}\right)^2 + \mu_i \operatorname{tr} \left(\boldsymbol{\varepsilon}^{\mathrm{el}}\right)^2, \tag{E.2}$$

where $\boldsymbol{\varepsilon}^{\mathrm{el}} = \boldsymbol{\varepsilon} - \boldsymbol{\varepsilon}_i^{\mathrm{t}}$ is the elastic small-strain tensor. Assuming the continuity of the displacement field $\boldsymbol{u}$ at the interface Γ, one can obtain the solution for such a problem,

$$u_r(r) = \begin{cases} (1-\epsilon^*)\epsilon\, r, & 0 \leqslant r \leqslant \rho, \\ \dfrac{(\lambda_1+\mu_1)\left(\mu_2 r^2 + (\lambda_2+\mu_2)\, R^2\right)\rho^2 \epsilon^* \epsilon}{\mu_2\,(\lambda_2+\mu_2)\,(R^2-\rho^2)\, r}, & \rho < r \leqslant R, \end{cases} \tag{E.3}$$

where μ_i, λ_i are the Lamé constants for i-th phase, and ϵ^* denotes the fraction of the eigenstrain that is recovered elastically in the inclusion, expressed as

$$\epsilon^* = \frac{\mu_2\,(\lambda_2+\mu_2)\left(R^2-\rho^2\right)}{\mu_2\,(\lambda_1-\lambda_2+\mu_1-\mu_2)\,\rho^2 + (\lambda_2+\mu_2)\,(\lambda_1+\mu_1+\mu_2)\,R^2}. \tag{E.4}$$

The total elastic strain energy of such a system is thus given by

$$\hat{\Psi}_{\mathrm{el}} = \sum_{i=1}^{2} \int_{\Omega_i} \psi_i^{\mathrm{el}}\, \mathrm{d}V = 2\pi\,(\lambda_1+\mu_1)\,\rho^2 \epsilon^* \epsilon^2. \tag{E.5}$$

Integrating the interfacial energy density γ over the interface Γ gives the total interfacial energy

$$\hat{\Psi}_{\mathrm{int}} = \int_{\Gamma} \gamma\, \mathrm{d}S = 2\pi\rho\gamma, \tag{E.6}$$

which together with the total elastic strain energy $\hat{\Psi}_{\mathrm{el}}$ constitute the total free energy functional

$$\hat{\Psi} = \hat{\Psi}_{\mathrm{el}} + \hat{\Psi}_{\mathrm{int}}. \tag{E.7}$$

Now consider that the interface Γ is evolving, i.e., the inclusion radius is a function of time, $\rho = \rho(t)$, see Fig. E.1b. Then the global rate-potential $\hat{\Pi}$ is formulated by adding the global dissipation potential $\hat{\mathcal{D}}$ to the rate of the free energy $\dot{\hat{\Psi}} = \mathrm{d}\hat{\Psi}/\mathrm{d}t$,

$$\hat{\Pi} = \dot{\hat{\Psi}} + \hat{\mathcal{D}}. \tag{E.8}$$

Note that no external loading is applied so that the potential energy of the loading does not contribute to $\hat{\Pi}$. The dissipation is here assumed to be of purely viscous nature, i.e., the local dissipation potential $\hat{D}$ is quadratic in terms of the interface speed $\hat{v}_n = -\dot{\rho}$,

$$\hat{\mathcal{D}} = \int_\Gamma \hat{D}\left(\dot{\rho}\right) \mathrm{d}S = 2\pi\rho\hat{D}(\dot{\rho}) = \frac{\pi\rho\dot{\rho}^2}{\hat{m}}, \qquad \hat{D}(\hat{v}_n) = \frac{1}{2\hat{m}}\hat{v}_n^2, \tag{E.9}$$

where $\hat{m}$ denotes the local interface mobility parameter.

Finally, the complete evolution problem is expressed as the minimization of the global rate-potential $\hat{\Pi}$ with respect to $\dot{\rho}$:

$$\dot{\rho}(t) = \arg\min_{\dot{\rho}} \hat{\Pi}. \tag{E.10}$$

Since the global rate-potential $\hat{\Pi}$ is quadratic in terms of $\dot{\rho}$, the condition of stationarity, $\mathrm{d}\hat{\Pi}/\mathrm{d}\dot{\rho} = 0$, delivers an equation that is linear with respect to $\dot{\rho}$. Therefore, $\dot{\rho}$ can be easily found in a closed form,

$$\dot{\rho} = -\hat{m}\frac{\gamma}{\rho} + \hat{m}\frac{2(\lambda_1+\mu_1)(\epsilon^*\epsilon)^2}{\mu_2(\lambda_2+\mu_2)(R^2-\rho^2)^2}\Big(\mu_2(\lambda_1-\lambda_2+\mu_1-\mu_2)\rho^4 \\ -(\lambda_2+\mu_2)(\lambda_1+\mu_1+\mu_2)(R^2-2\rho^2)R^2\Big). \tag{E.11}$$

Assuming the same material for both the inclusion and the matrix, i.e., $\lambda = \lambda_1 = \lambda_2$, $\mu = \mu_1 = \mu_2$, the formula for the total elastic strain energy becomes simpler, cf. Eq. (E.5),

$$\hat{\Psi}_{\mathrm{el}} = \frac{2\pi\mu\rho^2\epsilon^2(\lambda+\mu)(R^2-\rho^2)}{R^2(\lambda+2\mu)}, \tag{E.12}$$

and therefore, the resulting evolution equation reads

$$\dot{\rho} = -\hat{m}\left(\left(\frac{1}{2} - \left(\frac{\rho}{R}\right)^2\right)\frac{E\epsilon^2}{1-\nu^2} + \frac{\gamma}{\rho}\right), \tag{E.13}$$

where Lamé constants have been converted into Young's modulus, E, and Poisson's ratio, ν. The above equation can be rewritten in a more concise format

$$\dot{\rho} = -\hat{m}\left(\hat{f}_{\mathrm{bulk}} + \hat{f}_{\mathrm{int}}\right), \tag{E.14}$$

where

$$\hat{f}_{\mathrm{bulk}} = \left(\frac{1}{2} - \left(\frac{\rho}{R}\right)^2\right)\frac{E\epsilon^2}{1-\nu^2}, \qquad \hat{f}_{\mathrm{int}} = \frac{\gamma}{\rho} \tag{E.15}$$

denote the local thermodynamic driving forces related to the elastic and the interfacial energy, respectively. It can be checked that the thermodynamic driving force $\hat{f} = \hat{f}_{\text{bulk}} + \hat{f}_{\text{int}}$ derived above from the total energy balance can be equivalently obtained from the local definition, Eq. $(3.43)_1$ (to have a consistent sign of the driving force, the interface normal must point into the inclusion so that the inclusion is treated as phase 2 in the notation of Subsection 3.2.1).

Although attempts have been made, it is difficult, if not impossible, to find the solution of Eq. (E.13) in a closed form. Therefore, in the simulations discussed in Section 7.1, the ordinary differential equation (E.13) has been solved using numerical methods instead.

Bibliography

1. R. Abeyaratne, J.K. Knowles, On the driving traction acting on a surface of strain discontinuity in a continuum, *Journal of the Mechanics and Physics of Solids*, **38**(3): 345–360, 1990, https://doi.org/10.1016/0022-5096(90)90003-m.
2. G. Allaire, C. Dapogny, P. Frey, Shape optimization with a level set based mesh evolution method, *Computer Methods in Applied Mechanics and Engineering*, **282**: 22–53, 2014, https://doi.org/10.1016/j.cma.2014.08.028.
3. H. Allik, T.J.R. Hughes, Finite element method for piezoelectric vibration, *International Journal for Numerical Methods in Engineering*, **2**(2): 151–157, 1970, https://doi.org/10.1002/nme.1620020202.
4. M. Ambati, T. Gerasimov, L.D. Lorenzis, A review on phase-field models of brittle fracture and a new fast hybrid formulation, *Computational Mechanics*, **55**(2): 383–405, 2014, https://doi.org/10.1007/s00466-014-1109-y.
5. M.P. Anderson, G.S. Grest, D.J. Srolovitz, Computer simulation of normal grain growth in three dimensions, *Philosophical Magazine B*, **59**(3): 293–329, 1989, https://doi.org/10.1080/13642818908220181.
6. Q. Antoine, J. Remacle, J. Lambrechts, N. Moes, The X-Mesh method applied to multiphase flows, in: *8th European Congress on Computational Methods in Applied Sciences and Engineering*, ECCOMAS Congress 2022, CIMNE, 2022, https://doi.org/10.23967/eccomas.2022.272.
7. A. Artemev, Y. Jin, A.G. Khachaturyan, Three-dimensional phase field model of proper martensitic transformation, *Acta Materialia*, **49**(7): 1165–1177, 2001, https://doi.org/10.1016/s1359-6454(01)00021-0.
8. A. Bartels, J. Mosler, Efficient variational constitutive updates for Allen–Cahn-type phase field theory coupled to continuum mechanics, *Computer Methods in Applied Mechanics and Engineering*, **317**: 55–83, 2017, https://doi.org/10.1016/j.cma.2016.11.024.
9. T. Belytschko, T. Black, Elastic crack growth in finite elements with minimal remeshing, *International Journal for Numerical Methods in Engineering*, **45**(5): 601–620, 1999, https://doi.org/10.1002/(sici)1097-0207(19990620)45:5<601::aid-nme598>3.0.co;2-s.
10. T. Belytschko, C. Parimi, N. Moës, N. Sukumar, S. Usui, Structured extended finite element methods for solids defined by implicit surfaces, *International Journal for Numerical Methods in Engineering*, **56**(4): 609–635, 2002, https://doi.org/10.1002/nme.686.

11. T. Belytschko, S.P. Xiao, C. Parimi, Topology optimization with implicit functions and regularization, *International Journal for Numerical Methods in Engineering*, **57**(8): 1177–1196, 2003, https://doi.org/10.1002/nme.824.

12. D.N. Bhate, A. Kumar, A.F. Bower, Diffuse interface model for electromigration and stress voiding, *Journal of Applied Physics*, **87**(4): 1712–1721, 2000, https://doi.org/10.1063/1.372082.

13. S. Bhattacharyya, R. Sahara, K. Ohno, A first-principles phase field method for quantitatively predicting multi-composition phase separation without thermodynamic empirical parameter, *Nature Communications*, **10**(1): 3451, 2019, https://doi.org/10.1038/s41467-019-11248-z.

14. T. Biben, K. Kassner, C. Misbah, Phase-field approach to three-dimensional vesicle dynamics, *Physical Review E*, **72**(4): 041921, 2005, https://doi.org/10.1103/physreve.72.041921.

15. V. Bongiorno, H.T. Davis, Modified van der Waals theory of fluid interfaces, *Physical Review A*, **12**: 2213–2224, 1975, https://doi.org/10.1103/PhysRevA.12.2213.

16. B. Bourdin, G.A. Francfort, J.-J. Marigo, Numerical experiments in revisited brittle fracture, *Journal of the Mechanics and Physics of Solids*, **48**(4): 797–826, 2000, https://doi.org/10.1016/s0022-5096(99)00028-9.

17. S. Brisard, L. Dormieux, FFT-based methods for the mechanics of composites: A general variational framework, *Computational Materials Science*, **49**(3): 663–671, 2010, https://doi.org/10.1016/j.commatsci.2010.06.009.

18. E. Burman, S. Claus, P. Hansbo, M.G. Larson, A. Massing, CutFEM: Discretizing geometry and partial differential equations, *International Journal for Numerical Methods in Engineering*, **104**(7): 472–501, 2014, https://doi.org/10.1002/nme.4823.

19. G. Caginalp, An analysis of a phase field model of a free boundary, *Archive for Rational Mechanics and Analysis*, **92**(3): 205–245, 1986, https://doi.org/10.1007/bf00254827.

20. G. Caginalp, P.C. Fife, Dynamics of layered interfaces arising from phase boundaries, *SIAM Journal on Applied Mathematics*, **48**(3): 506–518, 1988, https://doi.org/10.1137/0148029.

21. J.W. Cahn, On spinodal decomposition, *Acta Metallurgica*, **9**(9): 795–801, 1961, https://doi.org/10.1016/0001-6160(61)90182-1.

22. J.W. Cahn, Critical point wetting, *The Journal of Chemical Physics*, **66**(8): 3667–3672, 1977, https://doi.org/10.1063/1.434402.

23. J.W. Cahn, J.E. Hilliard, Free energy of a nonuniform system. I. Interfacial free energy, *The Journal of Chemical Physics*, **28**(2): 258–267, 1958, https://doi.org/10.1063/1.1744102.

24. L.-Q. Chen, Phase-field models for microstructure evolution, *Annual Review of Materials Research*, **32**(1): 113–140, 2002, https://doi.org/10.1146/annurev.matsci.32.112001.132041.

25. L.-Q. Chen, A. Khachaturyan, Computer simulation of structural transformations during precipitation of an ordered intermetallic phase, *Acta Metallurgica et Materialia*, **39**(11): 2533–2551, 1991, https://doi.org/10.1016/0956-7151(91)90069-d.

26. S. Choudhury, Y.L. Li, C.E. Krill III, L.-Q. Chen, Phase-field simulation of polarization switching and domain evolution in ferroelectric polycrystals, *Acta Materialia*, **53**(20): 5313–5321, 2005, https://doi.org/10.1016/j.actamat.2005.07.040.

27. J.D. Clayton, J. Knap, A phase field model of deformation twinning: Nonlinear theory and numerical simulations, *Physica D: Nonlinear Phenomena*, **240**(9–10): 841–858, 2011, https://doi.org/10.1016/j.physd.2010.12.012.

28. R.W. Clough, The finite element method in plane stress analysis, in: *Proceedings of 2nd ASCE Conference on Electronic Computation*, American Society of Civil Engineers, Pittsburgh, PA, 1960.

29. J.B. Collins, H. Levine, Diffuse interface model of diffusion-limited crystal growth, *Physical Review B*, **31**(9): 6119–6122, 1985, https://doi.org/10.1103/physrevb.31.6119.

30. C. Cui, R. Ma, E. Martínez-Pañeda, A phase field formulation for dissolution-driven stress corrosion cracking, *Journal of the Mechanics and Physics of Solids*, **147**: 104254, 2021, https://doi.org/10.1016/j.jmps.2020.104254.

31. C. Dapogny, C. Dobrzynski, P. Frey, Three-dimensional adaptive domain remeshing, implicit domain meshing, and applications to free and moving boundary problems, *Journal of Computational Physics*, **262**: 358–378, 2014, https://doi.org/10.1016/j.jcp.2014.01.005.

32. E.A. de Souza Neto, D. Perić, M. Dutko, D.R.J. Owen, Design of simple low order finite elements for large strain analysis of nearly incompressible solids, *International Journal of Solids and Structures*, **33**(20–22): 3277–3296, 1996, https://doi.org/10.1016/0020-7683(95)00259-6.

33. A. Dimokrati, Y.L. Bouar, M. Benyoucef, A. Finel, S-PFM model for ideal grain growth, *Acta Materialia*, **201**: 147–157, 2020, https://doi.org/10.1016/j.actamat.2020.09.073.

34. J. Dobrzański, S. Stupkiewicz, Towards a sharper phase-field method: A hybrid diffuse–semisharp approach for microstructure evolution problems, *Computer Methods in Applied Mechanics and Engineering*, **423**: 116841, 2024, https://doi.org/10.1016/j.cma.2024.116841.

35. J. Dobrzański, K. Wojtacki, S. Stupkiewicz, Lamination-based efficient treatment of weak discontinuities for non-conforming finite element meshes, *Computers & Structures*, **291**: 107209, 2024, https://doi.org/10.1016/j.compstruc.2023.107209.

36. Q. Du, C. Liu, X. Wang, Simulating the deformation of vesicle membranes under elastic bending energy in three dimensions, *Journal of Computational Physics*, **212**(2): 757–777, 2006, https://doi.org/10.1016/j.jcp.2005.07.020.

37. R. Duddu, D.L. Chopp, P. Voorhees, B. Moran, Diffusional evolution of precipitates in elastic media using the extended finite element and the level set methods, *Journal of Computational Physics*, **230**(4): 1249–1264, 2011, https://doi.org/10.1016/j.jcp.2010.11.002.

38. A. Durga, P. Wollants, N. Moelans, Evaluation of interfacial excess contributions in different phase-field models for elastically inhomogeneous systems, *Modelling and Simulation in Materials Science and Engineering*, **21**(5): 055018, 2013, https://doi.org/10.1088/0965-0393/21/5/055018.

39. B. Engquist, O. Runborg, A.-K. Tornberg, High-frequency wave propagation by the segment projection method, *Journal of Computational Physics*, **178**(2): 373–390, 2002, https://doi.org/10.1006/jcph.2002.7033.

40. B. Engquist, O. Runborg, A.-K. Tornberg, High-frequency wave propagation by the segment projection method, *Journal of Computational Physics*, **178**(2): 373–390, 2002, https://doi.org/10.1006/jcph.2002.7033.

41. J.D. Eshelby, Energy relations and the energy-momentum tensor in continuum mechanics, in: J.M. Ball, D. Kinderlehrer, P. Podio-Guidugli, M. Slemrod, eds, *Fundamental Contributions to the Continuum Theory of Evolving Phase Interfaces in Solids: A Collection of Reprints of 14 Seminal Papers*, pp. 82–119, Springer, Berlin, Heidelberg, 1999, https://doi.org/10.1007/978-3-642-59938-5_5.

42. S. Essongue, G. Couégnat, E. Martin, Performance assessment of the augmented finite element method for the modeling of weak discontinuities, *International Journal for Numerical Methods in Engineering*, **122**(1): 172–189, 2020, https://doi.org/10.1002/nme.6530.

43. A. Finel, Y.L. Bouar, B. Dabas, B. Appolaire, Y. Yamada, T. Mohri, Sharp phase field method, *Physical Review Letters*, **121**(2), 2018, https://doi.org/10.1103/physrevlett.121.025501.

44. G. Fix, Phase field models for free boundary problems, in: A. Fasano, M. Primicerio, eds, *Free Boundary problems: Theory and Applications*, vol. II, pp. 580–589, Pitman, Boston, 1983.

45. M. Fleck, F. Schleifer, Sharp phase-field modeling of isotropic solidification with a super efficient spatial resolution, *Engineering with Computers*, **39**(3): 1699–1709, 2022, https://doi.org/10.1007/s00366-022-01729-z.

46. M. Fleck, F. Schleifer, P. Zimbrod, Frictionless motion of diffuse interfaces by sharp phase-field modeling, *Crystals*, **12**(10): 1496, 2022, https://doi.org/10.3390/cryst12101496.

47. L. Gélébart, F. Ouaki, Filtering material properties to improve FFT-based methods for numerical homogenization, *Journal of Computational Physics*, **294**: 90–95, 2015, https://doi.org/10.1016/j.jcp.2015.03.048.

48. S.S. Ghorashi, N. Valizadeh, S. Mohammadi, Extended isogeometric analysis for simulation of stationary and propagating cracks, *International Journal for Nu-*

merical Methods in Engineering, **89**(9): 1069–1101, 2011, https://doi.org/10.1002/nme.3277.

49. V.L. Ginzburg, L.D. Landau, On the theory of superconductivity (in Russian), *Zhurnal Eksperimental'noi i Teoreticheskoi Fiziki*, **20**: 1064–1082, 1950, https://doi.org/10.1016/B978-0-08-010586-4.50035-3.

50. V.L. Ginzburg, L.D. Landau, On the theory of superconductivity, in: D. ter Haar, editor, *Collected Papers of L.D. Landau*, pp. 217–225, Pergamon Press, 1965, https://doi.org/10.1016/c2013-0-01806-3.

51. J. Glimm, J.W. Grove, X.L. Li, K.-m. Shyue, Y. Zeng, Q. Zhang, Three-dimensional front tracking, *SIAM Journal on Scientific Computing*, **19**(3): 703–727, 1998, https://doi.org/10.1137/s1064827595293600.

52. W.I. Goldburg, C.-H. Shaw, J.S. Huang, M.S. Pilant, Spinodal decomposition in a binary liquid mixture, *The Journal of Chemical Physics*, **68**(2): 484–494, 1978, https://doi.org/10.1063/1.435778.

53. D. Gueyffier, J. Li, A. Nadim, R. Scardovelli, S. Zaleski, Volume-of-fluid interface tracking with smoothed surface stress methods for three-dimensional flows, *Journal of Computational Physics*, **152**(2): 423–456, 1999, https://doi.org/10.1006/jcph.1998.6168.

54. L. Guin, D.M. Kochmann, A phase-field model for ferroelectrics with general kinetics, Part I: Model formulation, *Journal of the Mechanics and Physics of Solids*, **176**: 105301, 2023, https://doi.org/10.1016/j.jmps.2023.105301.

55. M.E. Gurtin, *Configurational Forces as Basic Concepts of Continuum Physics*, Springer, New York, 2000, https://doi.org/10.1007/b97847.

56. B.I. Halperin, P.C. Hohenberg, S.-k. Ma, Renormalization-group methods for critical dynamics: I. Recursion relations and effects of energy conservation, *Physical Review B*, **10**(1): 139–153, 1974, https://doi.org/10.1103/physrevb.10.139.

57. F.H. Harlow, J.E. Welch, Numerical calculation of time-dependent viscous incompressible flow of fluid with free surface, *The Physics of Fluids*, **8**(12): 2182–2189, 1965, https://doi.org/10.1063/1.1761178.

58. F.E. Hildebrand, C. Miehe, A phase field model for the formation and evolution of martensitic laminate microstructure at finite strains, *Philosophical Magazine*, **92**(34): 4250–4290, 2012, https://doi.org/10.1080/14786435.2012.705039.

59. C. Hirt, B. Nichols, Volume of fluid (VOF) method for the dynamics of free boundaries, *Journal of Computational Physics*, **39**(1): 201–225, 1981, https://doi.org/10.1016/0021-9991(81)90145-5.

60. T.J.R. Hughes, W.K. Liu, T.K. Zimmermann, Lagrangian-Eulerian finite element formulation for incompressible viscous flows, *Computer Methods in Applied Mechanics and Engineering*, **29**(3): 329–349, 1981, https://doi.org/10.1016/0045-7825(81)90049-9.

61. T.J.R. Hughes, J.A. Cottrell, Y. Bazilevs, Isogeometric analysis: CAD, finite elements, NURBS, exact geometry and mesh refinement, *Computer Methods in Applied Mechanics and Engineering*, **194**(39–41): 4135–4195, 2005, https://doi.org/10.1016/j.cma.2004.10.008.

62. H. Ji, D. Chopp, J.E. Dolbow, A hybrid extended finite element/level set method for modeling phase transformations, *International Journal for Numerical Methods in Engineering*, **54**(8): 1209–1233, 2002, https://doi.org/10.1002/nme.468.

63. D. Juric, G. Tryggvason, A front-tracking method for dendritic solidification, *Journal of Computational Physics*, **123**(1): 127–148, 1996, https://doi.org/10.1006/jcph.1996.0011.

64. M. Kabel, D. Merkert, M. Schneider, Use of composite voxels in FFT-based homogenization, *Computer Methods in Applied Mechanics and Engineering*, **294**: 168–188, 2015, https://doi.org/10.1016/j.cma.2015.06.003.

65. M. Kabel, F. Ospald, M. Schneider, A model order reduction method for computational homogenization at finite strains on regular grids using hyperelastic laminates to approximate interfaces, *Computer Methods in Applied Mechanics and Engineering*, **309**: 476–496, 2016, https://doi.org/10.1016/j.cma.2016.06.021.

66. M. Kabel, A. Fink, M. Schneider, The composite voxel technique for inelastic problems, *Computer Methods in Applied Mechanics and Engineering*, **322**: 396–418, 2017, https://doi.org/10.1016/j.cma.2017.04.025.

67. A. Karma, W.-J. Rappel, Phase-field method for computationally efficient modeling of solidification with arbitrary interface kinetics, *Physical Review E*, **53**(4): R3017–R3020, 1996, https://doi.org/10.1103/physreve.53.r3017.

68. A. Karma, W.-J. Rappel, Quantitative phase-field modeling of dendritic growth in two and three dimensions, *Physical Review E*, **57**(4): 4323–4349, 1998, https://doi.org/10.1103/physreve.57.4323.

69. S. Keshav, F. Fritzen, M. Kabel, FFT-based homogenization at finite strains using composite boxels (ComBo), *Computational Mechanics*, **71**: 191–212, 2023, https://doi.org/10.1007/s00466-022-02232-4.

70. J.H. Keyak, J.M. Meagher, H.B. Skinner, C.D. Mote, Automated three-dimensional finite element modelling of bone: A new method, *Journal of Biomedical Engineering*, **12**(5): 389–397, 1990, https://doi.org/10.1016/0141-5425(90)90022-f.

71. A.G. Khachaturyan, Microscopic theory of diffusion in crystalline solid solutions and the time evolution of the diffuse scattering of X rays and thermal neutrons, *Soviet Physics Solid State*, **9**: 2040–2046, 1968.

72. A.G. Khachaturyan, *Theory of Structural Transformations in Solids*, Wiley, New York, 1983.

73. K. Kim, A. Roy, M.P. Gururajan, C. Wolverton, P.W. Voorhees, First-principles/Phase-field modeling of θ' precipitation in Al-Cu alloys, *Acta Materialia*, **140**: 344–354, 2017, https://doi.org/10.1016/j.actamat.2017.08.046.

74. J.E. Klepeis, Introduction to first-principles electronic structure methods: Application to actinide materials, *Journal of Materials Research*, **21**(12): 2979–2985, 2006, https://doi.org/10.1557/jmr.2006.0371.

75. R. Kobayashi, Modeling and numerical simulations of dendritic crystal growth, *Physica D: Nonlinear Phenomena*, **63**(3–4): 410–423, 1993, https://doi.org/10.1016/0167-2789(93)90120-p.

76. J. Korelc, Automation of primal and sensitivity analysis of transient coupled problems, *Computational Mechanics*, **44**(5): 631–649, 2009, https://doi.org/10.1007/s00466-009-0395-2.

77. J. Korelc, S. Stupkiewicz, Closed-form matrix exponential and its application in finite-strain plasticity, *International Journal for Numerical Methods in Engineering*, **98**(13): 960–987, 2014, https://doi.org/10.1002/nme.4653.

78. J. Korelc, P. Wriggers, *Automation of Finite Element Methods*, Springer International Publishing, 2016, https://doi.org/10.1007/978-3-319-39005-5.

79. C. Kuhn, R. Müller, M. Klassen, D. Gross, Numerical homogenization of the Eshelby tensor at small strains, *Mathematics and Mechanics of Solids*, **25**(7): 1504–1514, 2017, https://doi.org/10.1177/1081286517724607.

80. L.D. Landau, On the theory of phase transitions. I (in Russian), *Physikalische Zeitschrift der Sowjetunion*, **11**: 26, 1937.

81. L.D. Landau, D. Ter-Haar, *Collected papers of L.D. Landau*, Pergamon, Oxford, 1965.

82. J.S. Langer, Statistical methods in the theory of spinodal decomposition, *Acta Metallurgica*, **21**(12): 1649–1659, 1973, https://doi.org/10.1016/0001-6160(73)90108-9.

83. J.S. Langer, Models of pattern formation in first-order phase transitions, in: G. Grinstein, G. Mazenko, eds, *Directions in Condensed Matter Physics: Memorial Volume in Honor of Shang-Keng Ma*, pp. 165–186, World Scientific, 1986, https://doi.org/10.1142/9789814415309_0005.

84. J.L. Lebowitz, J.K. Percus, Statistical thermodynamics of nonuniform fluids, *Journal of Mathematical Physics*, **4**(1): 116–123, 1963, https://doi.org/10.1063/1.1703877.

85. V.I. Levitas, D.L. Preston, Three-dimensional Landau theory for multivariant stress-induced martensitic phase transformations. I. Austenite↔martensite, *Physical Review B*, **66**: 134206, 2002, https://doi.org/10.1103/PhysRevB.66.134206.

86. V.I. Levitas, D.L. Preston, D.-W. Lee, Three-dimensional Landau theory for multivariant stress-induced martensitic phase transformations. III. Alternative potentials, critical nuclei, kink solutions, and dislocation theory, *Physical Review B*, **68**(13): 134201, 2003, https://doi.org/10.1103/physrevb.68.134201.

87. D. Li, L. Chen, Shape evolution and splitting of coherent particles under applied stresses, *Acta Materialia*, **47**(1): 247–257, 1998, https://doi.org/10.1016/s1359-6454 (98)00323-1.

88. K. Li, *The Shifted Interface/Boundary Method for Embedded Domain Computations*, PhD thesis, Duke University, 2021.

89. K. Li, N.M. Atallah, G.A. Main, G. Scovazzi, The shifted interface method: A flexible approach to embedded interface computations, *International Journal for Numerical Methods in Engineering*, **121**(3): 492–518, 2019, https://doi.org/10.1002/nme.6231.

90. Y.L. Li, S.Y. Hu, Z.K. Liu, L.-Q. Chen, Phase-field model of domain structures in ferroelectric thin films, *Applied Physics Letters*, **78**(24): 3878–3880, 2001, https://doi.org/10.1063/1.1377855.

91. Z. Li, X. Yang, An immersed finite element method for elasticity equations with interfaces, in: Z.-C. Shi, Z. Chen, T. Tang, D. Yu, eds, *Recent Advances in Adaptive Computation*, vol. 383, pp. 285–298, American Mathematical Society, 2005, https://doi.org/10.1090/conm/383/07171.

92. Z. Li, T. Lin, X. Wu, New cartesian grid methods for interface problems using the finite element formulation, *Numerische Mathematik*, **96**(1): 61–98, 2003, https://doi.org/10.1007/s00211-003-0473-x.

93. W.D. Lian, G. Legrain, P. Cartraud, Image-based computational homogenization and localization: comparison between X-FEM/levelset and voxel-based approaches, *Computational Mechanics*, **51**(3): 279–293, 2012, https://doi.org/10.1007/s00466-012-0723-9.

94. T. Lin, X. Zhang, Linear and bilinear immersed finite elements for planar elasticity interface problems, *Journal of Computational and Applied Mathematics*, **236**(18): 4681–4699, 2012, https://doi.org/10.1016/j.cam.2012.03.012.

95. C. Liu, P. Shanthraj, M. Diehl, F. Roters, S. Dong, J. Dong, W. Ding, D. Raabe, An integrated crystal plasticity–phase field model for spatially resolved twin nucleation, propagation, and growth in hexagonal materials, *International Journal of Plasticity*, **106**: 203–227, 2018, https://doi.org/10.1016/j.ijplas.2018.03.009.

96. H. Liu, I. Papadimitriou, F. Lin, J. LLorca, Precipitation during high temperature aging of Al–Cu alloys: A multiscale analysis based on first principles calculations, *Acta Materialia*, **167**: 121–135, 2019, https://doi.org/10.1016/j.actamat.2019.01.024.

97. W. Liu, Q.D. Yang, S. Mohammadizadeh, X.Y. Su, An efficient augmented finite element method for arbitrary cracking and crack interaction in solids, *International Journal for Numerical Methods in Engineering*, **99**(6): 438–468, 2014, https://doi.org/10.1002/nme.4697.

98. E.D. Luycker, D.J. Benson, T. Belytschko, Y. Bazilevs, M.C. Hsu, X-FEM in isogeometric analysis for linear fracture mechanics, *International Journal for Numerical Methods in Engineering*, **87**(6): 541–565, 2011, https://doi.org/10.1002/nme.3121.

99. L. Lymperakis, M. Friák, J. Neugebauer, Atomistic calculations on interfaces: Bridging the length and time scales, *The European Physical Journal Special Topics*, **177**(1): 41–57, 2009, https://doi.org/10.1140/epjst/e2009-01167-6.

100. R.H. MacNeal, C.W. McCormick, The NASTRAN computer program for structural analysis, *Computers & Structures*, **1**(3): 389–412, 1971, https://doi.org/10.1016/0045-7949(71)90021-6.

101. C. Mareau, C. Robert, Different composite voxel methods for the numerical homogenization of heterogeneous inelastic materials with FFT-based techniques, *Mechanics of Materials*, **105**: 157–165, 2017, https://doi.org/10.1016/j.mechmat.2016.12.002.

102. P. Michaleris, D.A. Tortorelli, C.A. Vidal, Tangent operators and design sensitivity formulations for transient non-linear coupled problems with applications to elastoplasticity, *International Journal for Numerical Methods in Engineering*, **37**(14): 2471–2499, 1994, https://doi.org/10.1002/nme.1620371408.

103. S. Mirjalili, S. Jain, M. Dodd, Interface-capturing methods for two-phase flows: An overview and recent developments, *Annual Research Briefs 2017*, pp. 117–135, Center for Turbulence Research, Stanford, CA, 2017.

104. N. Moelans, B. Blanpain, P. Wollants, An introduction to phase-field modeling of microstructure evolution, *Calphad*, **32**(2): 268–294, 2008, https://doi.org/10.1016/j.calphad.2007.11.003.

105. M.R. Moldover, J.W. Cahn, An interface phase transition: Complete to partial wetting, *Science*, **207**(4435): 1073–1075, 1980, https://doi.org/10.1126/science.207.4435.1073.

106. J. Mosler, O. Shchyglo, H.M. Hojjat, A novel homogenization method for phase field approaches based on partial rank-one relaxation, *Journal of the Mechanics and Physics of Solids*, **68**: 251–266, 2014, https://doi.org/10.1016/j.jmps.2014.04.002.

107. H. Moulinec, P. Suquet, A numerical method for computing the overall response of nonlinear composites with complex microstructure, *Computer Methods in Applied Mechanics and Engineering*, **157**(1–2): 69–94, 1998, https://doi.org/10.1016/s0045-7825(97)00218-1.

108. N. Moës, J. Dolbow, T. Belytschko, A finite element method for crack growth without remeshing, *International Journal for Numerical Methods in Engineering*, **46**(1): 131–150, 1999, https://doi.org/10.1002/(sici)1097-0207(19990910)46:1<131::aid-nme726>3.0.co;2-j.

109. N. Moës, M. Cloirec, P. Cartraud, J.-F. Remacle, A computational approach to handle complex microstructure geometries, *Computer Methods in Applied Mechanics and Engineering*, **192**(28–30): 3163–3177, 2003, https://doi.org/10.1016/s0045-7825(03)00346-3.

110. N. Moës, J.-F. Remacle, J. Lambrechts, B. Lé, N. Chevaugeon, The eXtreme Mesh deformation approach (X-MESH) for the Stefan phase change model, *Journal of Computational Physics*, **477**: 111878, 2023, https://doi.org/10.1016/j.jcp.2022.111878.

111. L. Munk, S. Reschka, H.J. Maier, P. Wriggers, S. Löhnert, A sharp-interface model of the diffusive phase transformation in a nickel-based superalloy, *Metals*, **12**(8): 1261, 2022, https://doi.org/10.3390/met12081261.

112. W.F. Noh, P. Woodward, SLIC (Simple Line Interface Calculation), in: A.I. van de Vooren, P.J. Zandbergen, eds, *Proceedings of the Fifth International Conference on Numerical Methods in Fluid Dynamics June 28 – July 2, 1976 Twente University, Enschede*, Springer, Berlin, Heidelberg, 1976, https://doi.org/10.1007/3-540-08004-x_336.

113. L. Noël, M. Schmidt, K. Doble, J.A. Evans, K. Maute, XIGA: An eXtended IsoGeometric analysis approach for multi-material problems, *Computational Mechanics*, **70**(6): 1281–1308, 2022, https://doi.org/10.1007/s00466-022-02200-y.

114. M. Ode, S.G. Kim, T. Suzuki, Mathematical modeling of iron and steel making processes. recent advances in the phase-field model for solidification, *ISIJ International*, **41**(10): 1076–1082, 2001, https://doi.org/10.2355/isijinternational.41.1076.

115. S. Osher, J.A. Sethian, Fronts propagating with curvature-dependent speed: Algorithms based on Hamilton-Jacobi formulations, *Journal of Computational Physics*, **79**(1): 12–49, 1988, https://doi.org/10.1016/0021-9991(88)90002-2.

116. J. Parvizian, A. Düster, E. Rank, Finite cell method, *Computational Mechanics*, **41**(1): 121–133, 2007, https://doi.org/10.1007/s00466-007-0173-y.

117. O. Penrose, P.C. Fife, Thermodynamically consistent models of phase-field type for the kinetic of phase transitions, *Physica D: Nonlinear Phenomena*, **43**(1): 44–62, 1990, https://doi.org/10.1016/0167-2789(90)90015-h.

118. C.S. Peskin, Numerical analysis of blood flow in the heart, *Journal of Computational Physics*, **25**(3): 220–252, 1977, https://doi.org/10.1016/0021-9991(77)90100-0.

119. P. Podio-Guidugli, Configurational forces: are they needed?, *Mechanics Research Communications*, **29**(6): 513–519, 2002, https://doi.org/10.1016/s0093-6413(02)00295-1.

120. S. Popinet, An accurate adaptive solver for surface-tension-driven interfacial flows, *Journal of Computational Physics*, **228**(16): 5838–5866, 2009, https://doi.org/10.1016/j.jcp.2009.04.042.

121. S. Popinet, Numerical models of surface tension, *Annual Review of Fluid Mechanics*, **50**(1): 49–75, 2018, https://doi.org/10.1146/annurev-fluid-122316-045034.

122. N. Provatas, K. Elder, *Phase-Field Methods in Materials Science and Engineering*, Wiley, 2010, https://doi.org/10.1002/9783527631520.

123. A. Quiriny, J. Lambrechts, N. Moës, J.-F. Remacle, X-Mesh: A new approach for the simulation of two-phase flow with sharp interface, *Journal of Computational Physics*, **501**: 112775, 2024, https://doi.org/10.1016/j.jcp.2024.112775.

124. M. Rezaee-Hajidehi, S. Stupkiewicz, Phase-field modeling of multivariant martensitic microstructures and size effects in nano-indentation, *Mechanics of Materials*, **141**: 103267, 2020, https://doi.org/10.1016/j.mechmat.2019.103267.

125. M. Rezaee-Hajidehi, S. Stupkiewicz, Micromorphic approach to phase-field modeling of multivariant martensitic transformation with rate-independent dissipation

effects, *International Journal of Solids and Structures*, **222–223**: 111027, 2021, https://doi.org/10.1016/j.ijsolstr.2021.03.014.

126. M. Rezaee-Hajidehi, P. Sadowski, S. Stupkiewicz, Deformation twinning as a displacive transformation: Finite-strain phase-field model of coupled twinning and crystal plasticity, *Journal of the Mechanics and Physics of Solids*, **163**: 104855, 2022, https://doi.org/10.1016/j.jmps.2022.104855.

127. J.S. Rowlinson, Translation of J.D. van der Waals' "The thermodynamic theory of capillarity under the hypothesis of a continuous variation of density", *Journal of Statistical Physics*, **20**(2): 197–200, 1979, https://doi.org/10.1007/bf01011513.

128. M. Rudman, Volume-tracking methods for interfacial flow calculations, *International Journal for Numerical Methods in Fluids*, **24**(7): 671–691, 1997, https://doi.org/10.1002/(sici)1097-0363(19970415)24:7<671::aid-fld508>3.0.co;2-9.

129. P. Sadowski, K. Kowalczyk-Gajewska, S. Stupkiewicz, Consistent treatment and automation of the incremental Mori–Tanaka scheme for elasto-plastic composites, *Computational Mechanics*, **60**(3): 493–511, 2017, https://doi.org/10.1007/s00466-017-1418-z.

130. P.H. Saksono, W.G. Dettmer, D. Perić, An adaptive remeshing strategy for flows with moving boundaries and fluid–structure interaction, *International Journal for Numerical Methods in Engineering*, **71**(9): 1009–1050, 2007, https://doi.org/10.1002/nme.1971.

131. R. Scardovelli, S. Zaleski, Direct numerical simulation of free-surface and interfacial flow, *Annual Review of Fluid Mechanics*, **31**(1): 567–603, 1999, https://doi.org/10.1146/annurev.fluid.31.1.567.

132. D. Schneider, O. Tschukin, A. Choudhury, M. Selzer, T. Böhlke, B. Nestler, Phase-field elasticity model based on mechanical jump conditions, *Computational Mechanics*, **55**(5): 887–901, 2015, https://doi.org/10.1007/s00466-015-1141-6.

133. K. Sedighiani, V. Shah, K. Traka, M. Diehl, F. Roters, J. Sietsma, D. Raabe, Large-deformation crystal plasticity simulation of microstructure and microtexture evolution through adaptive remeshing, *International Journal of Plasticity*, **146**: 103078, 2021, https://doi.org/10.1016/j.ijplas.2021.103078.

134. J.A. Sethian, *Level Set Methods and Fast Marching Methods: Evolving Interfaces in Computational Geometry, Fluid Mechanics, Computer Vision, and Materials Science*, Cambridge Monographs on Applied and Computational Mathematics (No. 3), Cambridge University Press, Cambridge, England, 2nd edition, 1999.

135. J.A. Sethian, P. Smereka, Level set methods for fluid interfaces, *Annual Review of Fluid Mechanics*, **35**(1): 341–372, 2003, https://doi.org/10.1146/annurev.fluid.35.101101.161105.

136. M. Šilhavý, *The Mechanics and Thermodynamics of Continuous Media*, Springer, Berlin, Heidelberg, 1997, https://doi.org/10.1007/978-3-662-03389-0.

137. J. Simmons, C. Shen, Y. Wang, Phase field modeling of simultaneous nucleation and growth by explicitly incorporating nucleation events, *Scripta Materialia*, **43**(10): 935–942, 2000, https://doi.org/10.1016/s1359-6462(00)00517-0.

138. J.C. Simo, T.J.R. Hughes, *Computational Inelasticity*, Springer, New York, NY, 1998, https://doi.org/10.1007/b98904.

139. J.-H. Song, P.M.A. Areias, T. Belytschko, A method for dynamic crack and shear band propagation with phantom nodes, *International Journal for Numerical Methods in Engineering*, **67**(6): 868–893, 2006, https://doi.org/10.1002/nme.1652.

140. D.J. Srolovitz, M.P. Anderson, P.S. Sahni, G.S. Grest, Computer simulation of grain growth—II. Grain size distribution, topology, and local dynamics, *Acta Metallurgica*, **32**(5): 793–802, 1984, https://doi.org/10.1016/0001-6160(84)90152-4.

141. K. Stein, T. Tezduyar, R. Benney, Mesh moving techniques for fluid-structure interactions with large displacements, *Journal of Applied Mechanics*, **70**(1): 58–63, 2003, https://doi.org/10.1115/1.1530635.

142. I. Steinbach, Phase-field models in materials science, *Modelling and Simulation in Materials Science and Engineering*, **17**(7): 073001, 2009, https://doi.org/10.1088/0965-0393/17/7/073001.

143. I. Steinbach, F. Pezzolla, B. Nestler, M. Seeßelberg, R. Prieler, G.J. Schmitz, J.L.L. Rezende, A phase field concept for multiphase systems, *Physica D: Nonlinear Phenomena*, **94**(3): 135–147, 1996, https://doi.org/10.1016/0167-2789(95)00298-7.

144. M. Stolarska, D.L. Chopp, N. Moës, T. Belytschko, Modelling crack growth by level sets in the extended finite element method, *International Journal for Numerical Methods in Engineering*, **51**(8): 943–960, 2001, https://doi.org/10.1002/nme.201.

145. S. Stupkiewicz, *Micromechanics of Contact and Interphase Layers*, Springer, Berlin, Heidelberg, 2007, https://doi.org/10.1007/978-3-540-49717-2.

146. N. Sukumar, D.L. Chopp, N. Moës, T. Belytschko, Modeling holes and inclusions by level sets in the extended finite-element method, *Computer Methods in Applied Mechanics and Engineering*, **190**(46–47): 6183–6200, 2001, https://doi.org/10.1016/s0045-7825(01)00215-8.

147. M. Sussman, E. Fatemi, An efficient, interface-preserving level set redistancing algorithm and its application to interfacial incompressible fluid flow, *SIAM Journal on Scientific Computing*, **20**(4): 1165–1191, 1999, https://doi.org/10.1137/s1064827596298245.

148. M. Sussman, E. Fatemi, P. Smereka, S. Osher, An improved level set method for incompressible two-phase flows, *Computers & Fluids*, **27**(5–6): 663–680, 1998, https://doi.org/10.1016/s0045-7930(97)00053-4.

149. M. Sussman, K.M. Smith, M.Y. Hussaini, M. Ohta, R. Zhi-Wei, A sharp interface method for incompressible two-phase flows, *Journal of Computational Physics*, **221**(2): 469–505, 2007, https://doi.org/10.1016/j.jcp.2006.06.020.

150. A. Tambat, G. Subbarayan, Isogeometric enriched field approximations, *Computer Methods in Applied Mechanics and Engineering*, **245–246**: 1–21, 2012, https://doi.org/10.1016/j.cma.2012.06.006.

151. K. Terada, T. Miura, N. Kikuchi, Digital image-based modeling applied to the homogenization analysis of composite materials, *Computational Mechanics*, **20**(4): 331–346, 1997, https://doi.org/10.1007/s004660050255.

152. T.E. Tezduyar, Interface-tracking and interface-capturing techniques for finite element computation of moving boundaries and interfaces, *Computer Methods in Applied Mechanics and Engineering*, **195**(23–24): 2983–3000, 2006, https://doi.org/10.1016/j.cma.2004.09.018.

153. A. Tornberg, B. Engquist, The segment projection method for interface tracking, *Communications on Pure and Applied Mathematics*, **56**(1): 47–79, 2002, https://doi.org/10.1002/cpa.10052.

154. A.-K. Tornberg, *Interface Tracking Method with Application to Multiphase Flows*, PhD thesis, Royal Institute of Technology, Department of Numerical Analysis and Computing Science, Stockholm, 2000.

155. C. Toulemonde, R. Masson, J.E. Gharib, Modeling the effective elastic behavior of composites: A mixed finite element and homogenisation approach, *Comptes Rendus Mécanique*, **336**(3): 275–282, 2008, https://doi.org/10.1016/j.crme.2007.11.024.

156. D. Tourret, H. Liu, J. LLorca, Phase-field modeling of microstructure evolution: Recent applications, perspectives and challenges, *Progress in Materials Science*, **123**: 100810, 2022, https://doi.org/10.1016/j.pmatsci.2021.100810.

157. D.G. Triezenberg, R. Zwanzig, Fluctuation theory of surface tension, *Physical Review Letters*, **28**: 1183–1185, 1972, https://doi.org/10.1103/PhysRevLett.28.1183.

158. G. Tryggvason, B. Bunner, A. Esmaeeli, D. Juric, N. Al-Rawahi, W. Tauber, J. Han, S. Nas, Y.-J. Jan, A front-tracking method for the computations of multiphase flow, *Journal of Computational Physics*, **169**(2): 708–759, 2001, https://doi.org/10.1006/jcph.2001.6726.

159. K. Tůma, S. Stupkiewicz, H. Petryk, Size effects in martensitic microstructures: Finite-strain phase field model versus sharp-interface approach, *Journal of the Mechanics and Physics of Solids*, **95**: 284–307, 2016, https://doi.org/10.1016/j.jmps.2016.04.013.

160. K. Tůma, S. Stupkiewicz, H. Petryk, Rate-independent dissipation in phase-field modelling of displacive transformations, *Journal of the Mechanics and Physics of Solids*, **114**: 117–142, 2018, https://doi.org/10.1016/j.jmps.2018.02.007.

161. K. Tůma, M. Rezaee-Hajidehi, J. Hron, P. Farrell, S. Stupkiewicz, Phase-field modeling of multivariant martensitic transformation at finite-strain: Computational aspects and large-scale finite-element simulations, *Computer Methods in Applied Mechanics and Engineering*, **377**: 113705, 2021, https://doi.org/10.1016/j.cma.2021.113705.

162. R.L.J.M. Ubachs, P.J.G. Schreurs, M.G.D. Geers, A nonlocal diffuse interface model for microstructure evolution of tin–lead solder, *Journal of the Mechanics and Physics of Solids*, **52**(8): 1763–1792, 2004, https://doi.org/10.1016/j.jmps.2004.02.002.

163. S.O. Unverdi, G. Tryggvason, A front-tracking method for viscous, incompressible, multi-fluid flows, *Journal of Computational Physics*, **100**(1): 25–37, 1992, https://doi.org/10.1016/0021-9991(92)90307-k.

164. V. Vaithyanathan, *Phase-field simulations of coherent precipitate morphologies and coarsening kinetics*, PhD thesis, Pennsylvania State University, 2002.

165. V. Vaithyanathan, C. Wolverton, L.-Q. Chen, Multiscale modeling of precipitate microstructure evolution, *Physical Review Letters*, **88**: 125503, 2002, https://doi.org/10.1103/PhysRevLett.88.125503.

166. J.D. van der Waals, The thermodynamic theory of capillarity under the hypothesis of a continuous variation of density (in Dutch), *Verhandel. Konink. Akad. Weten. Amsterdam* (Sect. 1), **1**(8), 1893.

167. J.D. van der Waals, Thermodynamische theorie der kapillarität unter voraussetzung stetiger dichteänderung, *Zeitschrift für Physikalische Chemie*, **13U**(1): 657–725, 1894, https://doi.org/10.1515/zpch-1894-1338.

168. J.D. van der Waals, Theorie thermodynamique de la capillarite, dans l'hypothese d'une variation continue de densite, *Archives Néerlandaises des Sciences Exactes et Naturelles*, **28**: 121–209, 1895.

169. S.-L. Wang, R.F. Sekerka, A.A. Wheeler, B.T. Murray, S.R. Coriell, R.J. Braun, G.B. McFadden, Thermodynamically-consistent phase-field models for solidification, *Physica D: Nonlinear Phenomena*, **69**(1–2): 189–200, 1993, https://doi.org/10.1016/0167-2789(93)90189-8.

170. Y. Wang, A.G. Khachaturyan, Three-dimensional field model and computer modeling of martensitic transformations, *Acta Materialia*, **45**(2): 759–773, 1997, https://doi.org/10.1016/s1359-6454(96)00180-2.

171. Y. Wang, J. Li, Phase field modeling of defects and deformation, *Acta Materialia*, **58**(4): 1212–1235, 2010, https://doi.org/10.1016/j.actamat.2009.10.041.

172. Y. Wang, L.-Q. Chen, A. Khachaturyan, Kinetics of strain-induced morphological transformation in cubic alloys with a miscibility gap, *Acta Metallurgica et Materialia*, **41**(1): 279–296, 1993, https://doi.org/10.1016/0956-7151(93)90359-z.

173. Y. Wang, D. Banerjee, C.C. Su, A.G. Khachaturyan, Field kinetic model and computer simulation of precipitation of $L1_2$ ordered intermetallics from f.c.c. solid solution, *Acta Materialia*, **46**(9): 2983–3001, 1998, https://doi.org/10.1016/s1359-6454(98)00015-9.

174. Y.U. Wang, Computer modeling and simulation of solid-state sintering: A phase field approach, *Acta Materialia*, **54**(4): 953–961, 2006, https://doi.org/10.1016/j.actamat.2005.10.032.

175. J.A. Warren, W.J. Boettinger, Prediction of dendritic growth and microsegregation patterns in a binary alloy using the phase-field method, *Acta Metallurgica et Materialia*, **43**(2): 689–703, 1995, https://doi.org/10.1016/0956-7151(94)00285-p.

176. P. Wei, M.Y. Wang, X. Xing, A study on X-FEM in continuum structural optimization using a level set model, *Computer-Aided Design*, **42**(8): 708–719, 2010, https://doi.org/10.1016/j.cad.2009.12.001.

177. A. A. Wheeler, W.J. Boettinger, G.B. McFadden, Phase-field model for isothermal phase transitions in binary alloys, *Physisal Review A*, **45**: 7424–7439, 1992, https://doi.org/10.1103/PhysRevA.45.7424.

178. A.A. Wheeler, B.T. Murray, R.J. Schaefer, Computation of dendrites using a phase field model, *Physica D: Nonlinear Phenomena*, **66**(1–2): 243–262, 1993, https://doi.org/10.1016/0167-2789(93)90242-s.

179. B. Widom, Structure of the $\alpha\gamma$ interface, *The Journal of Chemical Physics*, **68**(8): 3878–3883, 1978, https://doi.org/10.1063/1.436195.

180. M. Wörner, Numerical modeling of multiphase flows in microfluidics and micro process engineering: A review of methods and applications, *Microfluidics and Nanofluidics*, **12**(6): 841–886, 2012, https://doi.org/10.1007/s10404-012-0940-8.

181. B. Xu, G. Kang, Q. Kan, C. Yu, X. Xie, Phase field simulation on the cyclic degeneration of one-way shape memory effect of NiTi shape memory alloy single crystal, *International Journal of Mechanical Sciences*, **168**: 105303, 2020, https://doi.org/10.1016/j.ijmecsci.2019.105303.

182. A.J.M. Yang, P.D. Fleming, J.H. Gibbs, Molecular theory of surface tension, *The Journal of Chemical Physics*, **64**(9): 3732–3747, 1976, https://doi.org/10.1063/1.432687.

183. H.K. Yeddu, Phase-field modeling of austenite grain size effect on martensitic transformation in stainless steels, *Computational Materials Science*, **154**: 75–83, 2018, https://doi.org/10.1016/j.commatsci.2018.07.040.

184. J.X. Zhang, L.-Q. Chen, Phase-field microelasticity theory and micromagnetic simulations of domain structures in giant magnetostrictive materials, *Acta Materialia*, **53**(9): 2845–2855, 2005, https://doi.org/10.1016/j.actamat.2005.03.002.

185. P. Zhao, J.C. Heinrich, Front-tracking finite element method for dendritic solidification, *Journal of Computational Physics*, **173**(2): 765–796, 2001, https://doi.org/10.1006/jcph.2001.6911.

186. O.C. Zienkiewicz, Y.K. Cheung, *The Finite Element Method in Structural and Continuum Mechanics: Numerical Solution of Problems in Structural and Continuum Mechanics*, European Civil Engineering Series, McGraw-Hill, 1967.